UNIVERSITY OF MONS- FACULTY OF SCIENCES
Laboratory for Chemistry of Novel Materials

A-D-A π-conjugated molecules: intrinsic properties analysis for renewable energy applications

A dissertation submitted in fulfilment of the requirements for
the degree of Doctor of Science

Antoine RILLAERTS

This thesis was publicly defended on October 1^{st} 2025
before the jury, composed of

Prof. Stéphanos Konstandinis	Université de Mons, Belgium
Prof. Stéphane Lenfant	Université de Lille, Belgium
Prof. Suhao Wang	Université Littotal Côte d'Opale, France
Prof. Mathieu Surin	Université de Mons, Belgium
Prof. Jérôme Cornil	Université de Mons, Belgium

"On ne doit jamais retirer à un être humain sa vie, ni la possibilité de devenir meilleur !"

Robert Badinter citant Victor Hugo

"On ne peut pas changer ce que le destin nous réserve, mais on n'a pas à l'affronter seul."

Mel Medarda dans Arcane

Acknowledgements

I address my deep thankfulness to Professor Roberto Lazzaroni who accepted me in the CMN laboratory, Professor Jérôme Cornil for his supervising previous 5 years and Stéphane Lenfant, Suhao Wang, Mathieu Surin and Stéphanos Konstantinidis for accepting to be members of the thesis jury.

C'est ici que s'achève le voyage et que je vais remercier toutes les personnes que j'ai rencontrées au cours de ces années. Cette aventure a initialement démarré sur fond de démarche personnelle afin d'en apprendre d'avantage sur la personne que je suis et qui n'a probablement plus beaucoup de points communs avec celle que j'étais alors. En parallèle, mes conceptions du travail ont drastiquement et continuellement évoluées afin d'atteindre la rigueur et l'investissement nécessaire à l'accomplissement d'une telle tâche. Je suis soulagé d'avoir atteint l'arrivée mais pas déçu d'avoir entrepris le voyage malgré les difficultés que j'ai rencontrées et contre lesquelles j'ai maintes fois pesté.

J'entame le florilège des personnalités par GG. Ce diminutif exprime à lui tout seul la proximité qui règne entre toi et tes étudiants et qui permet souvent de dissiper la frustration inhérente au travail de recherche, de pouvoir confier ses doutes en plus de recevoir un regard critique mais sans jugement sur le travail que l'on fournit. J'aime me remémorer les deux conférences que nous avons faites tous les deux à l'étranger à Porquerolles et à Boston. Je n'aurais sûrement jamais imaginé me retrouver sur une plage d'une île presque paradisiaque à coté de mon chef, de me faire inviter à un match de basket des Celtics ou encore de n'avoir comme seul recourt pour profiter de la piscine de l'hôtel que de se changer dos à dos. Tout n'a pas fonctionné comme voulu durant cette thèse mais je n'ai aucun regret.

Je remercie également Pascal Viville qui a codirigé ce travail avec Jérôme durant mon mémoire déjà et la première année de mon doctorat. J'ai pu compter sur toi pour la partie expérimentale de mon travail et pour également œuvrer auprès des hautes sphères matérianoviennes afin de rendre le travail plus facile. Dans un contexte plus musical, j'ai pu obtenir gratuitement du matériel musical de qualité pour m'improviser chanteur au sein de Kenduskeag, mon ancien groupe de musique, afin de célébrer l'union de Arthur et Victoire, deux amis que je connais depuis mes années secondaires.

Je m'adresse également à toutes les personnes qui ont participé aux répétitions et à l'élaboration du projet FRIA pour lesquelles elles se sont investies deux années de suite. Le soutien et le coaching dont j'ai pu bénéficier de la part de Jérôme, Roberto, David Beljonne, Mathieu Surin, Olivier Douheret, David Moerman et Pascal Viville a été précieux et décisif dans le succès de la deuxième tentative du concours.

Je tiens à remercier Vincent Lemaur qui m'a formé à l'utilisation des outils nécessaires à l'entièreté de l'étude théorique présente dans ce travail. Tu fais preuve de beaucoup de gentillesse et d'engagement pour nous aider, nous, les mémorants et doctorants, parfois en répondant à nos mails même à des heures fort tardives. Comment parler de toi sans évoquer le Dalmuti qui a été ressuscité pendant mon parcours, accompagné du fidèle "esprit du jeux" qui, pour les néophytes consiste à pourrir joyeusement la partie d'un seul d'entre nous. Je suis très heureux d'avoir croisé ton chemin.

Je tiens à remercier chaleureusement Stéphane Lenfant et Dominique Vuillaume pour leurs disponibilités et leur accueil au sein de leur institution. J'ai pu y trouver de l'assistance lorsque j'en avais le plus besoin afin de poursuivre les expériences qui n'ont, hélas, pas abouties. Mon admission au sein de l'IEMN a marqué un tournant important dans mon parcours en redynamisant ma motivation et ça signifie beaucoup pour moi !

J'adresse ces remerciements à Sébastien Kozlowskyj et Laura Wauters pour le soutien logistique dont tous les membres du CMN. Merci Laura pour l'aide administrative concernant les "marchés publics", "bons de commande", "appel d'offres" ou "insérer le terme administratif de votre choix" qu'il est nécessaire de maîtriser pour effectuer les commandes indispensables à mon projet de recherche. Sébastien, ta maîtrise de l'informatique et de ses profondeurs insondables au commun des mortels nous a assurément tous retirer de nombreuses épines hors des pieds. L'élargissement de mes connaissances informatiques te sont entièrement dues. J'ai pris énormément de plaisir à discuter software et hardware mais aussi à me plonger dans des projets personnels grâce à tes précieux conseils.

L'ambiance CMN ne serait pas la même sans Mariano, Zoé, Tudor, Maxime, Ari, Nico, Louis, Isaac, Alexis, David D., Mohammed, Tina et Guille. J'inclus dans ce groupe également Mary, Stella, Clara et Pauline. La plupart d'entre eux formaient déjà un groupe soudé mais ils ont eu la délicate attention de me convier à la plupart de leurs événements, ce qui m'a beaucoup touché. On se sera rencontré plutôt vers la fin mais je garde de mémorables souvenirs et un de mes plus beaux voyages au ski.

Cher Florian, le moins que l'on puisse dire c'est que nous aurons mutuellement marqué la vie de l'autre. J'ai passé différents caps avec toi comme la première collocation liée au départ du nid familial ou encore la première supervision d'un étudiant que ce soit en stage ou pour son mémoire. Je suis heureux d'avoir vécu ces moments avec toi malgré les quelques difficultés que nous avons pu rencontrer. En même temps quelles amitiés ne s'entachent jamais de l'un ou l'autre différent ? Je te souhaite plein de courage et de réussite dans la suite de ton parcours académique.

Les années passées à l'université m'ont amené à rencontrer beaucoup de monde. Parmi ceux-ci, il y a certainement mes camarades de promotion qui ont participé à forger la personne que je suis aujourd'hui. Merci Alexandre, Julien, Benja, David, Angélique et Hugo pour les agréables moments passés à la fois sur le campus comme en dehors. Alexandre, on se souviendra toujours de cette solution inconnue est passée de transparent à jaune en la versant dans un autre contenant. Ce qui n'a pas manqué d'être accompagnée d'un tonnerre d'injures dont j'épargne le lecteur.

Au delà du laboratoire, je peux toujours compter sur des amis de longue date. David, Romain, Raphaël, Arnaud et Jessica pour ne citer que mes plus proches amis du groupe "Oxfam". Ce groupe qui se fonda l'envie d'avoir notre mot à dire sur la pauvreté, qui n'est malheureusement pas toujours si lointaine qu'on le pense. J'ai eu la chance de continuer à vous côtoyer, après nos années "Saint Vincent" et vous m'avez apporté beaucoup d'énergie et de joie qui m'ont souvent permis de passer à travers les moments difficiles. J'ai fait plus ample connaissance avec certains d'entre vous pendant cette période et parfois à changer mon point de vue ce qui fut très enrichissant.

J'ai l'immense chance de pouvoir compter sur deux parents non seulement brillants mais aussi aimants qui m'ont toujours placé au centre de leurs préoccupations et de leur vie. J'ai déjà eu l'occasion de dire qu'ils étaient les meilleurs du monde et chaque jour qui passe ne fait que renforcer ce sentiment. Merci également à ma famille qui a souvent été derrière moi et même si certains ne verront jamais ces mots, je leur transmets en pensée.

Enfin, je conclurai cette partie en parlant de toi qui partage maintenant mon quotidien. Pendant la période de rédaction, s'il a toujours fait bon vivre chez nous, c'est entièrement à toi que je le dois. Merci Emma pour ton soutiens indéfectible, ta complicité, tes rires, tes attentions,... Ton amour tout simplement. Tu es une personne merveilleuse que j'ai eu la chance de rencontrer et sans qui j'ai dorénavant du mal à envisager l'avenir. Tu as raison à propos de "qu'est ce que l'amour", c'est garder son enthousiasme pour réaliser et vivre comme on le fait normalement mais c'est quand même beaucoup mieux avec toi. En retour, j'espère également que je t'apportes autant que ce que tu me donnes. J'ai hâte de découvrir ce que l'avenir nous réserve pour me retourner et admirer ce que nous aurons bâtit.

Abstract

This work investigates a class of molecules with strong potentials for new green energy production applications, focusing on special molecular structures: A-D-A π-conjugated systems. The targeted applications are organic photovoltaics and thermoelectricity.

Density Functional Theory (DFT) calculations were performed to model their electronic structure and highlight their key features for organic photovoltaic (OPV) applications. DFT results show push-pull effect between electron rich and electron poor fragments which impact the light absorption window located in the visible region while creating charge transfer (CT) excited state, useful to split exciton into free carriers by reducing coulomb interactions. This was supported by UV-vis absorption experiments in solutions and thin films. DFT was also used to predict the directionality for charge transport for some compounds in their crystalline structure.

AFM analyses were carried out on organic active layers containing a donor polymer and an acceptor A-D-A molecule, blend required for an efficient charge generation process in solar cell. This helped us to understand layer deposition behavior using a spin-coater and to determine the best parameters for active layer deposition such as nature of the solvent, solution concentration, rotation speed, etc. It has been shown that not only the miscibility is important, but also the boiling point temperature and viscosity that are tailoring domain size and have strong impact on final device performances.

Then, we had to choose carefully interlayer materials and electrodes to match HOMO/LUMO energy levels and/or work functions while avoiding to dissolve previously deposited layers. We have shown that interlayers have also a significant impact on performances and are not always straightforward to choose.

Charge carrier mobility has also been analyzed in a vertical device configuration to extract the intrinsic behavior of active layer using impedance spectroscopy in a Metal-Insulator-Semiconductor (MIS) device.

All these measurements have been correlated to OPV device performance and underlying parameters such as open-circuit voltage, short-circuit current, fill factor and yield.

Similar molecule structures have shown a thermoelectric response when doped and a comparison is performed at the end of this work with molecules generally used in OPV applications. In parallel, molecular mechanic (MM) and molecular dynamic (MD) tools should have been used to simulate thermal transport in a crystal of one A-D-A derivative to assess their potential application in thermoelectric generator but the project was aborted because technical issues.

Contents

Scientific activities

Peer Reviewed publications

1. Regnier, F., **Rillaerts, A.**, Lemaur, V., Viville, P. and Cornil, J.(2023). The impact of side chain elongation from the Y6 to Y6-12 acceptor in organic solar cells: a fundamental study from molecules to devices. *Journal Of Materials Chemistry C*, 11(22), 7451-7461.
2. Wang, S., Wei, H., **Rillaerts, A.**, Deneme, I., Depriester, M., Manikandan, S., ... and Pisula, W. (2025). N-Type Molecular Thermoelectrics Based on Solution-Doped Indenofluorene-Dimalononitrile: Simultaneous Enhancement of Doping Level and Molecular Order. *Advanced Materials Technologies*, 10(1), 2401131.
3. Regnier, F., Rillaerts, A., Viville, P., and Cornil, J. (2023). A Joint Theoretical and Experimental Characterization of the Rising Star Y6 Acceptor Used in Organic Solar Cells: From Molecules to Devices. Chimie Nouvelle, 140, 17-31.

Conference attendance

1. Advanced materials for energy storage and conversion(2021), Bordeaux, France: *Summer school*.
2. Emerging Solar Energy Materials & Applications(2022), Porquerolles, France: *Poster presentation*.
3. Material Research Society (MRS) Fall meeting(2022), Boston, USA: *Poster presentation*.
4. Société Royal de Chimie (SRC): Young Chemist's day(2024 and 2025), Bruxelles, Mons and Namur, Belgium: *Talk and poster presentation*.
5. SRC: Journée scientifique(2024), Mons, Belgium: *Poster presentation*.

Internship

Research stay at Brilliant Matters Company and Université Laval,1st July - 31th September 2023, Québec, Canada.

List of Abbreviations

AC	**A**lternative **C**urrent
ADA	**A**cceptor **D**onor **A**cceptor
AFM	**A**tomic **F**orce **M**icroscopy
ALD	**A**tomic **L**ayer **D**eposition
BM	**B**rilliant **M**atters
BDD	**B**enzo**D**ithiophene**D**ione
BDTT	**B**enzo**D**i**T**hiophene alkyl**T**hienyl
BHJ	**B**ulk **H**etero-**J**unction
CB	**C**hlor**B**enzene
CF	**ChloroF**orm
CV	**C**yclic **V**oltammetry
CT	**C**harge **T**ransfer
CO_2-eq	**CO_2 equivalent**
COP	**C**onference **O**f **P**arties
DC	**D**irect **C**urrent
DFT	**D**ensity **F**unctional **T**heory
EPBT	**E**nergy **P**ay**B**ack **T**ime
ETL	**E**lectron **T**ransport **L**ayer
EU	**E**uropean **U**nion
FTIR	**F**ourier **T**ransform **I**nfra **R**ed
FWHM	**F**ull-**W**idth-at-**H**igh-**M**aximum
GDP	**G**ross **D**omestic **P**roduct
GHG	**G**reen **H**ouse **G**ases
GIWAXS	**G**razing **I**ncident **W**ide-angle **X**-ray **S**cattering
H-F	**H**artree-**F**ock
HTL	**H**ole **T**ransport **L**ayer
IEA	**I**nternational **E**nergy **A**gency
IPA	**I**so **P**ropyl **A**lcohol
IS	**I**mpedance **S**pectroscopy
LCAO	**L**inear **C**ombination of **A**tomic **O**rbitals
MD	**M**olecular **D**ynamic
MIS	**M**etal **I**nsulator **S**emiconductor
NFA	**N**on-**F**ullerene **A**cceptor
NTO	**N**atural **T**ransition **O**rbital
OFET	**O**rganic **F**ield **E**ffect **T**ransistor
OPV	**O**rganic **P**hoto**V**oltaic

OSC	**O**rganic **S**emi**C**onductor
OTE	**O**rganic **T**hermo**E**lectric
PCE	**P**ower **C**onversion **E**fficiency
PBC	**P**eriodic **B**oundary **C**onditions
PV	**P**hoto**V**oltaic
SCLC	**S**pace **C**harge **L**imited **C**urrent
S-Q	**S**hockley-**Q**ueisser
TE	**T**hermo**E**electric
TEG	**T**hermo**E**lectric **G**enerator
U-V	**U**ltra-**V**iolet
VDW	**V**an **D**er **W**aals
WW1	**W**orld **W**ar **1**
WW2	**W**orld **W**ar **2**

Chapter 1

Introduction

1.1 Environmental crisis

1.1.1 Origins

Everyone has ever heard of “global warming”, “overshoot day” or “carbon footprint” and can give a theoretical definition of each word. But what do they mean to our individual and global behavior as human beings? A minority spreads the word that humans are not responsible of any climate changing while a majority thinks that we are strongly accountable of temperature rising and climate effects associated.

According to an European survey, 77% of European citizens think that this is a serious topic that we need to focus on. To the question of choosing the best actor to solve the existing situation, 56% of them think about European Union (EU), 53% about companies and industries and 56% about national governments while 30% think that we have individually the power to make things change and 36% think that this power lies in the local and regional authorities hands. Finally, 30% takes environmental organizations as responsible for the climate change[1].

This study shows that a majority of persons is concerned by the climate question often raised in media during political elections and polemic debates. But it also demonstrates how complex the question is because they are many actors that can influence it in multiple directions. Moreover, these actors are present in many activity sectors such as transport, energy production, raw material extraction, etc. Of course, the carbon footprints are not similar for each field of activity. At the world scale, in 2022, the top four sectors with biggest carbon footprint were respectively energy consumption and more precisely, the electricity and heat production with roughly 15.18 Bt CO_2, transport with 7.29 Bt, manufacturing and construction with 6.22 Bt and agriculture with 5.27 Bt[2].

At the same time, sector impact is not similar in every country since needs and economical development are specific to each world region. Top four country/region in 2022 with the highest carbon emission were China with 11.40 Bt of CO_2, Asia (without China and India) with 7.55 Bt, U.S.A. with 5.06 Bt and India with 2.83 Bt. Correlating these numbers with the population size makes it consistent since China has 1.469.117.710 inhabitants, Asia (excluding India and China) 1.923.582.595 inhabitants, U.S.A 340.990.475 inhabitants and India 1.450.094.130, which corresponds in total to 5.183.784.910 inhabitants, 63% of the global population.

Nevertheless only referring to greenhouse gases (GHG) by country would not represent an accurate distribution of emission because many industries nowadays have a dedicated production for Europe and North America because labour costs are drastically inferior in emerging countries. This means that the carbon emission weight of western countries is under evaluated and including the Gross Domestic Product (GDP) could be a better approach. However, if trends were consistent one hundred years ago, it is no longer the case for every country since most of them have invested in clean energy production.

In an International Energy Agency (IEA) report, it was shown that clean energies represented 33% of energy investment against 66% for fossil fuel infrastructure 20 years ago while, nowadays, the average balance tends to be 65% and 35% for clean energy and fossil fuels respectively. Besides, electrification has sharply risen for applications that were using fuels previously such as heating and cooking, mobility, or in industrial and agriculture processes for examples. Moreover, the technical energy efficiency has increased reducing the amount of energy behind the generation of a GDP unit because technology development helped to improve the efficiency of devices such as refrigerators, air conditioners, vehicles, electric motors or industrial boilers. Finally, in the U.S.A., the fuel for energy production has been replaced from coal to natural gas with a cleaner combustion in parallel to renewable energy infrastructures[3].

Other data representation can show a complete different point of view of the problem. As already said above, China, India, U.S.A., and the European Union generate more than 50% of the total emission in 2022. These data inform us on the geographical emission localisation and imply that a strong collaboration between Asia, North America and the U.E. is mandatory to achieve a sustainable amount reduction of CO_2.

On the other hand, considering emission amount per person (Fig. 1.1) seems more fair because high population countries will obviously contribute more than countries with a low population. In such a representation, Qatar raises to the top with 37.6 tons per capita, followed by United Arab Emirates with 25.8 tons per capita and Bahrain with 25.7 tons per capita while countries at the bottom of the list are Democratic republic of Congo, Somalia and Central Africa Republic. Typically, high per capita emission countries are, most of the time, among the richest ones. Belgium per capita emissions is quite close to China with 7.7 tons against 8 tons respectively.

Moreover, since carbon dioxide stays in the atmosphere for centuries, responsibility of each country is time dependent. The industrial period has started in the United Kingdoms at the middle of the 18^{th} century before propagating to other countries. Contributions are mainly distributed between European and North American countries until the end of the 19^{th} century before reaching other continents. This historical conception explains that society transition to the post industrial period has also

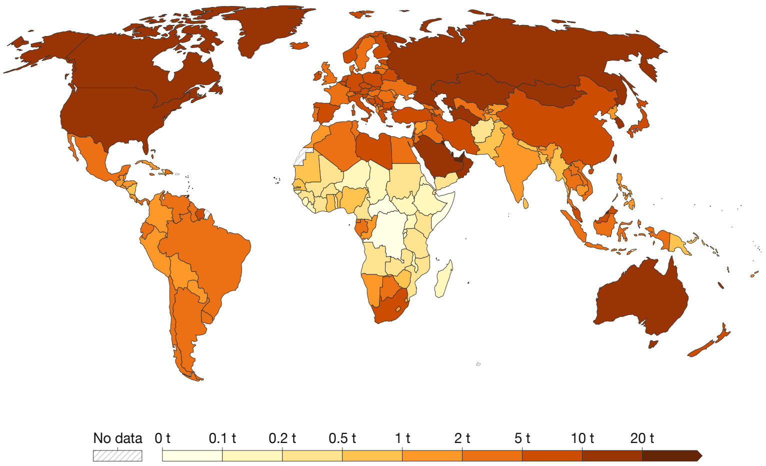

FIGURE 1.1: *World diagram representing carbon dioxide emission per capita. Darker color for larger CO_2 emission.*

risen the standard of living in many countries and inequities in other countries with a lower greenhouse effect gas emission rate. Nowadays, rich countries might have a lower carbon footprint but responsibility distribution with poor countries is not equal since these populations would also like to lift people out of poverty but cannot follow the same pathway as occidental societies.

Finally, previous data were only focused on domestic emission but what if we take into account trade related emissions. Regarding economy in Western European countries, globalisation has exported industries and many companies to poorer countries since transporting merchandises from far regions where employment laws and ecological restrictions are more flexible reduces the costs compared to local employment. Besides having a bad effect on local jobs, it also increases strongly our carbon footprint. Data adjustment can be made by adding emissions related to importation and subtracting emissions related to exportation.

Regarding the world diagram (Fig. 1.2), richer countries from Europe and North America tend to be net importers with some countries from South America and Africa while poorer countries across Asia, some countries from South America and Africa are net exporter. One can make an interesting comparison between Belgium and China, often targeted for high CO_2 production. In 2022, China global proportion of carbon dioxide related to trade hits roughly 10% while in the case of Belgium, it is estimated to about 108%[4].

The last data I wanted to collect were about my own country, Belgium. It has produced 103.6 Mt of carbon dioxide in 2022 divided in several sectors: transport (23.4%), industrial process, energy production and energy consumption by industries (46.3%), heating (17.4%), agriculture (11.1%) and waste and other sources (1.8%)[5].

Moreover, Belgium GHG peak production settled in 1873 and is bound to industrial activity of steel and other metals, textile, glass and coal extraction but has felt consecutively due to world war one (WW1), wall street crash and WW2.

The rebuild of European countries after WW2 had a strong impact on their industry and their modernization, and became more competitive. It has been followed by a coal crisis after 1950 followed by oil crisis in 1974. Nowadays Belgium economy is settled in the tertiary sector, governed by services and non-merchant fields, which has for consequence to increase importation. Our carbon footprint thus relies on our standard of living rather than on real production that can be leveraged[6].

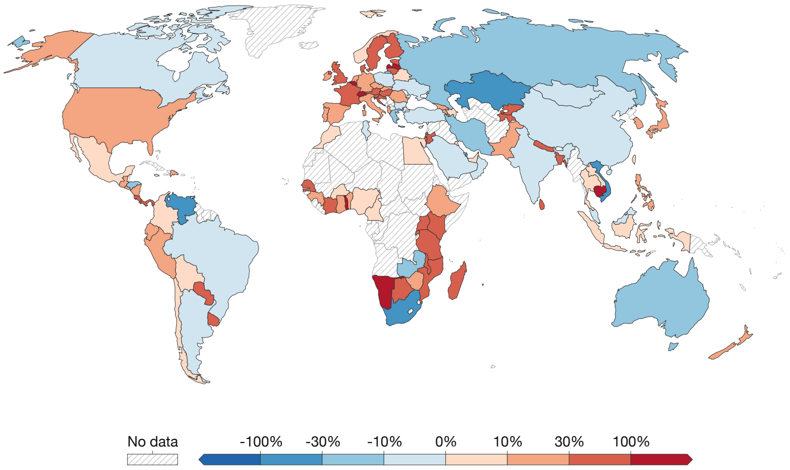

FIGURE 1.2: *World diagram representing carbon dioxide emission embedded in trade[4]. Blue scale represents CO_2 exporter while red scale stands for CO_2 importer.*

1.1.2 What is the matter?

CO_2, CH_4, N_xO,... are part of what we call GHG because they absorb sunlight and contribute to warm up ambient air. They are essential to get temperature inertia and keep a stable range to enable life on Earth. Nevertheless, excess of them can have big consequences on our livings by raising temperature and influencing climate variables such as humidity, air mass distributions and displacement speed, warmth etc. Indirectly, these parameters influence the flora and fauna behaviour depending on the light and water quantity available for photosynthesis for example which are indispensable for animals development. One can see the chain reaction going on by examining only the changes in gas distribution in the atmosphere.

Since all the previous data can help us to figure out the origin of the carbon footprint, the following question comes up: *How far would our livings be impacted?*. But first, we need to rise numbers behind the concept of a high carbon footprint. It is well known that global mean temperatures were rising from 1850-1900 till now to reach

+1.1°C compared to that period (Fig. 1.3). The correlation with human activities is based on the evolution of the rising quantities of GHG emissions in the atmosphere and the concentration of GHG in the atmosphere during the same period of time.

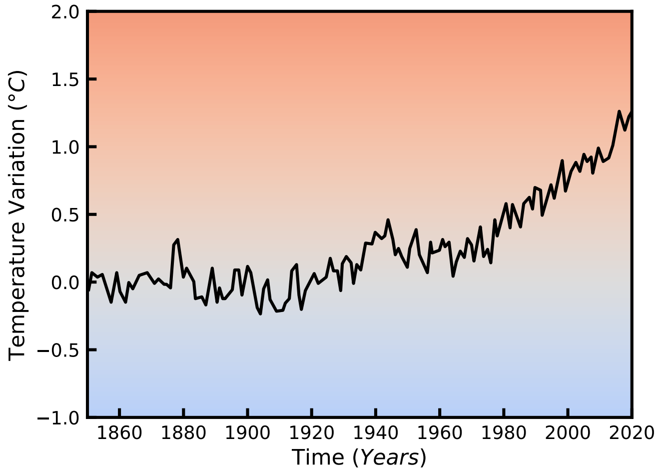

FIGURE 1.3: Changes in global surface temperature since 1850 until 2020.

Concentrations may seem infinitesimally small but what matters is the evolution trend. Values for CO_2, CH_4 show a slow crescent trend until 1950 followed by a steeper slope while the N_2O slope evolves more slowly. At the same time, trends are very similar in terms of GHG emitted quantities. One can see that the major contribution comes by far from fossil fuel and industry activities while the non CO2-emission and that from Land Use, Land-Use Changes and Forestry (LULUCF) show much less variation. Warm periods were caused by small orbital variation during multi millennial time period meaning that current growth points to humans as responsible according to climate models[7]. When it is getting warmer, extreme weather phenomena occur at higher frequency and strength. At the same time, changing the sea and air current distribution would impact weather forecast over several locations. Moreover, this change will impact biodiversity starting by plants followed by the whole food chain. In parallel, ice located at the pole will melt and participate to the sea level rising but also to the global warming because ice reflects much more quantity of light than water that absorbs it. This means that ice melting will increase the quantity of light absorbed by water and accelerate in turn the ice melting by warming up water.

It is important to clarify that life would not disappear because of global warming but our life style would be strongly impacted as well as nature as we know it. One would then understand the emergency of taking strong action to reduce our carbon footprint.

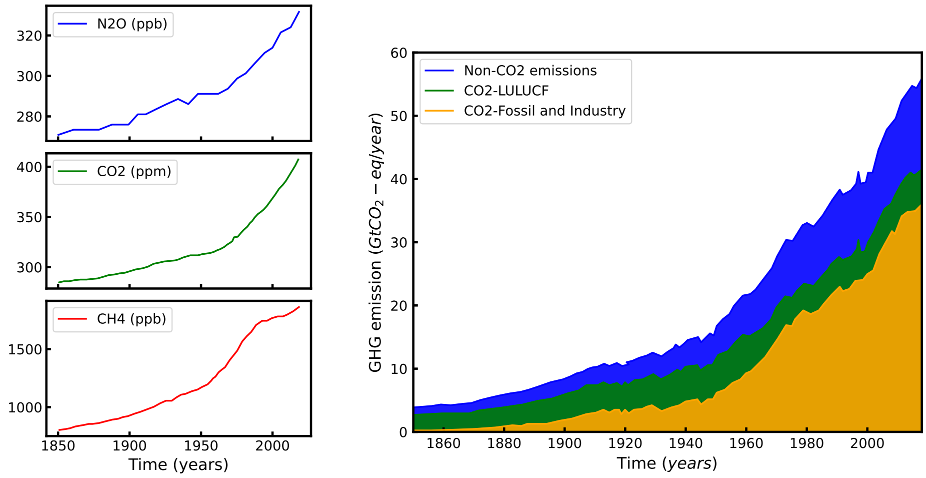

FIGURE 1.4: Graphics showing correlation between temperature rise, GHG emission and concentration and human activities[7].

1.2 Prospects for a greener world

It is clear that the problem is really complex and there are no simple solutions to apply to solve this global crisis. Present statements show a rise of the mean temperature of 1.1°C between 2011-2020 and the objective will be to keep it below 1.5°C at least. There are several models to target a mean temperature rising for 1.5°C, 2°C, 3°C etc associated with their relation with weather and climate modifications to target mitigation pathways. Unfortunately, national contributions, those implemented and financial contributions are not sufficient to maintain the target across all sectors and regions. Indeed, GHG emissions since 1850 were 2400 ± 240 Gt (Fig:1.3) that can be divided in two contributions: 58% of emissions before 1989 and 42% of them since 1989, meaning that our carbon footprint raised significantly in the recent period. For instance, 59 ± 6.6 $GtCO_2$-eq were emitted in 2019 which is 54% higher than in 1990.

Each ton of CO_2 weight in the global warming of about 0.45°C (likely range from 0.27°C to 0.63°C) and there is a budget allocated to each temperature threshold cited above. Estimation allows us only 500 $GtCO_2$-eq to stay under the 1.5°C with a likelihood of about 50% and 1150 $GtCO_2$-eq with a likelihood of 67% to stay under 2°C. This implies that to maintain temperature below 1.5°C, the most plausible scenario is a reduction of our GHG emissions by 43% until 2030, 69% until 2040 and 84% until 2050.

Before taking actions, it is important to create instruments of regulation, economic indicators,...which have already been settled by many countries. Many famous international conventions have been organised since the global awareness about our footprint on Earth biotope such as Kyoto Protocol, Paris Agreement and many other Conferences Of Parties (COP). Despite the many conferences and the controversial political engagement in them, the existence of such conferences marks a certain will to answer the climate problematic.

One would say that we need to reduce our consumption to reduce individual and industrial impact on greenhouse effects while others would say that technology and scientific research will help us fighting global warming, or that actions could be taken from individual to company scale or could be imposed by government laws at large scale, Multiple sectors can be targeted such as food and particularly meat production and exportation, car production, etc. For example, national policies have been taken to improve energy efficiency, rate of deforestation reduction and speed up the roll-out of technologies. GHG reductions were expected around 6 Gt CO_2-eq/year even if current results tend rather to reach 2 Gt CO_2-eq/year[7].

If the majority agrees on the necessity of taking actions, the pathway is not clear yet because there are several strategies. Indeed while some defends the urge to reduce economical growth and try to limit the wealth accumulation, others would like to develop technologies to reduce our global footprint while keeping our standards of living and conception of economy. These two main point of view are usually and respectively called *Degrowth* and *Green-* or *Sober growth*.

Degrowth consists in lowering economical consumption and production by inducing changes in our lifestyle and social behaviour to avoid the classic exponential evolution trend encountered in the livings[8]. *Living better with less*, some of their major arguments consist in reducing human transport around the globe, fighting against planned obsolescence related to overconsumption, questioning certain activity sector place such as advertising, reducing fiscal advantages on plane fuel and goods truck. They would change GDP, as wealth indicator, propose something else than capitalism that would favour wealth redistribution and social solidarity. Citing Paul Ariès *Capitalism is an accumulation regime that works like a bike, when it stops moving, it falls. So the capitalism is the economical system that needs the most that people consume ever more while they rather need to limit themselves.*[9].

The other point of view wants to explore technological solutions such as electrification and renewable sources of energy to get rid of fossil sources that are in a finite amount. There are many sources existing such as wind, solar, geothermal, hydroelectric, biomass or marine power as main alternatives[10]. Even if their carbon footprints are not zero, it is low enough to be compensated after a short time activity. Here are some median values for the whole life-cycle (Table 1.1):

My point of view to reach necessary milestones and reduce our carbon footprint considers the two points of view. It is necessary to explore other sources of energy, optimize energy conversion to reduce energy loss and hence CO_2 production excess and develop technology that would help us reducing our needs while it is also mandatory to stop the perpetual race for innovation that also implies constant need of consumption accelerated by organised obsolescence. To Stop the perpetual need of economic growth which is not consistent with the finite amount of resources available. There is a compromise to find between a reduction of our standard of living and developing strategies to transform our fossil fuel dependency into other sources more reliable and available in an infinite amount.

Energy source	Life-cycle emission (gCO_2-eq/kWh)
Wind	11-12
Hydro-power	24
Geothermal	38
Solar PV	41-48
Biomass	230
Gas	490
Coal	820

TABLE 1.1: Common sources of energy associated with their respective carbon footprint life cycle per kWh[11].

Solar photovoltaics (PV) drew my attention since the Sun represents a very large amount of energy and despite the intermittence of day/night switch, it is the most stable and reliable source. Indeed fluctuations of insolation have been constant since many years compared to wind or hydro-power that are more changing. I decided then to explore PV technology and a research advancement for my PhD and I will describe the topic more in detail in the following.

1.3 Solar photovoltaic energy

1.3.1 Today's technology

Even if the solar energy is not the least carbonated energy, it has the largest reservoir. Indeed, one has measured that 173,000 TW are coming directly from the Sun, combining the total solar irradiance with the total Earth's surface, considering also day and night alternation, seasons and fluctuations during the day. Taking into account that atmosphere absorbs at certain wavelengths and sunlight emission varies along the latitude, the amount available for harvesting if 15% of land surfaces were covered by PV facilities having a 10% yield is about 2500 TW. Interestingly, 2500 TW would be largely enough considering our annual consumption: latest numbers show a consumption of 19 TW in 2019[12–15].

Price is the sinew of the war, that is why i looked for the price of a MWh for main energy sources (Fig.1.5). PV price has largely fallen since 2009 to reach the fossil fuel price zone, in gray on the graph, getting even cheaper between 2018 and 2022. Another renewable source, wind-onshore, has followed the same trend while fossil fuel tends to stay constant. One notices that nuclear, also considered as CO_2 free energy source, is getting more expensive since 2016 but it will stay a major actor for the future since it is well implanted in many countries[16,17]. Currently, the photovoltaic technology requires crystalline or amorphous silicon, the second one conceding a better carbon footprint, reaching up to 15% yield[18]. Nevertheless, the only benefit of this material is its abundance and availability in the earth crust because it has actually poor absorption capability, and requires thick layers to reach

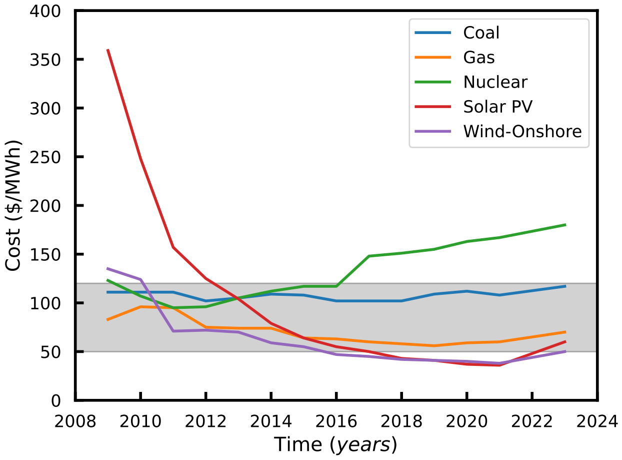

FIGURE 1.5: Graph reporting the price per MWh evolution during the past year for each source. The grey zone represents the fossil fuel average price[16].

decent results; it has also non-negligible carbon foot print, purifying silicon to build 1m^2 of photovoltaic panel spends 400 kg CO_2 for mono crystalline silicon produced in china. Considering alternatives like poly-crystal silicon and other production location could help to divide this amount by four[19].

As a result, the amount of time to write off the carbon investment is still sizeable. For example, considering 10-15% yield, European insolation and energy lost during transformation and transportation, crystalline silicon panels would require more than 2.5 years as energy payback time (EPBT) per square meter. Researchers have probed other materials than silicon for such applications, as for example organic photovoltaic materials (OPV) that would require only two months and a half to refund its carbon debt[20,21]. Before giving further explanation, let's introduce the working principle of a PV cell.

1.3.2 Photovoltaic principle

The photovoltaic effect is everything but new, discovered by Alexandre Edmond Becquerel in 1839 who led experiments on metal plates dipped in a corrosive solution and as explained by H.R. Hertz later in 1887[22], he noticed that lighting a corroded metal plate in an electrolyte produces an electrical current. The PV effect was then associated to semiconductor materials and the technology development started with the rise of electronics and the silicon advent in 1954. The first efficient pv cells made of silicon showed up[23]. But how does it work? What is the physics behind such a transformation of light into electricity?

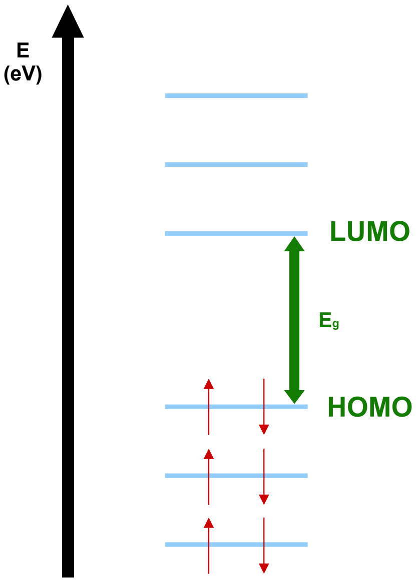

FIGURE 1.6: Scheme of a molecular electronic structure. Electrons are represented by red arrows and orbitals by blue lines. Deeper levels are low in energy and occupied while upper levels are high in energy and empty.

1.3.3 Electronic structure of matter

Let us start with a description of the atomic electronic structure. This requires the approach settled by quantum mechanics to describe the infinitely small, quantifying energy and space for the electrons of an atom. Each electron does not have the same energy and are distributed in specific orbitals which define the electronic structure. Since molecules are composed of several atoms, its electronic structure is obtained by combination of atomic orbitals.

There are then two representations: energy and spatial dependent. In the first one, levels are distinguished by their occupancy. The highest level in energy containing electrons is called the HOMO (Highest Occupied Molecular Orbital) and the lowest energy level without electrons is called the LUMO (Lowest Occupied Molecular Orbital)[24]. The energetic difference between these two frontier orbitals is called the electronic gap, E_g, see (Fig.1.6). The spatial dimension is the location of orbitals on the molecule backbone represented by 3D volume resulting from the combination between atomic orbital values. Depending on their energy, atomic orbital have specific geometry spherically based, giving very complex shape after combination at the molecule scale.

As mentioned earlier, the PV effect occurs only in semiconducting compoun-ds which are characterised by E_g values ranging from 0.5 to 4 eV, for example, silicon with a gap of 1.1 eV. One considers two main classes of materials: inorganic and organic, with the latter subdivided into small π-conjugated molecules and conjugated polymers. My work will only deal with organic semiconductors, so let's focus on their electronic structure specifically[25,26].

One usually talks about a discrete electronic structure for molecules instead of a band structure for long polymer chains. Since molecular orbitals are formed by a linear combination of atomic orbitals, the monomer unit of a polymer also interacts with each other, see example in Fig.1.7. In this way, a polymer composed of a large number of monomer units increases its number of occupied and unoccupied energy levels, reducing the distance between them by filling partly the forbidden band. The electronic gap between the HOMO and LUMO levels is thus reduced, enhancing the intrinsic electrical conductivity properties[27].

For π-conjugated molecules, as for polymer, extending conjugation helps reducing the gap but adding electron withdrawing or donating groups have strong power on the gap size. there are two main effects: inductive effects that apply at short range and based on chemical element electronegativity in opposite of the mesomeric effect effective applying at long range through electron delocalisation over the molecule. The inductive effect is known to symmetrically shift HOMO and LUMO levels, decreasing them when adding an electro-attractor group and increasing them when adding an electro-donor element. The impact of mesomeric effect is less obvious and typically induces an asymmetric response in the HOMO/LUMO shifts.[27–29].

Such strategies let us design molecules with a reduced E_g to achieve good electrical conductivity but also with desired energy for HOMO and LUMO level. One usually target to get a polymer with a high energy HOMO level, easier to ionise and called the donor while the π-conjugated molecule has low energy LUMO level to easily capture an electron and is called the acceptor.

The electrical resistivity for semiconductors ranges from 10^{-6} to 10^{4} Ωm. Materials achieving values below 10^{-4} Ωm are considered as metal while materials exceeding 10^{4} Ωm are considered as insulators[30]. This is correlated with the band gap height; indeed metals have no band gap and hence no difficulty to promote electron in the empty levels by thermal energy while insulators cannot do that because thermal energy (about 0.025 eV) or other stimuli are no sufficient to excite electron from the valence band (VB) to the conduction band (CB). Semiconductors are in between these categories with a barrier of few eV, which is accessible for a higher energetic stimulus, like photons for example.

1.3.4 Light absorption mechanism

Matching electric conductivity and light photons leads to optoelectronic properties, the ability to transform light into electricity and vice versa. The biggest photon source is obviously the sun but one needs to know the amount of light is reaching our region to quantify the efficiency of the photovoltaic module. There are then several parameters to take into account like the earth tilt, time of the day, the weather forecast, seasons…Scientists have then created test light that match all the criteria and reproduce with high fidelity the sun emission spectrum. the conditions that fit our irradiance in Europe are called AM 1.5 (Air Mass 1.5). In comparison, AM0 correspond to the Sun light spectrum in space and AM 1 at the light at the equator

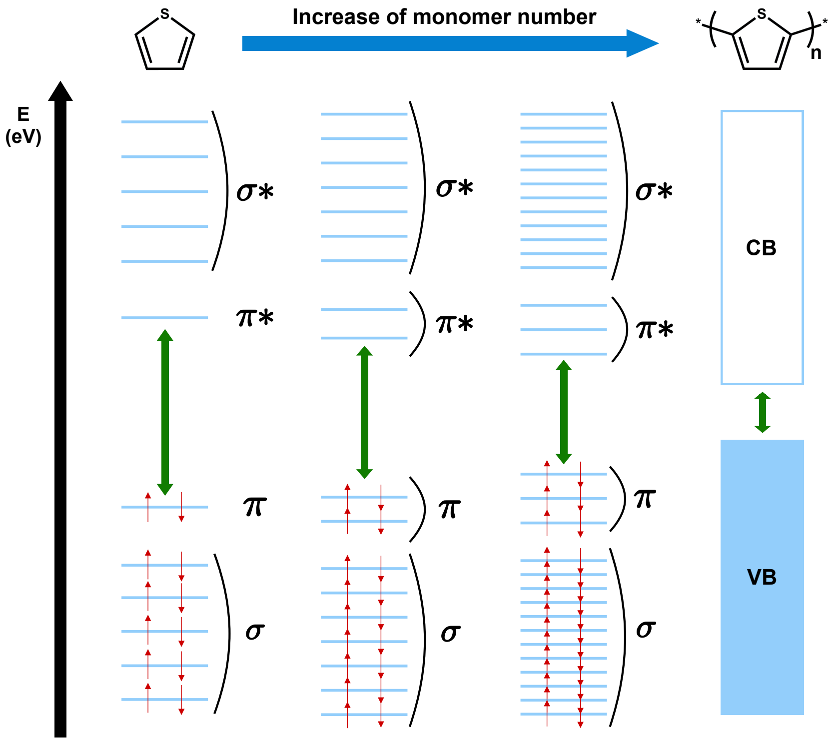

FIGURE 1.7: Scheme of the band structure formation of a polymer because with the number of molecular level rising as a function of the number of monomers. This lead to the formation of the empty conduction band (CB) and the populated valence band (VB).

after passing through the atmosphere. AM 1.5 consider an angle of 48.2° with the normal at the equator, at zenith and without clouds[31].

The absorption results in the promotion of an electron from the HOMO/ valence band to the LUMO/conduction band as a function of the system under study. But not all photons will be absorbed: considering the visible part of the electromagnetic spectrum, the photon energy ranges from 1.6 eV to 2.8 eV (750 nm to 450 nm) but the electronic gap is fixed the molecular structure/polymer length. Thus, only photons with sufficient energy will be able to excite electron to the LUMO/conduction band[32].

In addition, the quantity of photons that can be absorbed differs from one material to another. The absorption coefficient (α) let us quantify the efficiency of absorption. This is a factor proving that silicon is not the best compound for PV application since α in silicon is about 10^4 cm^{-1} while π-conjugated compounds usually reach 10^5 cm^{-1}. The inverse value of α corresponds to the absorption length, i.e. the average distance to cover for photons to be absorbed. This defines the thickness of materials required for efficient absorption devices, which is reduced for organic materials compared to silicon[27,33–35]; it is about one hundred nanometres for organic

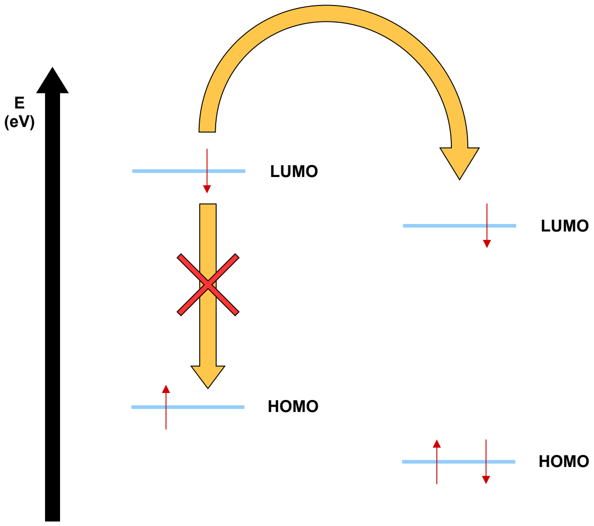

FIGURE 1.8: Scheme representing the competition between the radiative or non-radiative deexcitation versus electron transfer from the donor to the acceptor of another molecule.

devices.

1.3.5 Charge collection

When the molecule has an electron in a more energetic orbital, it is not a stable situation and the system wants to return to its ground state by emitting a photon or heat and allowing the electron to fall back into the HOMO. These two phenomena have to be avoided because they prevent us to collect the excited electron. The promoted electron leaves a hole behind, bonded together by electrostatic interactions, which is referred to as electron-hole pair or exciton. The energy amount needed to break these interactions ranges from 0.4 eV for polymer but can reach 1 eV for small molecule[36]. The strategy to break excitons is to blend a donor material with an acceptor compound to create an energy offset between their LUMOs and to separate the electron from the hole by overcoming the electrostatic interactions, see Fig.1.8. If the exciton is formed in the acceptor, there is a hole transfer from the HOMO of the donor to the HOMO of the acceptor[37].

For inorganic semiconductors, the process is slightly different since excitons are less stable but a chemical doping is still mandatory to separate charges instead of mixing two different compounds. The doping consist generally in adding impurities in the semiconductors to partially fill the conduction band or deplete the valence band. The first case ends up with a n-type doped semiconductor while the second one ends up in a p-type doped semiconductor[38]. A key parameter here is the Fermi level energy defined for metals at the top of the valence band; for non-doped semiconductors, it is typically set at mid height of the gap. By populating the conduction band or depopulating the valence band, the Fermi level is respectively shifting up or down.

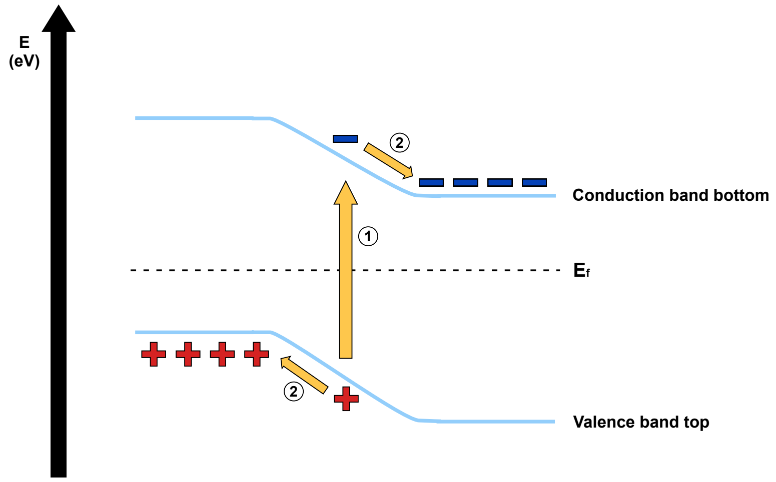

FIGURE 1.9: Scheme of a p-n junction at the bottom of the conduction band and top of the valence band. The first step is light absorption, promoting an electron in the conduction band and the second step is the charge separation mechanism thanks to the depletion layer.

The way to make a solar cell is to set-up a p-n junction, putting in contact both types of semiconductors. At the interface and over a few angströms, the Fermi levels will align following electron transfer from the n part to the p one, resulting in a depletion zone. This construction allows for charge separation via the built-in of an external electric field that will push electrons to the n zone and holes to the p zone[39], see Fig.1.9.

1.3.6 Organic photovoltaic devices

Now that we have understood the main features and physical principles behind the light energy transformation into electric energy, it is time to take a closer look on devices, especially OPV devices. It is composed of an active layer sandwiched between two inter-layers and by two electrodes to close the electrical system, see Fig.1.12.

In fact, there are two types of architecture, called direct vs inverted. Their origin comes from a historical conception because, at first, the ITO electrode served as anode, collecting holes, and the counter electrode as the cathode, collecting electrons. The main challenge occurring during the device construction is adding layers on top of the others without dissolving them during the deposition. At that time, there was a lack of materials adapted to be deposited on top of the active layer so that degradation coming from the electrode/active layer interface was not avoidable. Solutions were found by inverting the charge direction pathway and by discovering materials that do not dissolve the active layer and can be deposited on top of it[40,41].

Active layer

This part has to generate free charge carrier upon light absorption. It is generally composed of a mix of a conjugated polymer as p-type semiconductor with a π-conjugated molecule acting as n-type semiconductor, wisely chosen to match orbital energies according to the previously mentioned requirements. The versatility of organic chemistry allows to create a large variety of semiconductors in contrast to inorganic chemistry usually restrained in terms of compound nature or mixing.

The ideal architecture for such a layer consists in a bulk hetero-junction (BHJ), see Fig.1.10, to balance two important parameters: exciton dissociation rate and charge carrier mobility[42]. Both parameters are important for an efficient device but difficult to conciliate. The charge carrier mobility is optimised for a bi-layer structure because it relies on inter molecular orbital overlap. In fact, the charge has to to jump from a molecule to another of the same kind to reach progressively the electrode. However, charge generation is rare in such an architecture because there is only one interface between the donor and acceptor phase and the exciton diffusion length is about 10-15 nm. On the other hand, maximizing the exciton dissociation via a bulk heterojunction will reduce charge transport by enhancing the amount of energetic disorder in one phase, and hence by generating traps for free charge carriers[37].

Charges caught in a trap are likely to recombine, i.e. an electron stuck in a trap will recombine with nearby passing or trapped hole by radiative or non-radiative emission. The degree of charge recombination increases with low charge carrier mobility or poor charge dissociation at the interface, and is one of the most detrimental phenomena in OPV leading to weak performances.

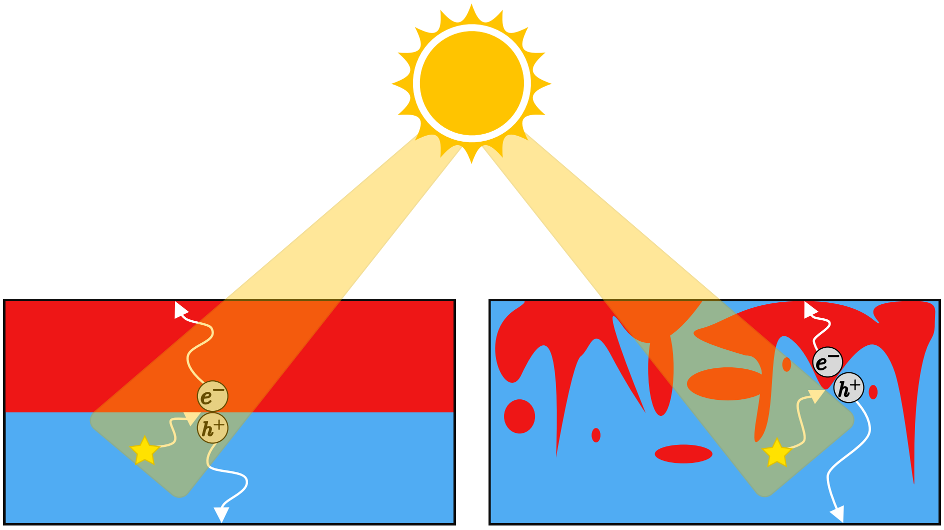

FIGURE 1.10: Scheme of a bi-layer device, on the left and a BHJ device, on the right. Exciton is represented by a yellow star and electron-hole pair by e^- and h^+ symbols.

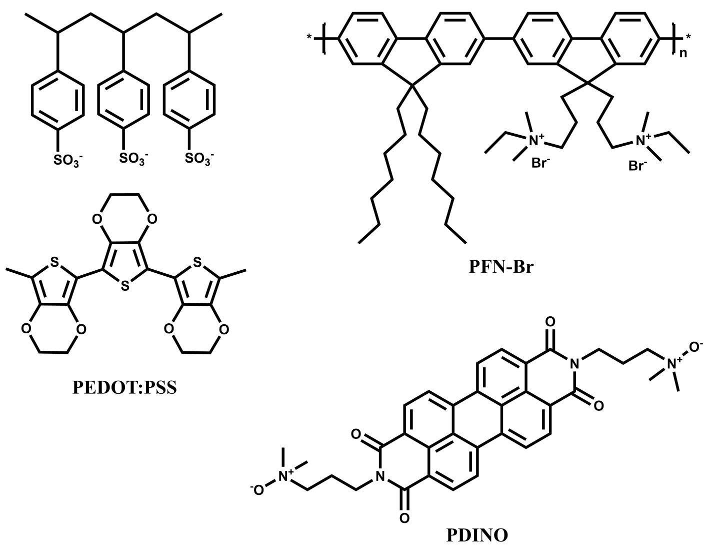

FIGURE 1.11: Chemical structures of main organic buffer layers

Inter-layers

Their goal is to set a driving force for the charge collection selectivity based on the energy of their valence and conduction band. The electron transport layer (ETL) will attract electrons by having its conduction band edge slightly lower than the acceptor LUMO with, at the same time, its valence band edge to deep to let holes pass. in opposition the hole transport layer (HTL) is tailored to let holes pass and prevent electrons to get in its conduction band. Common materials encountered are metallic oxides, polymers or small π-conjugated molecules, usually using ZnO, SnO_2, PEDOT:PSS, MoO_3, PDINO, PFN-Br,...[43–45]

Electrodes

Electrodes are important for charge collection with their work function ideally chosen with respect to the band edges of the inter-layers. Nevertheless, one of them needs to be transparent. it is typically made of indium oxide doped with tin, ITO (Indium Tin Oxide, In_2O_3:Sn). The indium oxide has a large gap, hence the transparency, but the replacement of certain In atoms by Sn atoms creates some occupied bands at the Fermi level that cross in certain k points the conduction band[46]. The counter electrode is usually reflective to rise the amount of photon absorbed, counting for 30% of the device performance. Materials used include Ag, Al or even Ca or Mg[47].

1.3.7 Electrical characterisation

Once the OPV device is built, one wants to measure its yield or its power conversion efficiency (PCE). For this purpose, the device is electrically connected to a generator in order to measure the electrical (P_{elec}) power generated for a known light output (P_{light}). Scientists have developed solar simulators to avoid depending on the actual

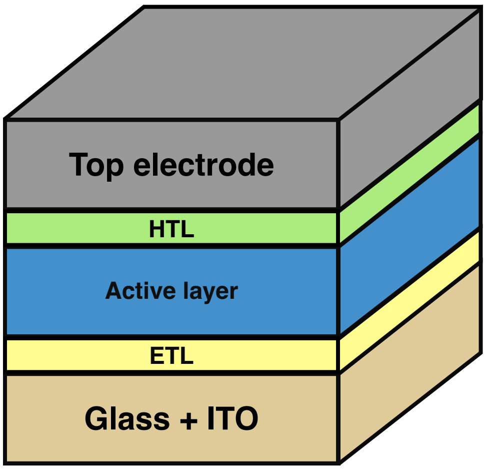

(A) Structure of an OPV device in an inverted architecture.

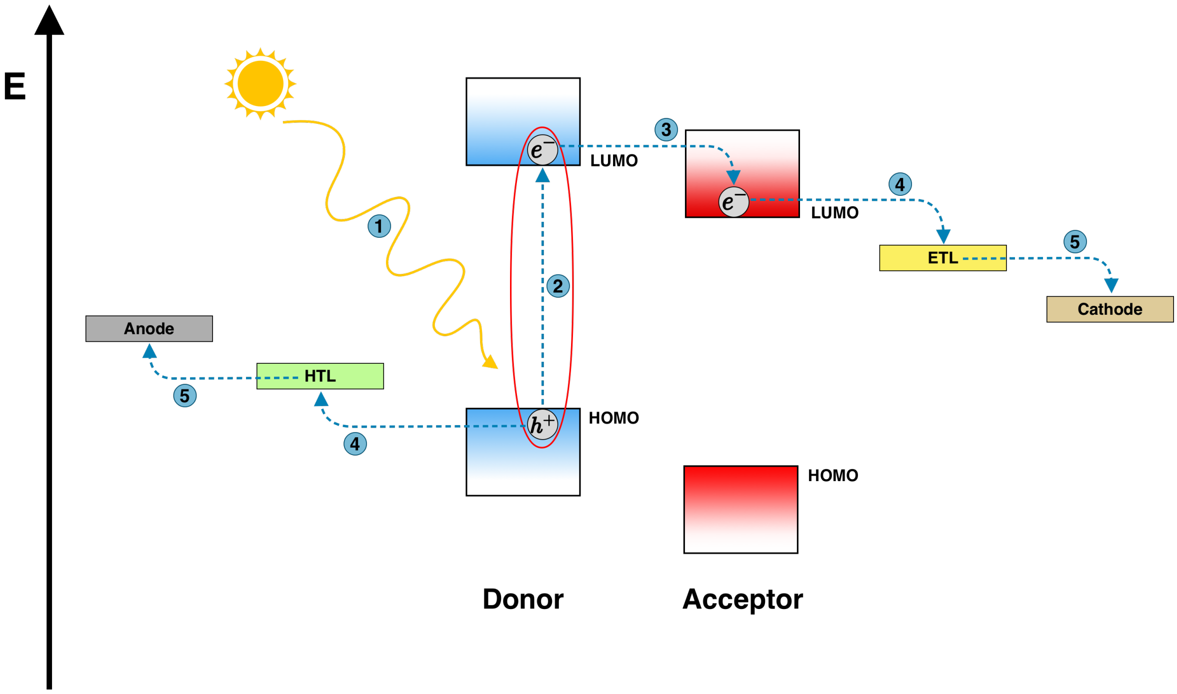

(B) Orbital/band energy of each layer in an OPV device showing how charges are generated and transported to each electrode for holes, h^+ and electrons, e^-. Only inter-layer levels matching accessible energy levels for each carrier type are represented, i.e. top valence band for holes and bottom conduction band for electrons Finally, electrodes are represented by their Fermi level. The light conversion process occurs in 5 steps: light absorption, exciton formation, exciton migration, exciton splitting, charges injected in inter-layers and charge collection at the electrode

FIGURE 1.12: Figure representing an OPV device (A) and its energetic diagram (B).

sunlight which is obviously not constant over days. The generated light spectrum refers to AM 1.5 conditions which means that air partial absorption and Earth's tilt (atmosphere thickness corresponding to 1.5 time that at equator latitude) is taken into account.

$$PCE = \frac{P_{elec}}{P_{light}} \text{ and } P_{light} = \frac{I_{lamp}}{S} \tag{1.1}$$

Where I_{lamp} stands for the lamp simulator intensity and S for the lit surface. Common target is set up at 100 mW/cm^2. A power is the result of the current received multiplied by the voltage applied but since the current generated depends on the device surface, the current density is most widely considered, see Eq.1.2.

$$P_{elec} = J * V \tag{1.2}$$

Since the PV effect relies on a P-N junction, devices behave as diodes and electrical response are then similar with a blocking regime and a passing regime. The device maximum output (P$_{max}$) occurs at the curve point conciliating maximal current (I$_{max}$) and voltage (V$_{max}$). Unfortunately, these two parameters are not directly accessible on the measured J/V curve and we need to introduce three new variables: short-circuit current (J$_{SC}$), open-circuit (V_{OC}) voltage and fill factor (FF), see Eq.1.3.

$$P_{max} = V_{OC} * J_{SC} * FF \tag{1.3}$$

Where V_{OC} corresponds to the potential needed to nullify the current, J_{SC} the current for an applied voltage equal to 0 V and FF to the area ratio between the theoretical maximum power square in blue (equal to $V_{OC} * J_{SC}$) and the effective maximum power square in yellow (equal to $V_{max} * I_{max}$). All these parameters are represented on the I-V curve in Fig.1.13. These three parameters depend on several factors[48,49]:

- J$_{SC}$: Absorption coefficient, exciton dissociation rate and charge transport
- V$_{OC}$: Energy difference between LUMO acceptor and HOMO donor and charge recombination rate
- FF: Interface quality between layers, donor:acceptor mixing quality in solid phase, BHJ homogeneity, ...

Even if one can tailor all these three parameters, there is still one important limitation called thermalisation. Indeed, if photons are too energetic they will promote the electron in a high-lying unoccupied level which will then get back to the LUMO or the bottom conduction band by emitting thermal energy. It means that the maximum accessible efficiency for a single p-n junction depends on the band gap height and is equal to 33% for a band gap of 1.1 eV, see Fig.1.13. This limit was found by Shockley and Queisser (S-Q)[50,51].

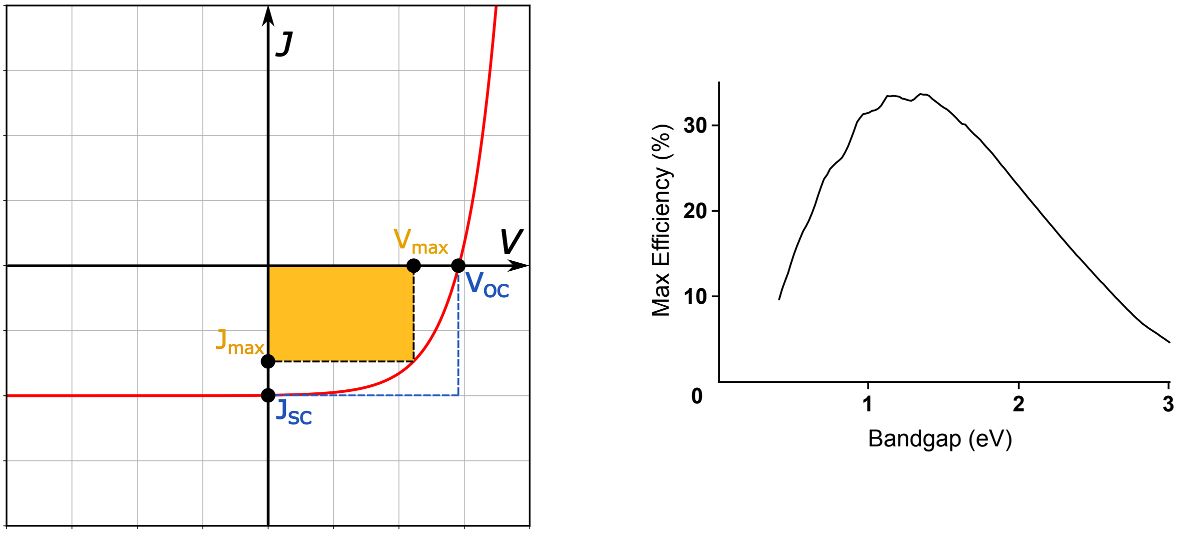

FIGURE 1.13: J/V curve featuring a typical PV electrical signature and its key parameters (A), and S-Q limit graph providing maximal efficiency accessible for a single p-n junction(B).

1.3.8 Important breakthrough

P3HT:PCBM

The first reportedly efficient OPV device was containing the following active layer blend: P3HT and PCBM. **P3HT**, or poly(3-hexylthiophene), is a polymer absorbing in the visible region, between 400 to 650 nm, and has an electronic band gap of 2.0 eV associated to a HOMO and a LUMO level at -5.0 eV and -3.0 eV respectively. **PC$_{61}$BM**, or [6,6] phenyl-C61-butyric acid methyl ester, in contrary does not absorb in the visible region but at 400 nm, in the ultra-violet (U-V) zone. It has a band gap of 2.2 eV associated to HOMO and LUMO energy levels lying at -6.0 eV and -4.2 eV respectively. P3HT plays the role of donor while PCBM is the acceptor.

The best values obtained for a single p-n junction is about 5%, with values of J_{SC}, V_{OC} and FF reaching 11 mA/cm2, 0,65 V and 54% respectively[52]. Considering device stability to light and heat, this blend turned out to be not successful to build long term efficient devices. Moreover, the energy yield is not very large and should be tuned to reach better values compared to the competing technologies.

In fact, problems come from PCBM in majority because it does not absorb visible light, has stability drawbacks and has a too deep LUMO. Finding an acceptor absorbing in the visible could improve J_{SC} values by increasing the amount of excitons generated. Stability problems comes from a dimerisation process occurring between PCBM molecules and cluster migration. This tends to create acceptor agglomerates and reduces the interface size, and hence leads to an exciton production rate falling down, reducing J_{SC} and FF factors[53,54].

Finally roughly 1 eV is lost in the exciton splitting process because the PCBM LUMO is too deep and chemical modification has not enough effect on electronic structure[55].

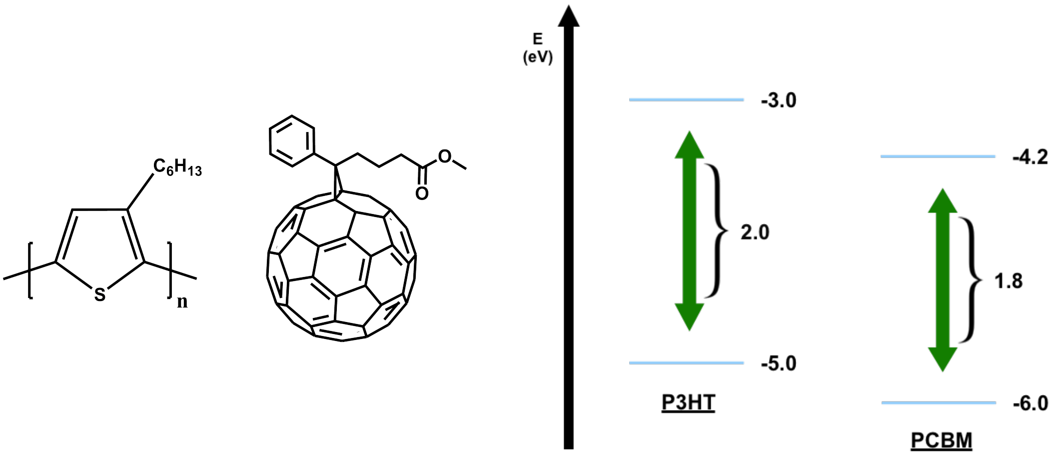

FIGURE 1.14: Chemical structure of P3HT (left) and PCBM (right). The chart represents their respective HOMO and LUMO energies

this results in a low V_{OC} value and then poor performances.

PTB7:PCBM

New blends launched the PTB7 donor polymer family with an optical bandg-ap allowing absorption until 785 nm and an electronic band gap of 1.6 eV. The HOMO and LUMO have respective their energy at -5.2 eV and -3.6 eV, leading to a larger donor HOMO acceptor LUMO separation, and hence a larger V_{OC} of 0.8 eV. The J_{SC} is also increased up 15 mA/cm^2 due to the better match of the absorption spectrum with the solar emission. FF stays around 60% because no improvements are brought by the new polymer in terms of interfacial quality. The resulting efficiency rises up to 9%[56–58].

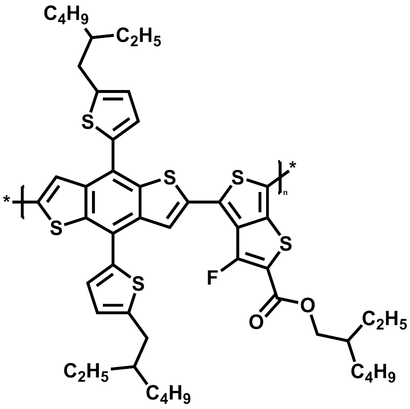

FIGURE 1.15: Chemical structure of the PTB7-Th polymer donor

Non-fullerene acceptor

A major breakthrough in OPV was the discovery of non fullerene acceptors (NFA), with a totally different molecular structure. Fullerene based acceptors were the only

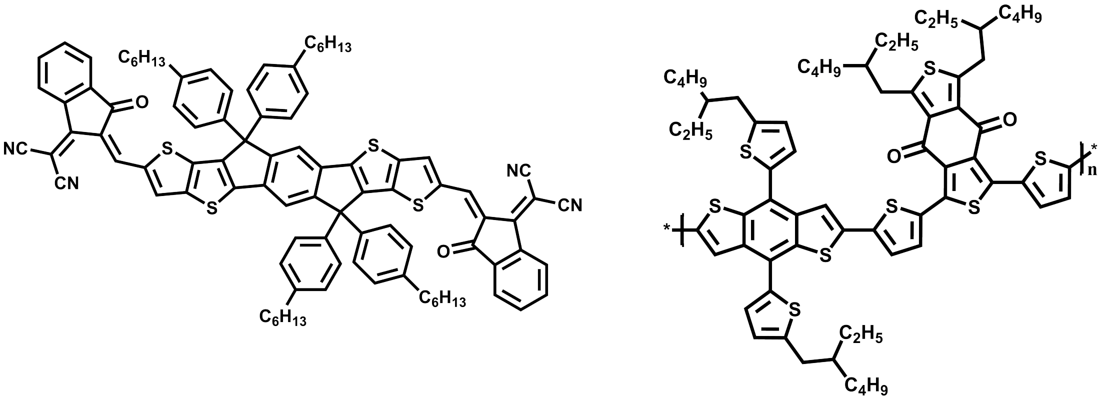

FIGURE 1.16: Chemical structures of donor and acceptor that have enabled above 10% yield in devices. On the left, ITIC NFA and on the right, PBDB-T donor polymer.

reliable option till then because of their relative good conductivity and their frontier orbital energy localisation. However, due to the previous cited drawbacks, performances using PCBM were capped and there was no other significant alternative because the molecular structure of C60 did not allow for a lot of chemical variations. Indeed, except C_{61} altered by a butyric acid methyl side chain corresponding to the PCBM molecule, reported similar molecules were $PC_{71}BM$ for better absorption properties, ICBA, $PC_{84}BM$, bis-PCBM,... all having very similar structure and electronic properties[59].

Attractive NFAs for solar cells primarily differ from fullerenic molecules by their planarity in opposition to the spherical shape of C_{61}. Moreover, their absorption band is located in the visible region, precisely in the red zone, near 700 nm allowing for the formation of excitons in the acceptor phase in addition to the donor phase, which thus boosts the current density values. The first widely studied NFA is called ITIC, i.e., 3,9bis(2-methylene-(3-(1,1 dicyanomethylene)-indanone))-5,5,11,11-tetrakis(4-hexylphenyl)-dithieno[2, 3d:2′,3′d′]-s-indaceno-[1,2-b:5,6-b′]-dithiophene[60].

Their frontier electronic levels are respectively located at -5.5 eV and -3.85, giving an electronic gap of 1.7 eV. Theoretically, V_{OC} should be improved by 0.35 V compared to PCBM but other recombination or deexcitation phenomena likely occurs, giving a value of 0.95 V. Since the light absorption is strongly improved, J_{SC} reaches 22.2 mA/cm^2. Finally, dimerisation reaction is avoided with these new acceptors and the planarity of the two components improves their interactions, which leads to better values of FF, reaching 82%. The PCE achieved with this blend has exceeded the 10% symbolic value[61].

The ITIC structure is somewhat particular in view of its A-D-A architecture: a central donor group end-capped by two external acceptor groups, resulting in a more delocalised LUMO but centralised HOMO. This architecture should allow for easier intramolecular charge separation, and hence easier creation of a charge transfer state (CT). This structure is also responsible of a red shift in the spectral signature.

Besides, better mixing and interactions give a higher charge mobility inside the active layer. The choice of inter-layers remains very important by tuning the key factor values.

More importantly, NFAs show better capacity to be chemically tuned because the backbone is more suitable for chemical modifications. One can easily change the core length or conjugation while adding hetero elements on the edges like F, Cl, etc. with a higher electro-attractor character, or even change the edge group structure. In this way, a large databank of NFA was created to best match a large set of donor polymers, improve active layer properties and enable higher performances[62].

In parallel, since the PTB7-Th polymer did not mix well with ITIC; the development of PBDB-T and similar donor polymers was initiated, providing better yield values, see Fig.1.16. This polymer is rather a copolymer because it has a donor and an acceptor part, similarly as an ITIC molecule, composed of a acceptor benzodithiophene-dione (BDD) part and a donor alkylthienyl-benzodithiophene (BDTT) part applying the same architecture as in NFA in the polymer backbone has enabled higher PCE values reaching 15%[63].

BTP derivatives

Recent works pointed to particular NFA structures: BTP derivatives with an A-D-A′-D-A structure. The A′ moiety has a weaker acceptor power but has the special feature of improving conjugation along the core, see Fig.1.17[64–66]. Moreover it appears that the optical absorption yields a stronger red shift in the solid phase because of improved molecular stacking. This ability to stack also promotes higher electron mobility and improves J_{SC} and FF . It is the most efficient structure until now, unlocking PCE reaching 19.2% with its fluorinated derivative, BTP-4F or Y6 combined with the PM6 co-polymer.[67].

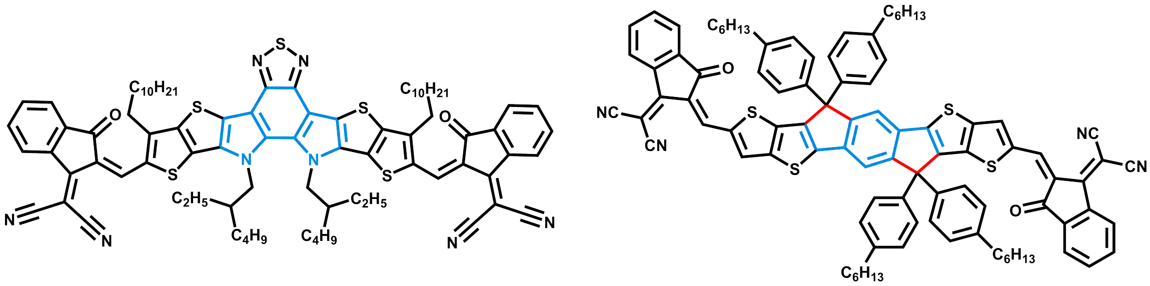

FIGURE 1.17: BTP (left) vs ITIC (right) molecular structure in terms of conjugation showing better delocalisation in case of BTP than ITIC. Blue highlighted bonds are available when red are not for π-electron delocalisation.

1.4 Thermoelectricity

1.4.1 Historical context

Besides the conversion of light into electricity, it is also possible to transform heat in electricity. This was discovered by Thomas Seebeck in 1821 and explained by Alessandro Volta, seeing a muscle contraction in a frog dead body plunged in two glasses of water at a different temperature. The Seebeck effect is the capability of a material to generate electricity from a gradient of temperature or inversely[68–71].

Other scientists have crossed the field of thermoelectricity, trying to improve thermoelectric generator efficiency, such as Ørsted and Fourier using bismuth and antimony, or Nobili and Melloni who were the first manufacturers of a thermoelectric pile with 36 assembled thermocouples (TE) pile[72,73]. Commercial prospects appeared for devices directly connected to a source of heat as a thermoelectric generator (TEG) but did not get a lot of success since they consumed a lot of fuel, were lacking reliability, and were massive equipments[74,75].

The development of high quality inorganic semiconductors during WW2 has strongly impacted the field of TEG. 5% efficiency was recorded using PbS and ZnSb[76] materials but the toxic nature of these materials and their rarity are still major obstacles for everyday applications. Nowadays, TEG applications remain in several niche domains such as aeronautics or medicine[77–79].

In the actual climate crisis and the search for renewable energy, TEGs are back in the spotlight through the development of nanotechnologies[80,81]. Since 70% of the energy investment in power plants and factories are lost as heat, TEGs are already good at reducing this amount of wasted energy but efforts must still be done in TE research to reach higher efficiency[82].

1.4.2 Characterisation

An effective TEG requires a poor thermal conductivity, a low resistivity and a high Seebeck coefficient[83,84]. One defines the figure of merit ZT of a thermocouple as follows:

$$Z = \frac{S^2\sigma}{\kappa} \tag{1.4}$$

Where σ [S m^{-1}] is the electric conductivity, κ [W m^{-1} K^{-1}], the thermal conductivity and S the Seebeck coefficient [V K^{-1}]. $S^2\sigma$ is usually denoted as the power factor PF [W m^{-1} K^{-2}]. Since Z varies as a function of the temperature, a dimensionless figure of merit is defined as follows:

$$zT = \frac{S^2\sigma}{\kappa} \cdot T \tag{1.5}$$

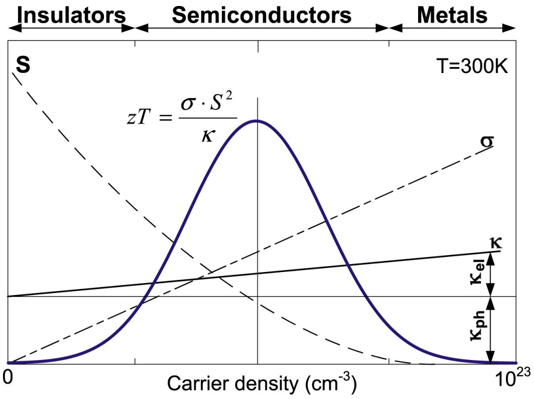

FIGURE 1.18: Thermoelectric parameters evolution as a function of the carrier density, divided in three material classes: insulators, semiconductors and metals[85].

where T [K] is the average temperature between the hot and cold parts of the thermocouple. Optimising zT parameters is none but an easy task since the power factor relies on an interconnected set of parameters depending on he carrier density. Increasing the charge carrier density clearly leads to a higher PF. On the other hand, the thermal conductivity is in fact divided into two components, lattice and electronic components $\kappa = \kappa_{ph} + \kappa_{el}$. Indeed, contribution of free electrons is larger than the phonons in the lattice, as resumed in fig.1.18.

Trade-off is then mandatory to obtain efficient TEGs. Nowadays, the most efficient choice is a heavily doped inorganic semiconductor, such as Bi_2Te_3 or Sb_2Te_3[86]with carrier density ranging from 10^{19} to 10^{21} carriers per cm^3. Thermal to electricity conversion efficiency is obtained in the following equation using zT. Where T[K] is the operating device average temperature.

$$\eta = \frac{T_h - T_c}{T_c} \cdot \frac{\sqrt{1+zT} - 1}{\sqrt{1+zT} + \frac{T_c}{T_h}} \tag{1.6}$$

Basically, the formula includes a Carnot's cycle efficiency (left term) in such a way that a TEG approaches the Carnot's efficiency when $zT \to \infty$. Increasing the temperature gradient, improves the efficiency. As a comparison, with a zT value of $\approx$ 3, the temperature gradient required to overtake conventional engine efficiency is $\approx$ 700 K. State of the art bulk materials for thermoelectric application show a zT value of 2.2[87]while commercial TEGs have an efficiency of about 10% under $\Delta T = 200$K.

1.4.3 TEG driving force

A TEG consists in several thermocouples serially linked electrically but parallelly linked with respect to the gradient of temperature. To explain the electricity generation process, let us recall the representation of inorganic semiconductors from section 1.3.5.

Applying a temperature gradient gives kinetic energy to charge carriers whi-ch will cause a charge migration from the hot side to the cold side. This phenomenon creates a difference of potential because of the higher charge carrier density, either electrons or holes, at the cold extremity leading to an electrical current. In a quantum description, electrons and holes are Fermion particles and obey to Fermi-Dirac statistics, see eq. 1.7

$$f(E) = \frac{1}{e^{\frac{(E-E_F)}{kT}} + 1} \tag{1.7}$$

Hot charge carriers are thus occupying higher energy states while cold carriers lay in lower energy states. There is a "will" of hot carriers to reach the colder energy states, as represented in fig.1.19. Equilibrium is reached when the electrochemical potential for diffusion is compensated by electrostatic repulsion resulting from build-up charges. To obtain a significant current value, a TEG contains generally between 10 and 100 thermocouples depending on the power output required[88,89].

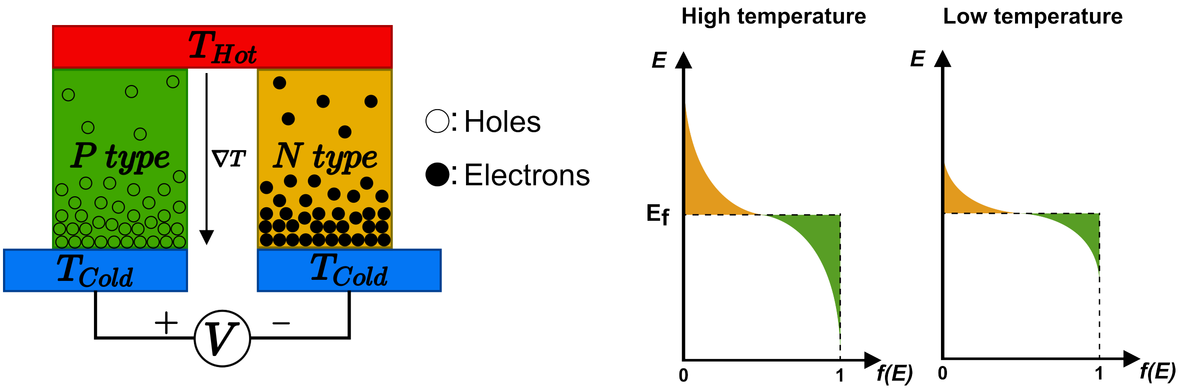

FIGURE 1.19: On the left, a schematic representation of a thermocouple and charge carrier spatial distribution in both n-type and p-type semiconductors. On the right, the Fermi-Dirac energy distribution for electrons in orange and holes in green.

1.4.4 Enhancement strategies

Many attempts were made to create more efficient TEGs. In this section, I will summarize the most important of them, from new conception methods to materials employed for this technology.

One of the most promising technology for TE applications was the emergence of nanotechnology and low dimensional materials. For instance, nano-structuration of Bi_2Te_3 has raised its figure of merit by a factor of thirteen[90] because the electronic density of states changes drastically in shape as we go from a 3D to a 2D to a 1D material. This improves electrical conductivity though hole and electron transport becomes asymmetric[91].

At the same time, transport for both charge carriers and phonons has been theorised by Slack[92] under the "Phonon-Glass-Electron-Crystal" (PGEC) design strategy. Carrier transport has to show a crystal-like behaviour while phonon transport has to show a glass-like behaviour, respectively. Emerging structures have then been developed in a cage-like architecture able to accept host atoms for independent charge and thermal transport tuning. Indeed, these heavy filler atoms are not strongly bonded to the framework because of their large radius which attenuates lattice thermal vibration because of undergoing localised and isolated vibrations. The most famous PGEC structures are skutterudites and clathrates.

1.4.5 Organic thermoelectrics - charge carrier transport

Similarly to OPV, organic compounds have been introduced in TEG as alternative to inorganic compounds to reduce the carbon foot print and enhance their development by offering new features that inorganic compounds do not have. Indeed, metal and alloy atomic elements are highly expensive because of their low abundance. Besides, they usually exhibits a certain degree of toxicity, being harmful to the environment. Finally, inorganic materials are often rigid which makes it harder to capture heat from irregular shapes.

In counter part, organic materials are made of lot more abundant constituents. Plus, they can be processed at room temperature, reducing their energy costs. Conjugated polymers are also lightweight and flexible extending their use to harvest heat from different shapes. Moreover, they often exhibit lower toxicity and are therefore more environment friendly. Finally their chemical structure can be tuned to tailor their TE efficiency.

As previously shown, one can decide to improve either the charge carrier conductivity or to reduce the thermal conductivity as tuning strategy[93]. Organic semiconductors typically show low electrical conductivity ($10^{-9} - 10^{-8}$ S cm^{-1}) but also low thermal conductivity (lower than 1 W m^{-1} K^{-1}), about one or two orders of magnitude lower than their inorganic counterparts. Obviously, their thermal resistance is not similar to inorganic TE and applications are restrained to under 500K temperature conditions[91,94,95].

The first option to increase the efficiency of organic thermoelectrics (OTE) is to increase the charge carrier concentration by doping, as already explained previously. For organic molecules, doping does not consist in introducing impurities or defects in a crystal structure to create intermediate electronic levels (gap states) between the valence and the conduction band. Doping is rather chemically operated by adding molecular dopants with matching molecular orbitals to partially fill or deplete unoccupied or occupied energy levels from the OTE material[96].

P-type conjugated polymer[97] has already exhibited a zT value higher than 1 at room temperature, approaching the zT value of Bi_2Te_3 as best p-doped candidate. A slower progress is seen for n-doped systems due to air and moisture instabili-ty[98].

N-type semiconductor polymer though approaches 0.5 at room temperature[99]. Nevertheless, there are strong downsides to doping such as local intermolecular packing disruption, or phase segregation creating high and low conductivity regions. Both effects are detrimental for the transport of charges[96,100].

Interestingly, alternative lays in the improvement of charge mobility which can increase the electrical conductivity while keeping the Seebeck coefficient relatively constant[91,101]. This parameter is strongly affected by the molecular and supramolecular structure and needs to be tailored to reach desirable values of conductivity and charge mobility (around 10 S cm^{-1} and 0.01 cm^2 V^{-1} s^{-1} respectively). Organic compounds are mostly made of carbon atoms and only π electrons are involved in the charge transport due to their small binding energies. Their bulk arrangement is driven through weak intermolecular interactions, such as π-π interactions, van der Waals interaction or hydrogen bonds. Their electronic structure is described through frontier energy levels due to these weak interactions, as described in section 1.3.3.

There are two main models for electronic transport, related to the bulk arrangement: band-like and hopping model[102]. Hopping occurs in disordered materials, yielding low-mobility OSCs ($\mu \ll 1$ cm^2 V^{-1} s^{-1}). Here, molecular orbitals slightly overlap enabling carrier transport only by hopping between localised sites by a thermally activated process. In ordered and high-mobility systems (($\mu \gg 1$ cm^2 V^{-1} s^{-1}), HOMO and LUMO orbitals overlap better and form electronic bands (with a width typically over 100 meV) to transport carriers delocalised over several molecules in a so-called band-like transport; the spatial extent of the charge carriers is actually driven by the phonons of the network.

In the case of OSC, they usually have an intermediate behaviour between these two models since they are composed of polycrystalline areas in an amorphous matrix. This creates complex microstructures that make the scale of the theoretical description an important parameter for charge transport. At the molecular scale, having a planar structure is well known to favour intermolecular interactions between neighbours and enhance charge mobility while at the microscopic scale, a conformation is adopted to reduce hopping barrier for carrier for intra and inter chemical species paths. Finally, at the macroscopic scale, the critical parameter is the carrier ability to transit from amorphous to crystalline domains, drastically affecting the charge carrier transport mechanisms[103].

1.4.6 Organic thermoelectrics - thermal transport

Low κ values from OSC is a major asset for TE application but the thermal transport mechanisms still need to be fully understood. Description are generally conducted through theoretical calculations as well as practical experiments. A description of current thermal transport knowledge will be presented in the following paragraph but no further studies have been performed in this work

Experimentally, thermal conductivity can be measured by using frequency-domain thermoreflectance, time-domain thermoreflectance, membrane-bas-ed AC calorimetry, suspended micro bridge method, scanning thermal microscopy, Raman probing method, infrared thermography,…[104] Despite the numerous possibilities for thermal transport measurements, thermal conductivity is tricky to measure with consistency and interest for OSC has not been seriously considered in last decades.

Thermal conductivity is defined in eq.1.8 by Fourier's heat conduction equation, where $\dot{Q}$ is the heat flux passing through the sample, Δl is the sample length and ΔT is the difference of temperature across the sample. Measurement uncertainty comes from parasitic heat transfer through radiative exchange with the surroundings and thermal resistance losses at interfaces[105,106].

$$\dot{Q} = -\kappa \frac{\Delta T}{\Delta l} \tag{1.8}$$

Another major limitation comes from the sample dimensions. Even with well established probing standards, the overall uncertainty can reach up to 20%. When samples have reduced dimensions, such as 2D or 1D materials, uncertainty is worse and experiments require extra care to be consistent[104].

At the same time, OSCs are typically anisotropic materials in terms of many properties, as it is the case for thermal conductivity. This means that the directionality of measurement is important. Most obtained values are reported for the out-of-plane direction because of probing difficulty inherent to previously cited methods[107]. Reported values lie below 1 W m^{-1} K^{-1}.

In solid systems, heat carriers are composed of electrons (κ_e) and lattice vibrations (κ_L). In analogy to electrons, "phonons" can be seen as quasi-particles to describe quantum of lattice vibrations. Hence, phonons and electrons can collide and propagate heat through thermal transfer mechanisms. κ is then expressed in eq.1.9.

$$\kappa = \kappa_e + \kappa_L = L_0 \sigma T \; + \; \frac{1}{3} C_v \lambda_{MFP} v_0 \tag{1.9}$$

where L_0 is the Lorentz number, C_v is the volumetric heat capacity, v_0 is the speed of sound in a solid, and λ_{MFP} is the phonon free mean path. For neutral and weakly doped OTEs, literature points to a higher contribution from the lattice than the electronic component. Heat conduction study in OSCs can be resumed as understanding phonon scattering processes that involve phonon-boundary, phonon-phonon, phonon-defect,…scattering phenomena[108]. Matthiessen's rule decomposes the total relaxation time of a phonon (τ_{total}) in eq.1.10.

$$\frac{1}{\tau_{total}} = \frac{1}{\tau_{boundary}} + \frac{1}{\tau_{ph-ph}} + \frac{1}{\tau_{defect}} + \dots \tag{1.10}$$

The following paragraphs will describe phonon scatterer contributions. A structural defect that is most often created during material processing is the grain boundary with sizes ranging between few tens to hundreds of nanometres[91]. It has been demonstrated that thermal conductivity at low temperature is significantly reduced when increasing the number of interfaces. Heat carrying phonons have mostly long wavelengths which help them to dodge small defects.

The second term of Matthiessen's rule stands for phonon-phonon Umklapp (U-) processes. This mechanism is known to be non negligible for both crystalline and amorphous inorganic as well as organic materials. By increasing the temperature, new phonons are massively generated and their free mean path are accordingly reduced. The U-process is responsible of $\kappa \approx \frac{1}{T}$ temperature trend[109,110].

Other scattering defects, such as vacancies or isotopic substitution, has been demonstrated to also affect thermal conductivity. Scaling law has been established to be $\kappa \approx n_v^{-\alpha}$[111], where n_v is the vacancy concentration and the exponent α is related to the molecular chemical structure. Dopant has been shown to be responsible for phonon free mean path reduction by a factor of three[112].

Apart from the previous phonon scattering sources, there are many other processes to reduce thermal conductivity in OTE, for instance, by modifying the molecular structure or the supramolecular arrangement. Studies performed on C_{60} and derivatives like PCBM or PCBNB highlight the role of side chains in thermal conductivity, with low experimental κ values[113] around 0.05 W m^{-1} K^{-1}.

1.5 Outlines of the thesis

Nowadays, a large quantity of OSC molecules is available and have been studied by scientists. Most of them have participated to the best performances race towards the best device for energy production. Nevertheless, only trial and error methods were followed with a limited knowledge on the structure-property relationships.

This work aims to take part in a global structure-properties relationship study to have a better understanding of the compound efficiency and limitations. In this context, I will divide my work into three axes, theoretical simulations, properties characterisation and device fabrication to approach several important aspects, sometimes poorly treated in the literature.

First of all, the theoretical simulations involve the atomistic modelling of the different systems under study. All studied molecules are drawn with graphical interfaces before performing quantum-chemical calculations and access their electronic properties. These calculations can predict some key features such as the efficiency of light absorption or the energy level evolution versus V_{OC} values.

Secondly, the optical properties are characterised and supplemented by morphological data taken by AFM and impedance spectroscopy (IS) measurements. It allows us to understand the best device conception conditions, e.g. regarding the solvent used, the molecule concentration, the donor acceptor ratio or even the drying kinetics through the film roughness. Accessing charge mobility data from IS also sheds light on the importance of deposition conditions and techniques.

Finally, building my own experimental solar cells let me face the big challenges of device conception and to follow he properties extracted from individual molecules to their actual behaviour in a complex medium. This will light up challenges behind the molecule design to obtain efficient devices by relating all the properties required and the limitations encountered.

Moreover, I will also approach the stability criteria since keeping good performances for a long term period is mandatory for industrial production. This part will talk about photochemical degradation in inert atmosphere and ambient air to gather information about chemical reaction pathways.

In view of the interest of OSCs for thermoelectricity, some thermoelectric key parameters controlling heat transport and charge transport will be evaluated by molecular mechanics and molecular dynamics simulations method and DFT calculations, respectively. Orbital overlapping between molecules and thermal conductivity will be probed to independently describe charge carrier mobility and phonon propagation directionality in a crystal cell.

All of these aspects will be addressed by focusing on molecules from ITIC and Y families because of their phenomenal success in the OPV scientific community. I will consider several candidates with modified part in their structures such as side-chains, end groups and core groups. This would help us to assess the impact of the chemical structure on photovoltaic and thermoelectric underlying properties and device performances.

Chapter 2

Methodology

2.1 Theoretical simulations

This section will describe the strategy that I used to collect my theoretical data and analyse them. Since this work mixes both theoretical and experimental approaches, I will start by describing the simulation techniques allowing us to calculate and optimize molecular geometries and compute on that basis molecular orbitals, optical transitions, charge distributions and charge transfer integrals. This has been achieved by using the Gaussian 16 and GaussView 6.0[114,115] and ADF software[116] . Besides, molecular dynamics (MD) simulations were also performed on crystal structure to heat transport at a larger scale. These simulations were carried out with the Materials Studio and LAMMPS software[117].

2.1.1 Density functional theory

Quantum mechanics allows for the description of the infinitely small world for systems not subjected to relativity[118,119]. All quantum physics rules rely on a probabilistic description; for example, in chemistry, an electronic orbital describes a volume in which the electron has 95% probability of presence.

Nevertheless, such tiny bodies are difficult to describe because of the wave-particle duality which implies that they behave like particles but also like waves at the same time. Since wave physics is completely different from physics based on particles, it is mandatory to make a choice. In chemistry, we often use a wave-like description, by resolving Schrödinger's equation, see eq.2.1.

$$H\Psi_i(r_n, R_N) = E_i\Psi_i(r_n, R_N) \tag{2.1}$$

Ψ_i is the total wave function of our system which integer all of its eigenstates and eigenvalues. In our world, everything exists in a three dimensional space, so that the coordinate number equals 3N + 3n , with N the number of nuclei and n the number of electrons. H is the Hamiltonian operator used to access the system energies; it has a kinetic and potential component and is applied to each particle, see eq.2.2.

$$H = -\sum_i \frac{1}{2M_i}\nabla_i^2 - \sum_j \frac{1}{2}\nabla_j^2 - \sum_i\sum_j \frac{Z_i}{r_{ij}} + \sum_i\sum_{i'\neq i} \frac{Z_i Z_{i'}}{r_{ii'}} + \sum_j\sum_{j'\neq j} \frac{1}{r_{jj'}} \tag{2.2}$$

$$= T_N + T_e + V_{eN} + V_{NN} + V_{ee} \tag{2.3}$$

The first and second terms, T_N and T_e, correspond to the kinetic energy of nuclei and electrons respectively. The third one, V_{eN}, is the Coulomb attraction between them while the fourth and fifth terms, V_{NN} and V_{ee} are the electrostatic repulsion between nuclei and electrons, respectively. Unfortunately, such an equation is impossible to solve because it involves too many degrees of freedom and thus requires approximations for simplification. The first one is the Born-Oppenheimer approximation that allows us to get rid of the solely nuclear depending components, i.e. T_N and V_{NN}.

Dealing with electronic repulsion is a tricky issue since their motions are interrelated. Douglas Hartree and Vladimir Fock describe electron interactions by considering that the other electrons create an average electrostatic field. Reaching the Hartree-Fock equations requires the application of the variational theorem which states that the exact fundamental state energy state is associated to an exact wave function and that any trial wave function will lead to an approximative energy higher than exact value, see eq.2.4.

$$E_{appr} = \int \Psi_{trial}\, H\, \Psi_{trial}\, d\tau > \int \Psi_{exact}\, H\, \Psi_{exact} = E_{exact} \tag{2.4}$$

$$J(\Psi) = \int \Psi(H - E_0)\Psi d\tau \tag{2.5}$$

To apply this variational theorem, one define a functional $J(\Psi)$, see eq.2.5. The application of the variational theorem shows that the function Ψ that best describes the system cancel the first derivative of $J(\Psi)$, see eq.2.6. Thus, in order to vary Ψ one needs to vary $J(\Psi)$ by applying an arbitrary function of Ψ $(\delta\Psi)$, see eq.2.6.

$$J(\Psi + \delta\Psi) = \int (\Psi + \delta\Psi)(H - E_0)(\Psi + \delta\Psi)d\tau \tag{2.6}$$

$$J(\Psi + \delta\Psi) = \int \Psi(H - E_0)\Psi d\tau + 2\int \delta\Psi(H - E_0)\Psi d\tau + \int \delta\Psi(H - E_0)\delta\Psi\, d\tau$$

$$J(\Psi + \delta\Psi) = J + 2\delta J + \delta J^2$$

Generalising for any closed-shell system and using a Slater determinant to describe the antisymmetry of the wave function, leads to the Hartree-Fock (H-F) operator in eq.2.7. h_i is the Hamiltonian for a single electron, J_m is the Coulomb operator accounting for Coulomb repulsion with the average spatial distribution of the other electrons and K is the exchange operator reflecting Pauli forces that prevent electrons of same spin to lie in the same region of space. It is purely related to quantum effects and does not have an equivalent in classical physics.

As shown in eq.2.8, there is a constrain in the H-F formalism. The Fock operator is defined by orbitals for the J and K terms but orbitals are only obtained by resolving the equation. The solution is to use an arbitrary wave function as starting point to define the operators and to use the solutions as new starting point to get progressively closer to the reality; it is an iterative calculation process leading to a so-called Self Consistent field. The final result is obtained when the difference in energy between injected wave function and resulting wave function is within the range of the selected threshold. The H-F method can also consider systems with several atoms, i.e. molecules.

$$f_i = h_i + \sum_{m}^{occ.\ orb.} [2J_m(r_i) - K_m(r_i)] \tag{2.7}$$

$$f_i\phi_i(r) = \epsilon_i\phi_i(r) \tag{2.8}$$

Molecular orbitals are then defined as a Linear Combination of Atomic Orbitals (LCAO), see eq.2.9, where c_{im} is the coefficient that defines the $i - th$ atomic orbital weight χ_i in the LCAO expansion.

$$\phi_m = \sum_{i=1}^{N_0} c_{im}\chi_i \tag{2.9}$$

The H-F method is useful to perform geometry optimisations, orbital energy level estimation, taking into account various media via their dielectric constant, spectral simulations (like UV-vis, infrared, RMN,...). Nevertheless, it suffers from several limitations such as the correlation error defined as the difference between the exact energy and that obtained by H-F. This error is associated to the Coulomb operator because of the average electrostatic field that allows only for an average description of Coulomb interactions in the system, and thus misses the instantaneous electron correlation.

Here is a short example demonstrating its impact. Consider a dihydrogen molecule; the atomic separation probability described by H-F shows 50% chance of homolytic and 50% chance of heterolytic dissociation while experiment shows only the homolytic pathway. To cure the drawbacks of HF, several physicists have worked quite independently on another theory centralised on the electronic density and called Density Functional Theory (DFT).

DFT has the first advantage to simplify the calculations because the H-F wave function is based on 4N dimensions (when including the spin) while electronic density is associated to a volume, hence three coordinates. The density relies on the number of electrons n_j in occupied orbitals ϕ_j, see eq.2.10.

$$\rho(r) = \sum_{j}^{occ.orb.} n_j \phi_j(r)^2 \tag{2.10}$$

Before going further, it is important to demonstrate the matching between this theory and H-F. The main information required to obtain wave functions are:

1. Number of electrons
2. Atomic positions
3. Nuclear charges

The integration of electronic density over space gives us the number of electrons (1) ; the spatial distribution of the electronic density forms a cusp at the nucleus position, giving information about atomic positions (2) ; knowing both previous data, number of electrons and atomic positions, it is easy to predict core charges (3). This confirms that the electronic density is a relevant parameter since it gives access to the same data as those required to solve Schrödinger′s equation.

2.1.2 Hohenberg and Kohn's theorems

There are two founding theorems in DFT. The first one demonstrates that there is only one electronic density associated to a given external potential. Therefore, the ground state is described by one and only one electronic density.

$$E(\rho) = T_e(\rho) + V_{ee}(\rho) + V_{en}(\rho) \tag{2.11}$$

$$F_{HK}(\rho) = T_e(\rho) + V_{ee}(\rho) \tag{2.12}$$

The system total energy is equal to the sum of the electronic kinetic energy, the electron repulsion interaction and nuclear-electron attraction. F_{HK} is the Hohenberg and Kohn's functional that groups the purely electronic terms because the actual system is only defined by the electron-core term. The DFT challenge is to define F_{HK} because it is composed of exchange-correlation terms that are hard to determine.

The second theorem is similar to the variational theorem in quantum mechanics, *cfr. eq.2.4*. As previously described, it is very useful to help finding the best trial function to get as close as possible to reality, see eq.2.13.

$$E_0(\rho) \leq E(\rho') = T(\rho') + V_{ee}('\rho') + V_{ext}(\rho') \tag{2.13}$$

2.1.3 Kohn-Sham's method

A key target of this method is to evaluate the kinetic energy term. This is done by considering a fictive system that has the same electronic density but where electrons are not interacting. A Hamiltonian with separated variables can be defined for this fictive system in eq.2.14 with $f^{KS}(r_i)$, the Kohn-Sham operator for one electron. One can solve the one electron Kohn-Sham equation to access orbitals and their energies of the fictive system, see eq.2.15 applying the constrain that the fictive and real systems have the same electronic density, see eq.2.16.

$$H_S = -\frac{1}{2}\sum_i \nabla_i^2 + \sum_i V_S(r_i) = \sum_i f^{KS}(r_i) \tag{2.14}$$

$$f^{KS}\phi_i = \epsilon_i \phi_i \tag{2.15}$$

$$\rho^{KS} = \sum_i \phi_i^2 = \rho_0 \tag{2.16}$$

To connect both systems, we need to define a fictive potential in the Kohn-Sham equations obtained by applying the variational principle in both systems. One can then access the energy of the real system by introducing the kinetic energy of the fictive system and a correction, see eq.2.17. Here, $T_f(\rho)$ is the kinetic energy of the non interacting electrons, $V_{ee}(\rho) = J(\rho) + V_{nc}(\rho)$ with $J(\rho)$ the classic Coulomb repulsion and $V_{nc}(\rho)$ non classical electron interaction, $V_{en}(\rho)$ is the nucleus-electron interaction and $T_c(\rho)$ is a correction of $T_f(\rho)$ including electron correlation. $T_c(\rho)$ and $V_{nc}(\rho)$ are finally grouped under a unique term called *exchange correlation energy*, $E_{XC}(\rho)$ but its exact expression is not known.

$$E_{real}(\rho) = T_f(\rho) + \int V_{ee}(r)\rho(r)dr^3 + \int V_{ext}(r)\rho(r)dr^3 + T_c(\rho) \tag{2.17}$$

$$E_{fic}(\rho) = \int V_S(r)\rho(r)dr^3 + T_f(\rho) \tag{2.18}$$

in eq.2.18, the energy of the fictive system sums the kinetic energy $T_f(\rho)$ of non-interacting electrons and energy integrated from the fictive potential $V_S(r)$ applied to the electronic density $\rho(r)$. By cancelling the first derivative of the energy (i.e., using the variation principle) and equalizing the two expressions, one obtain $V_S(r)$. The Kohn-Sham operator can now be expressed as in eq.2.19. It gives access to the electronic structure of the fictive system, the electronic density in the ground state shared by both systems thanks to eq.2.16. The first term describes the kinetic energy of an electron in the fictive system, the second term is the nucleus-electron interaction potential, the third term is the exchange-correlation potential and the last one, the classical part of the interaction potential between electrons.

$$f^{KS} = -\frac{1}{2}\nabla_i^2 + V_{ext}(r) + V_{XC} + \frac{\int \rho(r')\,dr'}{|r-r'|} \tag{2.19}$$

The results combine level energies and electronic density for the ground state. Nevertheless, since the effective potential depends on the density, solving such equations requires an iterative process similar to HF. *cfr.2.8*.

2.1.4 Exchange-correlation potential

There is no exact expression for this term and it needs approximations the closest possible to reality. There are several schemes like Local Density Approximation (LDA), Gradient Generalised Approximation (GGA) or even the use of hybrid functionals, mixing H-F and DFT theory to deal with this term.

The LDA formalism considers a homogeneous electron gas uniformly distributed on a positive surface; the number of electrons N tends toward infinity while ρ remains constant on each point of the surface. The exchange-correlation potential is then defined locally with the electronic density value, see eq.2.20. In fact, the exchange-correlation potential is always divided into the sum of its two components, the exchange potential and correlation potential. This approximation is very useful for crystalline solid systems, e.g. metals. GGA is a refinement of LDA by considering a density gradient in the E_{XC} term, see eq.2.21.

$$E_{xc}(LDA) = \int \rho(r)\ V_{XC}(\rho(r))\ dr \tag{2.20}$$

$$E_{xc}(GGA) = \int f(\rho, \nabla_\rho)\ dr \tag{2.21}$$

Finally, hybrid functionals include an exchange term expressed as in HF since it gives an analytical expression for it and tends to reduce the amount of self-interaction errors. For this work, we used the LC-ωHPBE functional adding a distinction between short range and long range interactions in the exchange term, see eq.2.22.

$$\frac{1}{r} = \frac{\alpha + \beta\, erf(\omega r)}{r} + \frac{1 - (\alpha + \beta\, erf(\omega r))}{r} \tag{2.22}$$

Where r is the interacting distance, α and β are functional parameters and ω is the system-dependent range switching parameter. For LC-ωHPBE functional, the mathematical expression of the exchange correlation term is expressed in eq.2.23.

$$\begin{aligned} E_{xc} =& \alpha\ E_X^{HF,SR}(\omega) + (1-\alpha)E_X^{\omega PBE,SR}(\omega) + (\alpha+\beta)E_x^{\omega HF,LR} + \\ & (1-\alpha-\beta)E_X^{\omega PBE,LR} + E_c^{PBE} \end{aligned} \tag{2.23}$$

Where α is equal 0.2 and β = 0.8 to satisfy the condition implied in range separated functionals that $\alpha + \beta = 1$ for gas phase systems. The terms of the previous equation are described as follows:

1. $\alpha\ E_X^{HF,SR}(\omega)$: Part of the exchange term calculated at short range in α amount with H-F theory
2. $(1-\alpha)E_X^{\omega PBE,SR}(\omega)$: Part of the exchange term calculated at short range in $1-a$ amount with PBE DFT theory
3. $(\alpha+\beta)E_X^{\omega HF,LR}$: Part of the long range exchange term calculated with H-F theory.

4. $(1-\alpha-\beta)E_X^{\omega PBE,LR}$: Part of the exchange term calculated at long range with 100% HPBE DFT theory
5. E_C^{PBE}: Correlation term calculated at 100% with PBE DFT theory

Basically, LC-ωHPBE uses 20% H-F and 80% DFT exchange at short range and 100% H-F exchange at long range. To define the ω cut-off parameter, we used Koopman's theorem considering the HOMO energy as the ionisation potential (IP) and the LUMO energy as the electronic affinity (EA). IP corresponds to the energy required to extract an electron from the system while EA is the gain in energy by adding an electron to the system which results in $E_{gap} = E_{HOMO} - E_{LUMO} = IP - EA$. The best ω value is chosen to minimize the J(ω) value expressed in eq.2.24 and ensures that HOMO and LUMO energies are best effectively associated to IP and EA values.

$$J(\omega) = [\epsilon_{HOMO} + IP(\omega)]^2 \ + \ [\epsilon_{LUMO} + EA(\omega)]^2 \tag{2.24}$$

Since the medium (gas, solvent, condensed phase,. . .) has a strong influence on the ω parameter but not significantly on frontier orbital energies, we have adjusted the range separation according to the medium used for condensed phase calculations. The functional has then to account for the screened electronic interactions using the dielectric constant (ϵ) of the studied medium so that $\alpha + \beta = 1/\epsilon$.

2.1.5 Time dependent DFT

When it comes to absorption spectra simulations, there is another additional part to introduce[119,120]. DFT is very powerful to describe ground state properties but not so accurate for excitations. To access excited-state energies, one needs to solve the time-dependent Schrödinger equation, eq.2.26.

$$i\hbar\frac{\delta}{\delta t}\Psi(r,t) = H(t)\Psi(r_j,t) \tag{2.25}$$

$$\hat{\mathrm{H}}(\mathrm{t}) = \hat{T} + \hat{V}(t) + \hat{W} \tag{2.26}$$

The Runge-Gross theorem lets us treat this time dependency by showing a one to one correspondence between a time-dependent potential and a time-dependent density, making the electronic density still a central relevant quantity. Then, $v(r,t)$ and $v'(r,t)$ will lead to different density $\rho(r,t)$ and $\rho'(r,t)$ coming from the same Ψ_0 wave-function if they differ more than a time constant $c(t)$, see eq.2.28

$$v(r,t) - v'(r,t) \neq c(t) \tag{2.27}$$

$$v(r,t) = v[\rho,\Psi_0](r,t) \tag{2.28}$$

If the starting point is the ground state and the potential is turned on at t_0:

$$v(r,t) = v_0(r) + \theta(t-t_0)v_1(r,t) \tag{2.29}$$

The Van Leeuwen theorem relates to the Kohn-Sham approach as it allows to use a non interacting system that has the same time-dependent density as the studied system. Orbitals $\phi_j(r,t)$ are now satisfying the time-dependant Kohn-sham equations (eq.2.31).

$$\rho(r,t) = \sum_{j=1}^{N} |\phi_j(r,t)|^2 \tag{2.30}$$

$$i\frac{\delta}{\delta t}\phi_j(r,t) = \left[-\frac{\nabla^2}{2} + v_s(r,t)\right]\phi_j(r,t) \tag{2.31}$$

where the time-dependent effective potential v_s is expressed as followed:

$$v_s(\rho,\Psi_0,\Phi_0) = v(r,t) + v_H(r,t) + v_{xc}(\rho,\Psi_0,\Phi_0)(r,t) \tag{2.32}$$

$$\begin{aligned} v(r,t) &= v_0(r) + \theta(t-t_0)v_1(r,t) \\ v_H(r,t) &= \int \frac{\rho(r',t)}{|r-r'|}\, d^3r' \end{aligned}$$

Regarding the time-dependent v_{xc} term, it is more difficult to describe here since it relies on the time-dependent density $\rho(r,t)$ and the initial states Ψ_0 and Φ_0. Since the Hohenberg-Kohn theorem allows us to eliminate the dependence of Ψ_0 and Φ_0 because they are functional of the density in the ground state which is most of the time the starting point, it partially simplifies the determination of v_{xc}. However, the exchange correlation potential at a certain space-time position depends on densities at all other space points and previous times. It is called a non-local properties.

To get rid of this "memory" feature, one uses the adiabatic approximation in which the exchange correlation potential is evaluated at the instantaneous time-dependent density. Since the system is varying slower ans slower in time, it gets then exact because this limit reaches the stationary ground state. Since it works in many cases, the majority of time-dependent Kohn-Sham calculations use this approximation, either with the LDA or GGA functionals, see eq.2.34.

$$\begin{aligned} v_{xc}^{ALDA} &= v_{xc}^{LDA}(\rho(r,t)) \\ v_{xc}^{AGGA} &= v_{xc}^{GGA}(\rho(r,t)) \end{aligned} \tag{2.33}$$

Here now comes the linear response theory which is used for system subjected to a small perturbation, which represents many cases. It helps us to reduce the response to the first order. Here is a brief explanation of this theory.

Consider a quantum mechanical observable $\hat{\alpha}$, its expected ground state value is

$\alpha_0 = \langle \Psi_0 | \hat{\alpha} | \Psi_0 \rangle$ where Ψ_0 is the ground state wave-function associated to the hamiltonian $\hat{H}_0$. We now consider that the system is influenced by a time-dependent perturbation associated to a new hamiltonian:

$$\hat{H}_1 = F(t)\hat{\beta}, \quad t \geq t_0 \tag{2.34}$$

Where $F(t)$ is an external field associated to an observable β. This perturbation affects the system and the observable α by consequence that becomes time-dependent:

$$\alpha(t) = \langle \Psi_t | \hat{\alpha} | \Psi_t \rangle, \quad t \geq t_0 \tag{2.35}$$

The response of $\hat{\alpha}$ to this time-dependent perturbation corresponds to $\hat{\alpha}(t) - \hat{\alpha}_0$ and can be expanded in a power development of the external field $F(t)$, see eq.2.36.

$$\hat{\alpha}(t) - \hat{\alpha}_0 = \alpha_1(t) + \alpha_2(t) + \alpha_3(t) + \dots \tag{2.36}$$

where $\alpha_1(t)$ is the linear part of the response, $\alpha_2(t)$ the quadratic part, $\alpha_3(t)$ is the cubic part,.... The expression of the linear response is given as follows:

$$\alpha_1(t) = \int_{-\infty}^{\infty} \chi_{\alpha\beta}(t - t')F(t')dt' \tag{2.37}$$

where $\chi_{\alpha\beta}$ is the system response function that depends only the system properties in absence of the perturbation. Applying the theory to a system of interacting particles on which a perturbation is activated at $t = 0$ let us describe the density as in eq.2.38. Then applying the linear response theory makes us focus only on $\rho_1(r,t)$ that is described with its response function and its perturbed external field, see eq.2.39.

$$\rho(r,t) = \rho_0(r) + \rho_1(r,t) + \rho_2(r,t) + \dots \tag{2.38}$$

$$\rho_1(r,t) = \int_{-\infty}^{+\infty} dt' \int \chi(r,r',t-t')v_1(r',t')d^3r' \tag{2.39}$$

By a Fourier transformation into the frequency domain, one can express the linear response in Kohn-Sham theory $\chi(r,r',\omega)$ as in eq.2.40. f_j and f_k are the occupation numbers of the orbitals in the Kohn-Sham ground state

$$\begin{aligned} \chi(r,r',\omega) &= \sum_{j,k=1}^{\infty} (f_k - f_j) \frac{\phi_j(r)\phi_k^*(r)\phi_j^*(r')\phi_k(r')}{\omega - \omega_{jk} + i\eta} \\ \omega_{jk} &= \omega_j - \omega_k \end{aligned} \tag{2.40}$$

The equation 2.40 shows spikes at the excitation energies of the Kohn-Sham system when ω gets close to ω_{jk}. η is a damping factor and the numerator exhibits orbitals involved in the transition[118–120].

The TD-DFT gives access to transition energies and orbitals associated to an electronic transition upon absorption of a photon. This type of calculation describes a vertical transition to which is artificially applied a broadening factor to mimic the real spectra shape.

2.2 Experimentations

This section will focus on the experimentations carried out to make comparison with simulations such as light absorption and emission. I will also dwell with other properties that have a strong impact on OPV performances but are somewhat difficult to model like thin film morphology, charge carrier transport and light conversion efficiency.

2.2.1 Device construction

Layer deposition

There are two main deposition techniques for OPV devices: thermal evaporation and spin-coating. The first possibility consists in heating a crucible of a solid materials under high vacuum (around 10^{-6} mbar) to sublimate it on the substrate. The vapour will spontaneously condensate at the substrate surface because of its cold temperature. One can control the crucible temperature to manage the deposition rate and control the thickness at the ångström scale.

The spin-coating is a wet deposition method because it uses concentrated solutions. The layer formation results from the solvent evaporation by spinning the substrate at high speed.

Material choice

The active layer will be treated in the results section so that I will only talk here about interlayer and electrode material choice. Interlayers are used to impose the charge collection direction and are carefully chosen for they frontier orbital energy levels/work function but also for their relatively low electrical conductivity which is helpfull to avoid recombinations. Such compounds are also used depending on the OPV architecture, direct or inverted. Indeed, depending on the layer deposition order, deposition techniques may change and one would prefer to spin-coat solutions or thermally evaporate powders. SnO_2 or ZnO will be used as ETL while MoO_3 will be adopted for the HTL.

Electrodes are useful to collect extracted charges from the interlayer as they have a larger conductivity. We will used ITO glasses bought directly from Ossila company and Al or Ag will be thermally evaporated as counter electrode.

OPV device recipe

The first step consists in cleaning the substrate to avoid the presence of impurities. ITO substrates will successively be plunged in an aqueous solution of detergent, acetone and isopropanol for 10 minutes. These solutions are settled in a sonic bath to clean effectively the substrates. Afterwards, surface treatment is performed using an oxygen plasma for 3 minutes to raise the wettability.

The ETL deposition is done by spin-coating ZnO or SnO_2 nanoparticle solution at 3000 rpm during 30 seconds and then annealed at 150°C for 15 minutes to obtain fused nanoparticles, reduced roughness and decreased solubility in solvents. The active layer is spin-coated at 2000 rpm on top using solution of donor and acceptor in a 1:1 ratio in chlorobenzene at a total concentration of 20 mg/ml to reach a thickness of about 100 nm. The active layer is annealed at 100°C afterwards to let molecules and chains rearrange themselves after solvent evaporation and obtain a better crystallinity which will enhance OPV performances.

The next step consists in the HTL deposition, done in a thermal evaporator at 10^{-6} mbar. The desired thickness is about 8 to 10 nm for both interlayers to get a transparent layer with ideal conductivity. Finally, the counter electrode is also evaporated from pellets. One would like to reach 100 nm to have a non transparent layer with high conductivity, see Fig.2.1[121,122].

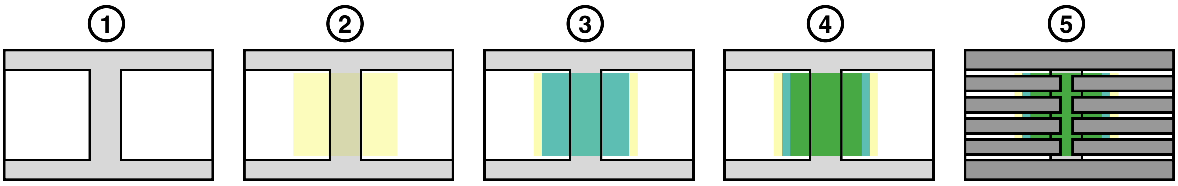

FIGURE 2.1: Representation of device making steps. 1: ITO glass substrate, 2: ETL layer deposition, 3: active layer deposition, 4: HTL layer deposition and 5: counter electrode deposition

Devices for impedance measurements

A specific device structure is required for impedance measurement that will be treated in section 2.2.4. The device structure has to be modified to create an insulator barrier between both electrodes. To do so, Al_2O_3 will be used in place of the ETL layer and is deposited by the Atomic Layer Deposition (ALD) method. This consists in successively vaporising $Al(CH_3)_3$ precursor and water, see eq.2.2.1. The chemical reaction is extremely exothermic and has to be performed under nitrogen atmosphere. This step is done at 300°C under low pressure atmosphere to deposit a 50 nm thickness layer. To reduce series resistances, one deposits a thin bus of aluminium on top of ITO of about 100 nm in thickness. This helps to obtain a better capacitance signal during the measurement.

$$2\,Al(CH_3)_3 + 3\,H_2O \longrightarrow Al_2O_3 + 6\,CH_4$$

To analyse separately hole and electron mobility, both ETL and HTL can be deposited on top of the active layer. Since only evaporation techniques can be used to avoid the redissolution of the active layer, MoO_3 can still be used for hole transport and C_{60} will replace the ZnO nanoparticles in such devices.

2.2.2 Optical spectroscopy

Since our materials have to absorb light to produce electricity, their absorption characteristics are important parameters. We have used an UV-vis spectrophotometer to measure absorbance in solution and in film. The first approach consists in comparing absorption signals between molecules to characterise their ability to form exciton. Moreover, it is also interesting to superimpose their absorption signature with respect to the solar emission spectrum because the available amount of photons coming from the sun is not similar at every wavelength.

The working principle lying behind is quite simple. A lamp is irradiating at every wavelength between 300 and 800 nm. A monochromator breaks the polychromatic character of the lamp to be able to select precisely a wavelength with a precision of 1 nm. The light is then forwarded to the sample that will absorb a certain quantity; the non absorbed intensity (I) is transferred to the detector and compared to the intensity of the emitted light (I_0), see eq.2.41. The Beer-Lambert law converts light transmission into light absorbance, see eq.2.42. This law is often used to correlate sample concentration and absorption maximum intensity; in our case, the focus is more on the signal shape, intensity and position.

$$T = \frac{I}{I_0} \tag{2.41}$$

$$A = -log\frac{I}{I_0} \tag{2.42}$$

Experimentations were carried out for ITIC, ITIC-Cl, ITIC-F, Y5, Y6 and PM7 at a concentration of $10^{-6} mol.L^{-1}$ using chlorobenzene as solvent. Blends were prepared in a 1:1 ratio between the PM7 donor polymer and all acceptors. For solid phase samples, higher concentrations must be used to reach around 100 nm thickness. The depositions are made with a spin-coater settling appropriate rotation speed, acceleration and time as a function of the solvent and the solution concentration.

Since these materials are sensible to oxygen, most of the following experimentations are done under inert atmosphere, inside a glovebox filled with nitrogen.

UV vis spectroscopy will also be used to compare signal shapes between solution and solid phase. This will highlight the impact of molecular stacking properties on the light absorption capabilities. Indeed, the solution phase is often considered as a well dispersed medium because spectroscopic measurements require highly diluted compounds. This renders a signal characteristic of isolated molecules while the solid phase is composed of densely packed molecules. Electrostatic and electronic polarization effects will affect the spectra as well as aggregation effects implying a delocalisation of the exciton over several molecules.

Finally, this instrument has also been exploited for stability measurements. The organic compounds under study can show relatively high or low resistance to long light exposure. To shed light into this issue, their signatures will be tracked over

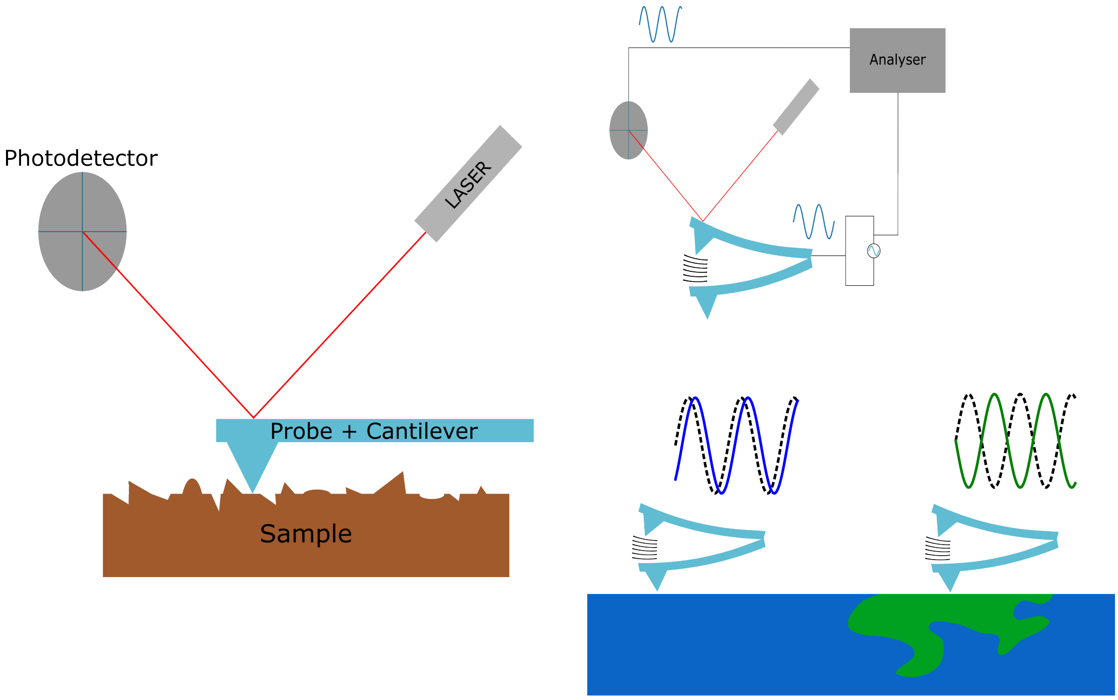

FIGURE 2.2: Illustration of the AFM analysis methods. On the left, the basic working principle and on the right, phase measurement working principle and its derived compounds localisation application.

time to analyse peak shape changing and make comparison with simulated structures in parallel to assign some intermediate compounds and understand the degradation pathways. Here, experiments will be done under inert and oxidizing atmosphere.

2.2.3 Atomic force microscopy

In parallel, morphology and roughness of thin films was studied by atomic force microscopy (AFM)[123]. This analysis consists in probing the sample surface with a really tiny tip to probe locally the chemical interactions between the surface and the tip. The tip has a bending radius of about 7 to 10 nm and analyses were performed in tapping mode.

The tip is mounted on a cantilever oscillating at 300 kHz. The measurement consists in probing, in every single point of the scanned region, the variation of the cantilever amplitude when approaching the surface. Practically, the sample is mounted on a scanner that has the ability to move horizontally and vertically. Vibrational amplitude value is fixed before the measurement. The scanner will therefore maintain a constant force between the probe and the sample by making vertical displacements to compensate the amplitude variations related to the surface roughness. This vertical displacement is translated in a topological signal. This mode is often used for organic compounds that are more fragile because it reduces the contact with the sample.

To ensure a retroactive loop, i.e. the force control is maintained between the tip and the sample surface, a laser is deflected on the cantilever to a photodetector target. When the tip gets in touch with the surface, the probe oscillation amplitude is locally modified which changes in turn the laser position on the target; finally, the retroactive loop corrects the scanner position to adjust the laser position, see Fig2.2.

Many information can be obtained from such a measurement. As firstly mentioned, the topology of the sample which can be used to access sample roughness value. Moreover, phase delay between inducted oscillation on the cantilever and the signal measured through the laser deflection can be used to localise individual components from a blend or a multi phase sample for instance, see fig. 2.2. Depending on the compound mechanical response, the phase delay vary giving information on its spatial position during the measurement.

AFM was also used for thickness calibration since it is quite easy to make the deposit on a glass substrate and to scratch the deposit with a razor blade to create a step. The height difference is then measured with the AFM tip and corresponds to the deposit thickness.

2.2.4 Impedance spectroscopy

This part of the work will deal with charge mobility inside the semiconductors. We will perform an impedance-based measurement that connects capacitance data with a simple electric model. Before explaining the model in details, let us start with some basics in electricity[124].

For a direct current, Ohm's law defines a relationship between three main electric variables, potential (V), current (I) and resistance (Ω) : $V = R \times I$ or $I = \frac{V}{R}$. The current depends on the potential bias value but is reduced as a function of the material ability to conduct charges. For alternative currents, the bias and current direction change after a certain time lapse. This results in taking into account the frequency for I and V, see eq.2.43.

$$\begin{aligned} v(t) &= V_m\, sin(\omega t) \\ i(t) &= I_m\, sin(\omega t + \theta) \end{aligned} \tag{2.43}$$

Where $\omega = 2\pi\nu$, ν is the frequency and θ is the phase difference between $v(t)$ and $i(t)$. Since the relationship between electrical response and material properties is very complex in the time domain, one uses Fourier transform to perform analysis in the frequency domain, see eq.2.44.

$$\begin{aligned} i(j\omega) &= C\, \omega\, j\, v(j\omega) \\ i(j\omega) &= \frac{v(j\omega)}{L\, \omega\, j} \end{aligned} \tag{2.44}$$

Where $j \equiv i \equiv \sqrt{-1}$. One can find an Ohm's law like expression in the frequency domain, see eq.2.45. Potential and current are respectively expressed like $v(j\omega) =$

$V_m \ \pi \ e^{j\theta}$ and $i(j\omega) = I_m \ \pi \ e^{j\theta}$.

$$v(j\omega) = Z(j\omega)\ i(j\omega) \tag{2.45}$$

$$Z(j\omega) = \frac{1}{C\omega j} \text{ and } Z(j\omega) = L\omega j \tag{2.46}$$

where $Z(j\omega)$ is the impedance and is the relative pendant of resistance for direct current, L and C stands for capacitance and inductance contribution of the impedance. The difference lies in the time dependence. Z has a real and imaginary part in the complex plane; $Z = a + jb$ where $a = Z'$ and $b = Z''$ stand for real and imaginary components and $j \equiv e^{\frac{j\pi}{2}}$ resulting in an anticlockwise rotation by $\pi/2$ in the complex plane, see Fig.2.3.

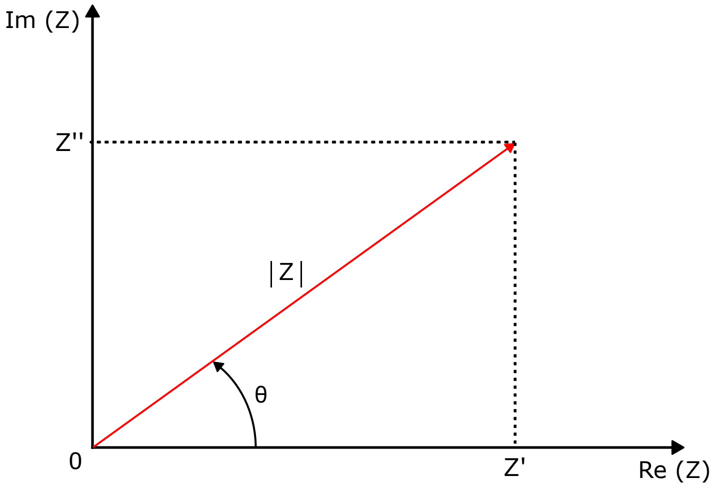

FIGURE 2.3: Impedance vector representation in the complex plane.

Z' and Z'' are also called resistance and reactance and noted R and X respectively. One can also consider the reverse impedance, $Y = Z^{-1}$ which has also a real and an imaginary part, the conductance and the susceptance: $Y(j\omega) = G(j\omega) + jB(j\omega)$. Dividing both real and imaginary components of the susceptance by omega let us find the capacity $(C(\omega))$ and the loss factor $(L(\omega))$. Both variables will be tracked upon the variation of ω, i.e. the frequency of the AC perturbation applied on the device.

The test device is referred to MIS for Metal-Insulator-Semiconductor. This architecture let us control the charge polarity inside the device and accumulates charges in the semiconductor layer. Moreover this also allows for the use of simple electric models, see Fig.2.4. the material layers are described in the section 2.2.1.

Let's now explain the experiment. One will apply a DC bias between the device electrodes from -5V to +5V to accumulate holes or electrons in the active layer. Then a small AC perturbation of about 10 mV is applied to make the charges moving into the layer. Using a relatively small perturbation compared to the DC bias let us keep Ohm's law as basic formula and the linearity conditions.

At small frequencies, charge carriers move freely in the layer but at too high AC frequency, the charges will be "frozen" in the layer due to the semiconductor nanostructure and limited conductivity.

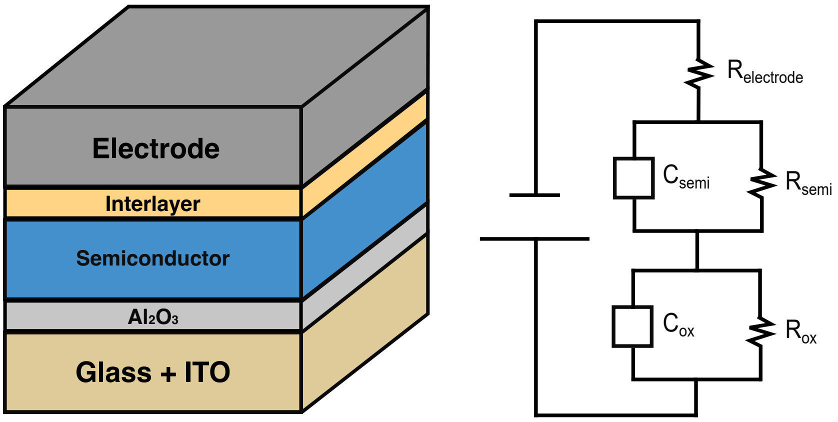

FIGURE 2.4: On the left, device architecture for charge carrier mobility measurements. On the right, the electric model for impedance spectroscopy analysis.

What stands for "small and high frequencies"? The range of operational frequencies needs to be determined and it is done by measuring the capacity of the insulator layer over a frequency domain according to the previous electric circuit model. For a metal-insulator system, this circuit is similar to the figure 2.4 without the *semi* components. We have determined the frequency range of operation between 1Hz and 10^6Hz before getting limited by series resistance from the electrode.

Since charge can move freely in the semiconductor at low AC frequency, the measured capacity corresponds to the signal of an insulator while at high frequency, the semiconductor acts like an insulator due to "frozen" charge carriers and the capacity arises from both the insulator plus the semiconductor layer. This will influence capacity value because it is inversely proportional to the thickness, see Eq: 2.47.

$$C = \epsilon_0 \epsilon_r \frac{Area}{Thickness} \tag{2.47}$$

We will measure the frequency at which the changing regime appears and combine it with Einstein law for hole diffusion, see eq.2.48 to extract charge carrier mobility values in a vertical geometry and using similar layers and same thicknesses as used in OPV devices, see eq.2.49.

$$\frac{D_p}{\mu} = \frac{kT}{q} \text{ and } D_p = \frac{l^2}{\tau} \tag{2.48}$$

$$\mu = \frac{q}{kT} l^2 f \tag{2.49}$$

With D_P the charge carrier diffusion coefficient, μ the charge carrier mobility value, l the layer thickness, kT the Boltzmann temperature coefficient, q the unitary charge and τ/f the characteristic time/frequency.

2.2.5 I-V measurements

When it comes to OPV performances, one needs to plot voltage vs current data. We have always acquired data with and without light exposure to compare the device behaviour between the depleted and accumulated regime. All details related to physics background are mentioned in the section 1.3.7.

Sunlight was simulated through a LED sunlight simulator model *LSH-3720* from Newport with an AM 1.5 calibration. This is related to a sun light tilt versus equator and takes into account the atmosphere absorption. A DC power supply was then connected to device electrodes to measure the current between a range from -1.5 to 1.5 V.

A mask with well delimited square holes was settled between the device and the lamp to keep the same irradiation area and compare current density data between samples.

Chapter 3

Optoelectronic properties: calculations and experiments

3.1 Introduction

This section focuses first on the famous NFA used in OPV technology. ITIC and Y5, shown in Fig.3.1, have both unlocked higher efficiencies in OPV devices. In this part, results will cover simulations about optical and electronic characteristics, as well as optical spectroscopy experiments for comparison with DFT calculations. We will also touch on the chemical stability of these compounds.

First, DFT results will help us to describe electronic assets of NFAs and let us analyse their structures and the modifications in the shape and energy of molecular orbitals upon structural changes, such as halogenation. The theoretical optical signatures in UV-vis spectra will be unfolded into their constitutive electronic transitions. The most relevant features will be then analysed by creating Natural Transition Orbitals (NTO). This is a summing technique of molecular orbitals involved in the selected electronic transition that helps to visualise hole and electron localisation after photon absorption.

Optical spectra will be experimentally recorded to compare to corresponding theoretical results and to analyse phenomena non reproducible in DFT. In particular, the impact of halogenation will be tracked in solution and thin-film samples to analyse benefits from chemical modifications from an electronical and morphological aspect.

Optical absorption experiments were also settled to track the NFA degradation behaviour. NFA are known to be unstable in ambient conditions due to sensitivity to air and moisture but also to intense light exposure. Experiments were then performed to track light absorption signature changes in inert (N_2 filled glovebox) atmosphere and in ambient air.

UV-vis spectra are recorded after a fixed time step and mass spectrometry analysis will be performed in parallel to connect optical behaviour and potential mass correlated change during the irradiation process under a calibrated lamp. Moreover, DFT calculation will be used as a complement to confirm experimental data and propose chemical structure as intermediate or final compounds in the degradation mechanism.

Finally, other D-A systems will be only theoretically analysed to illustrate other potential structural change and the resulting electronic properties, as well as the effect of adding successive D and A units in a block co-polymer geometry.

All DFT calculations rely on the LC-ωHPBE/6-31G** functional. By tuning the ω parameter, the following values were obtained for the ITIC systems: 0.099 Bohr^{-1} for ITIC and ITIC-F and 0.096 Bohr^{-1} for ITIC-Cl. Values obtained for BTP systems are 0.106 Bohr^{-1} for BTP and BTP-4F and 0.102 Bohr^{-1} for BTP-4Cl.

3.2 Non-fullerene acceptors

3.2.1 Geometry

Both ITIC and Y5 are shown in fig.3.1. We can see that π electrons are fully delocalised ITIC is rather linear while Y5 adopts a crescent shape, or a banana shape. Regarding the substituents, ITIC has two side chains fixed on the same carbon and out of the plane due to steric hindrance between the backbone the phenyl group while Y5 has only one side-chain on each carbon or nitrogen without rigid cycles. Moreover, ITIC shows a higher degree of planarity while Y5 displays a small twist. This comes from the inner side chains located on the quasi neighbouring nitrogens. This is evidenced from DFT calculation showing the constraint vanishing when replacing the actual ethyl groups by hydrogens; the initial 8.5° of twist then disappear.

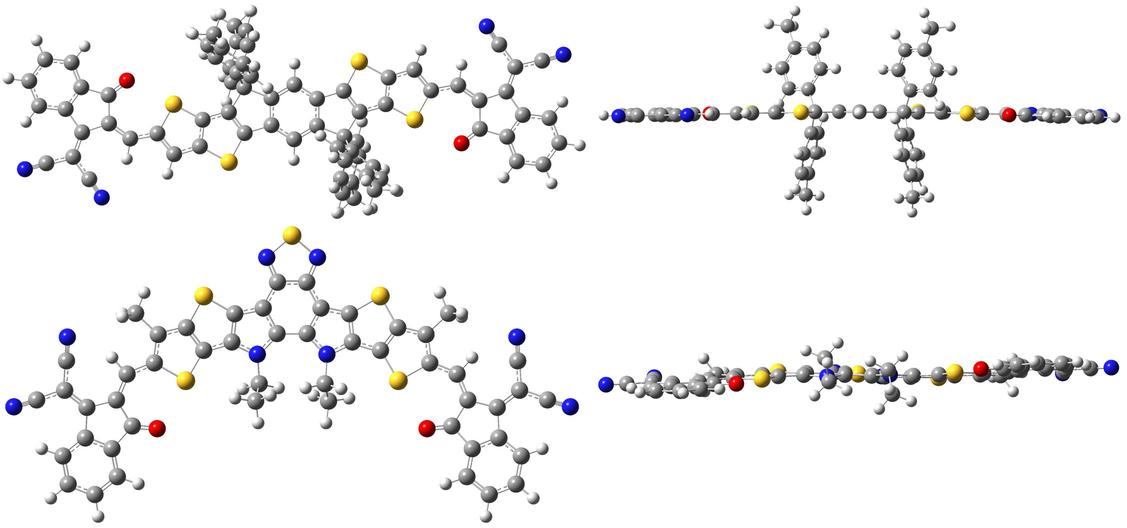

FIGURE 3.1: (Left) Top view and (right) side view of BTP and ITIC molecules represented with the GaussView software. carbons and hydrogens are represented by greys and white balls while nitrogen, oxygen and sulphur atoms are respectively drawn in blue, red and yellow.

Other studied compounds at the theoretical level are shown in fig.A.1, with two end cap hydrogen substituted by fluorine and chlorine atoms for Y6/ITIC-F and Y7 ITIC-Cl respectively. As expected, substituting hydrogens by halogens on the extremities does not affect much the overall geometry. Only ITIC-F and Y6 will be compared to experiments due to compound availability from suppliers.

3.2.2 Orbitals: energy level and localisation

With the proper omega tuning, we can now probe the LUMO and HOMO relative energies, plus localise them on the molecule. This will allow us to compare substitution effects on the electronic structure and the role of push-pull effect. Calculations have been carried out in chloroform since most experimental results are performed in a similar solvent. To achieve this, intrinsic parameters from the functional are tuned to take into account the dielectric constant of the medium, which is $\epsilon = 4.7113$

On the fig.3.2, the first graphic represents the energy of the frontier orbitals for both NFA systems with their halogenated derivatives. HOMO energy values for ITIC NFAs are calculated to be -5.58 eV, -5.71 eV and -5.76 eV for ITIC, ITIC-F and ITIC-Cl respectively while their LUMO are estimated at -3.26 eV, -3.40 and -3.48 respectively. For the Y family molecules, HOMO are estimated at -5.56 eV, -5.67 eV and -5.73 eV for Y5, Y6 and Y7 respectively while LUMO are estimated at -3.30 eV, -3.43 eV and -3.53 eV respectively.

First and straight observation is the orbital stabilisation upon adding electro-attractive substituents. In fact, F and Cl atoms have a strong inductive effect to attract electrons due to their high electronegativity. The HOMO and LUMO energy are symmetrically reduced by 0.12 eV and 0.14 eV respectively when comparing ITIC and ITIC-F. A comparison between ITIC-F and ITIC-Cl shows a lower energy diminution for HOMOs than LUMOs, by 0.05 eV and 0.09 eV respectively. Similar observations can be extracted for BTP and derivatives. These observations are consistent with the electro-attractor character of halogens and the polarisation of the $\mathrm{C-X}$ bound, where X stands for F or Cl.

These values should be carefully handled because they refer to a single molec-ule in a dielectric continuum using Koopman's approximation and have reasons to be close to experimental data (obtained through cyclic voltammetry (CV) or ultra-violet photoelectron spectroscopy). Nevertheless, they are very useful to compare systems between them. Indeed, let us consider the CV experimental results for BTP molecules conducted in acetonitrile solution with Bu_4PF_6 0.1 M[125–127] . Values of -5.55 eV and -3.87 eV were obtained for HOMO and LUMO of Y5 respectively, -5.68 eV and -4.00 eV respectively for Y6, and -5.64 eV and -4.15 eV respectively for Y7. Absolute values differ from what has been calculated in DFT but the energy tendency is well confirmed.

If the halogen substitution has only an inductive effect, we expect to see only a symmetrical effect on orbital energies and the electronical gap will remain constant. The DFT results confirm this trend with gap values of ≈2.30 eV for ITIC family and ≈2.2

Compounds	HOMO		LUMO		Electronic gap
	Acceptor	Donor	Acceptor	Donor	
ITIC	20%	80%	68%	32%	2.32
ITIC-F	20%	80%	69%	31%	2.31
ITIC-Cl	20%	80%	70%	30%	2.30
Y5	22%	78%	68%	32%	2.26
Y6	22%	78%	68%	32%	2.24
Y7	22%	78%	70%	30%	2.20

TABLE 3.1: Contribution of the LCAO coefficients in the frontier orbitals on each moiety for all NFA molecules.

eV for Y family. Detailed values are stored in table 3.1 At first sight, these results are not favourable for OPV because the LUMO energy reduction upon halogenation will also reduce the energy difference with the HOMO of the donor compound involved for the exciton splitting. This should be responsible of a V_{OC} loss compared to non halogenated NFA.

About orbital localisation, HOMOs are delocalised on the donor moiety while LUMOs are delocalised over the whole molecule, as seen in the fig. 3.2. LCAO coefficients have been calculated for each atom and their square values have been summed over each acceptor (A) and the donor (D) moiety. The results for the LUMO are well balanced for all ITIC systems with 34% for both A parts and 31% on the D part. For the HOMO, the D part has a value of 80% and both A parts reach a value of 10%. Similar trends are obtained for chlorine and fluorine derivatives, as resumed in table. Once again, no major impact arises from halogen atoms, pointing to only inductive effects at local scale.

In the case of BTP systems, the HOMO and LUMO are distributed similarly, with 78% - 22% for the parts and D part in the HOMO respectively, and 30% - 70% for A parts and D part in the LUMO respectively. Results for both ITICs and Ys systems are listed in table 3.1. These results on orbital localisation are interesting concerning photon absorption. Indeed, in the lowest absorption band, an electron is typically promoted from the HOMO into the LUMO if the transition is allowed.

If these orbitals are not located on the same molecular region, there is a high tendency of the formed exciton to have a charge transfer character which is a strong advantage in the OPV field. In fact, this implies that the electron and the hole are far from each others and then, the Coulombian interaction is reduced and makes it easier to split the charges. Nevertheless, a too high delocalisation decreases the transition probability thus a compromise is require to maximise the exciton generation and the splitting efficiency.

Moreover, a Mulliken charge distribution has been carried out on neutral molecules to assess the presence of an eventual dipole. ITIC systems do not have any dipolar

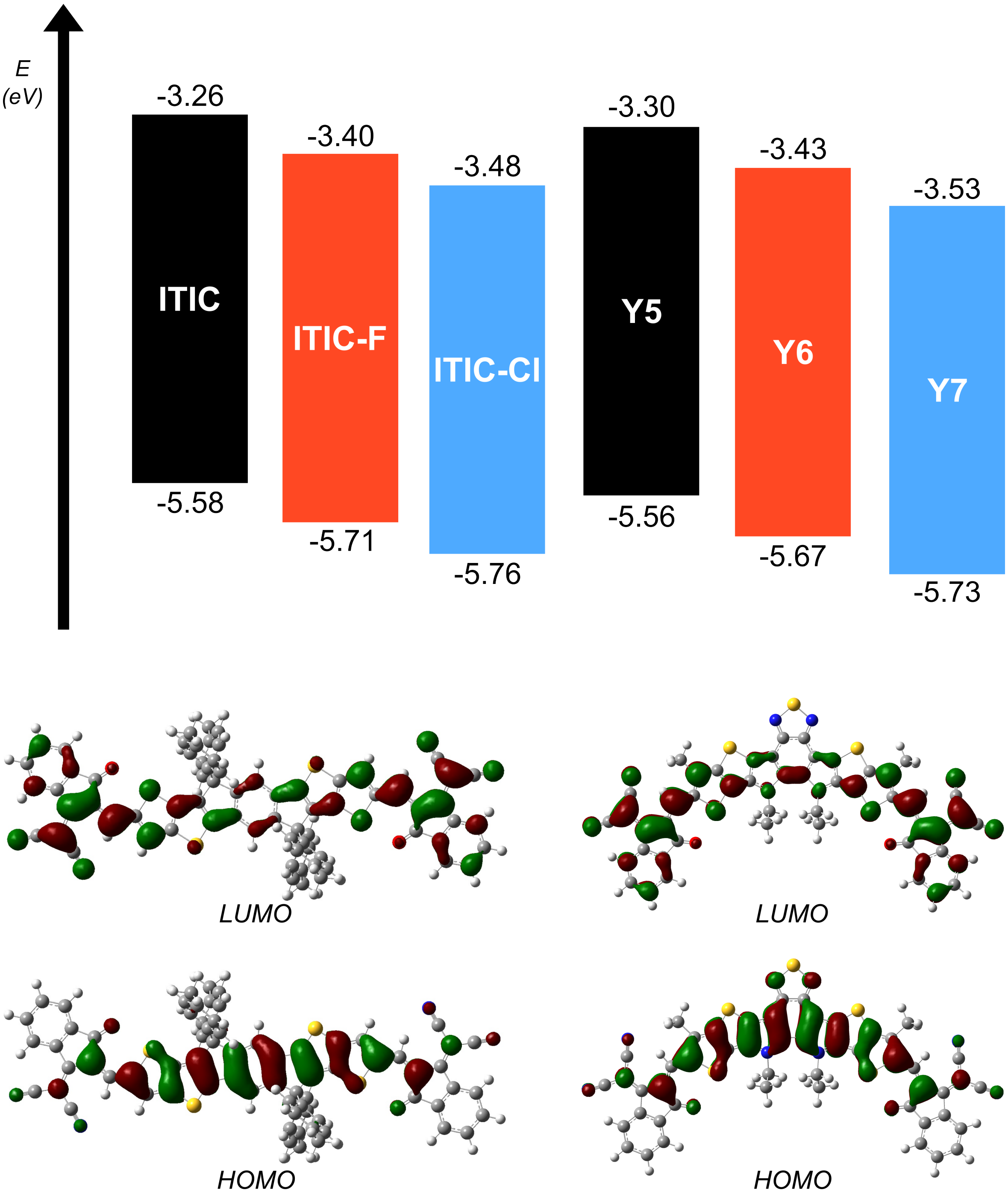

FIGURE 3.2: First chart represents electronic gap for each NFA with their HOMO and LUMO energy values represented below and above each rectangle respectively. Second image represents HOMO and LUMO localisation on ITIC, on the left, and Y5 NFA, on the right.

moment due to their planarity and the presence of an inversion centre which is not present on the BTP derivatives. This leads to the presence of a permanent dipole moment in all Y systems : -7.08 D, -1.70 D and -0.56D for Y5; Y6 and Y7 respectively. The Y5 dipole is surprisingly high compared to halogenated derivatives and is expected to generate a significant energetic disorder in non-crystalline materials. Nevertheless, these dipoles also act as an exciton separator driving force by increasing charge transfer state character of the molecules.

3.2.3 TD-DFT simulations

In this section, we have pushed the theoretical work to the analysis of NFA optical signatures and have highlighted important factors correlated to the electronic structure to provide a good understanding of light absorption phenomena.

TD-DFT calculations have been performed accordingly and results are shown in fig. 3.3. TD-DFT gives informations about any transition from the fundamental state of the molecule to n electronical excited states, with n wisely chosen to describe the molecule absorption region in the low energy range. Each optical transition contains several information, such as the energy required to reached this state (expressed in eV), the oscillator strength that translates the probability of the transition to occur and the involved one-electron excitations with a coefficient representing their weight in the solid state.

The spectra are obtained by computing 70 excited states and applying an artificial broadening of 0.25 eV around each transition. TD-DFT spectra only show vertical transitions, from a fundamental electronic state fundamental vibrational state to any excited electronic state in the same geometry. This means that vibrational coupling (or electron-phonon coupling) is not taken into account in the spectra.

For ITIC molecules, S_0 to S_1 transitions are located at 610 nm (2.03 eV), 618 nm (2.00 eV) and 628 nm (1.97 eV) for ITIC, ITIC-F and ITIC-Cl respectively. For BTP molecules, these transitions occur at 614 nm (2.02 eV), 621 nm (2.00 eV) and 630 nm (1.97 eV) for Y5, Y6 and Y7 respectively. A direct observation shows that all curves are well superimposed, meaning that the previous observation on electronic gap not being impacted by halogenation is verified on the optical gap as well.

In the table 3.2, the most intense transitions and their characteristics are described. The most intense peak is described as the $S_0 \rightarrow S_1$ S_1 for each molecule. It involves a HOMO to LUMO transition with a probability of 98%.

There is also another non negligible transition, the $S_0 \rightarrow S_9$ for ITIC and BTP derivatives. In the case of ITIC, its always a mixing of the H-1 → L+1 transition and the H-4 (or H-5 for ITIC-Cl) → L transition. Since the more probable transitions involve the LUMO, we can conclude that other excited states are available for charge generation process upon sunlight irradiation in OPV devices.

The overlap value mentioned in table.3.2 comes from the generated NTO which takes into account all departure and arrival orbitals for each contributing transition to generate effective orbitals. The overlap parameter calculates the degree of coverage between hole versus electron localization upon excitation.

In that way, the overlapping parameter ϕ_s can show us the character of the excited state. On the one hand, if it is a localised and very stable exciton state, $\phi_s = 100\%$, the departure and arrival effective orbital strongly overlap and the CT character is null. On the other hand, $\phi_s = 0\%)$ means a total CT character but since electron excitation relies on orbital coverage through the transition dipole moment, the transition probability is expected to be null in this extreme case. The Best compromise is achieved for $\phi_s \approx 50\%$ for good absorption capability and sufficient exciton separation for efficient charge splitting.

For all molecules, the S_1 state has clearly a pronounced CT character while allowing efficient light absorption. ITIC S_9 state shows a higher degree of CT character than the Y S_9 states, which suggests that he exciton would be more likely better dissociated in ITIC systems than Y ones when pumping this band. Since the intense band is more pronounced for ITIC, the latter should generate more charge carriers than Y in the same irradiation conditions.

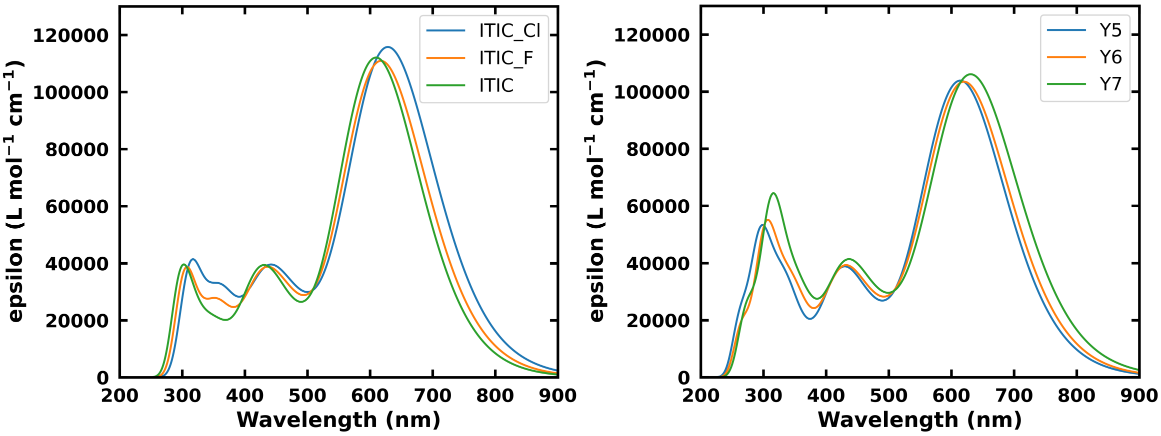

FIGURE 3.3: TD-DFT optical spectra of ITIC derivatives on the left and BTP derivatives on the right.

3.2.4 Optical experiments

Experiments have been carried out in parallel of the theoretical analysis to supply experimental data in solution to be compared to theoretical results on isolated molecules and also in thin films to understand the behaviour in condensed phase, such as in the active layer of OPV devices.

Optical absorption experiments have been carried out in chlorobenzene at 10^{-6} mol L^{-1} concentration and are shown on fig.3.4 and in solid phase by thin-film deposition from chlorobenzene solution at an average concentration of 10^{-2} mol L^{-1}. Solid lines refer to thin-film curves and dash lines to spectra in solution.

Compounds	Excited state	Energy	Oscillator strength	Major orbital contributions	Overlap
ITIC	S_1	2.05 eV	2.12	H → L: 98%	64%
	S_9	2.96 eV	0.56	H-4 → L: 60% H-1 → L+1: 30%	63%
ITIC-F	S_1	2.0 eV	2.05	H → L: 98%	62%
	S_9	2.88 eV	0.55	H-4 → L: 65% H-1 → L+1: 27%	61%
ITIC-Cl	S_1	1.97 eV	2.13	H → L: 98%	62%
	S_9	2.84 eV	0.57	H-5 → L: 58% H-1 → L+1: 34%	61%
Y5	S_1	2.01 eV	1.86	H → L: 98%	63%
	S_8	2.88 eV	0.34	H-2 → L: 85%	76%
Y6	S_1	1.99 eV	1.85	H → L: 98%	62%
	S_8	2.86 eV	0.35	H-2 → L: 85%	75%
Y7	S_1	1.95 eV	1.90	H → L: 98%	62%
	S_8	2.82 eV	0.38	H-2 → L: 85%	75%

TABLE 3.2: Description of the relevant excited states for each compounds. Each excited state is associated with its energy, oscillator strength, dominant one-electron excitation, overlap between departure and arrival orbitals in the NTO formalism.

ITIC based systems

0-0 transition maxima from solution absorption spectra are located around 670 nm (1,85 eV), 680 nm (1,82 eV) and 690 nm (1,80 eV) for ITIC, ITIC-F and ITIC-Cl respectively. The 0-1 vibronic maxima are situated at 620 nm (2.00 eV), 630 nm (1.96 eV) and 640 nm (1.94 eV) for ITIC, ITIC-F and ITIC-Cl respectively while the 0-2 transition peaks at 565 nm (2.19 eV), 575 nm (2.16 eV) and 585 nm (2.12 eV) for ITIC, ITIC-F and ITIC-Cl respectively. It is clear that the absorption region is in the red region of the visible spectrum.

There is only 20 nm (0.05 eV) difference between ITIC and ITIC-Cl lowest absorption band, with ITIC-F located in the middle range. Thus, the optical gap is quite similar for all molecules and halogenation has clearly no major effect on the optical gap. Comparison with theoretical spectra shows a red shift between 0-0 maxima of about 60 nm (0.2 eV). This is probably due to limitations in calculation using an implicit solvent and performed at 0 K.

Looking at the solid phase results gives information about possible aggregation effects. Indeed, peaks are broadened compared to solution due to aggregation effects (exciton delocalisation) or electrostatic interactions between neighbouring molecules. Fig.3.4 shows the normalised spectra for better visualisation. In reality, thin films

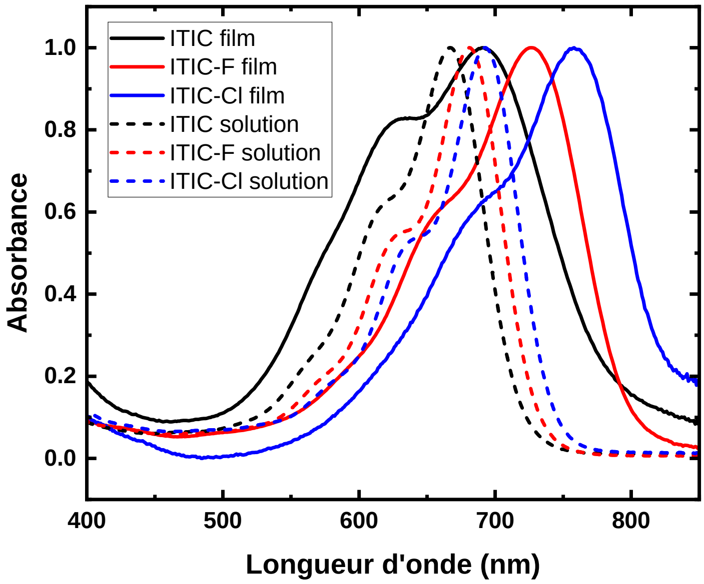

FIGURE 3.4: Absorption spectra of all ITIC derivatives in chlorobenzene solution (dashed lines) at a concentration of 10^{-6} mol L^{-1} and in thin films (solid lines).

have less intense maxima compared to solution which points to a wider distribution of molecular conformations due to steric effects in the condensed phase. Nevertheless, the first vibronic excitations are still very well defined.

Moreover, there is a red shift from solution maxima to solid phase maxima located at 690 nm (1,80 eV), 725 nm (1.71 eV) and 755 nm (1.64 eV), leading to shifts reaching 20 nm (0.05 eV), 45 nm (0.11 eV) and 65 nm (0.16 eV) for ITIC, ITIC-F and ITIC-Cl respectively. The red shift is more pronounced with chlorine and fluorine derivatives and is possibly linked to the capability to create halogen interaction with neighbours. ITIC has high structural constraints from its hexylphenyl side chains which create space around each molecule and prevent efficient π-π stacking.

Hao Zhang et al.[128] and Dan Deng et al.[129] have explained this through AFM, X-ray photoelectron spectroscopy (XPS) and x-ray diffraction experiments. There is a strengthening of non-covalent interactions $F \cdots H$ and $F \cdots S$, and also by a denser π-π stacking while substituting hydrogen terminal atoms by fluorine atoms. Moreover, most of NFA thin films are processed through halogenated solvents in which fluorinated molecule have a better miscibility and will lead to better organised films. Hanjian Lai et al.[130] have also evidenced $Cl \cdots S$ intermolecular interactions through chlorine d orbitals and sulphur lone pairs in X-ray diffraction data. A higher planarity has also been recorded despite the higher steric hindrance going from the chlorine to fluorine and hydrogen.

Note that our depositions are made by spin-coating which rather forms amorphous structured thin films. Previous observations help to understand affinity between ITIC based systems and, to a certain extent, the competition between chemical affinities and steric repulsions in the thin film organisation that could be at the origin of their respective optical response.

BTP based systems

Regarding the BTP systems, Y6 has been dissolved in the same conditions as ITIC molecules. The maximum of absorption is located at 733 nm (1.69 eV) and the vibronic peaks are situated at 675 nm (1.84 eV) and 590 nm (2.10 eV) for the 0-1 and 0-2 transitions respectively. The 0-2 transition is surprisingly well defined with a non-traditional "shoulder" shape. Compared to ITIC-F, the Y6 absorption spectrum is red-shifted by about 50 nm (0.13 eV). Since calculations have not demonstrated major changes in the electronic properties, this shift could be due to molecular interactions in solution probably triggered by the permanent dipole moments.

Looking at the solid phase spectra, peak broadening appears as for ITIC thin films resulting from aggregation and electrostatic effects leading to a wider distribution of transition energies. The Y6 molecule also shows a large red shift passing from solution to the solid-phase. The displacement is about 100 nm with a solid state maximum of absorption located at 830 nm (1.49 eV). Besides the fluorine atoms that enable more intermolecular interactions, The Y molecules have less steric hindrance because of their phenyl-free side chains. In fact, a crystalline structure has demonstrated the existence of 4 different dimers coupled by interactions over the molecular core or over the edges in contrast to the ITIC systems due to their side-chain steric hindrance.

BTP shows thus more favourable optical properties for OPV devices since the solid-state spectral region ranges from 600 to 900 nm (2.06 - 1.38 eV) approximately. This lets the choice of a donor polymer absorbing at higher energy. The absorption of Y6 also matches an important zone of the solar emission spectrum where there is a large quantity of incident and by extension absorbed photons.

Halogen comparison was not established for the Y molecules because these molecules still suffer from synthetic difficulties and Y5 and Y7 were not purchased. According to the DFT results and experiments led on ITIC based systems, plus the high likeness between Y and ITIC molecules structures, we can presume similar trends for Y5 and Y7.

3.2.5 Donor polymer

After the individual characterisation of all NFAs, a donor polymer was chosen to create an active layer in the same conditions for each acceptor. The polymer also has to blend easily with the acceptor and be miscible in the same solvents. We have chosen PBDB-T-2Cl (PM7) which has also a A-D-based chemical structure, shown in fig.3.5.

Fig 3.6 represents the absorption spectrum of the polymer, ITIC-F chosen as acceptor for the further steps of the study, and the blend of both donor and acceptor with the same total concentration of species in solution compared to the solutions of the

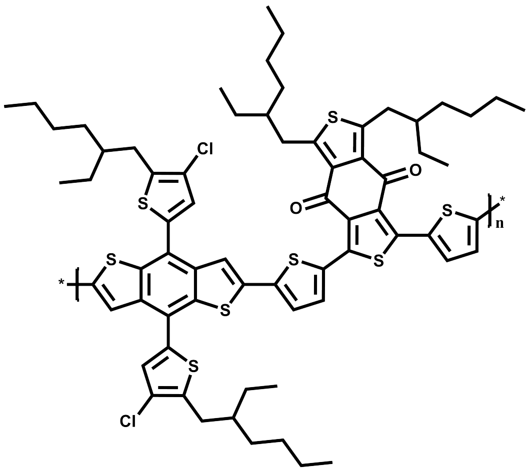

FIGURE 3.5: Lewis structure of the PM7 donor polymer

isolated compound; we have also added the numerical sum of the spectra of both isolated species to compare with the blend signal. There is also a graph including normalised spectra for both solution and solid state measurements.

PM7 has a maximum of absorbance at 605 nm (2.04 eV) and its 0-1 transition lies at 560 nm (2.21 eV). Its absorption intensity is much lower than the ITIC-F signal because of the less rigid structure and higher structural disorder; this makes typically polymer chains less planar and effectively less conjugated than small π-conjugated molecules. In fact, polymers can be seen a long repetition of chromophoric units whose size can vary as a function of the chain rigidity. The large number of conformations available tends to decrease the intensity and to broaden the peaks despite the longer theoretical conjugation length[131].

The theoretical addition of the spectra of both isolated systems covers with high fidelity the blend signal which confirms the absence of interaction phenomena that could arise from mixing. Small differences are present and certainly come from solution preparation; since these molecules are strong light absorber, tiny variations in quantity during weighting can be seen in the spectral signature. This can be seen on the ITIC maximum component of the black curve

On the second graph, solution vs solid-state spectra are compared and the red shift from the ITIC-F molecule already addressed in section 3.2.4 is recovered. In the case of PM7, no changes are observed in the solid phase, meaning that no significant intermolecular interactions or planarisation effects occur.

We can also see the overlap with the acceptor signal in solution spectra that reduce the absorption coverage region already mentioned in previous section. Because of the ITIC-F red shift in solid state, the overlap is a bit decrease but still consistent which will probably lead to lower performances because of lower light spectrum covering.

In the case of PM7:Y6 blend, the light absorption coverage is broader since the red shift occurring in the solid state is much more important. Beside, the augmented

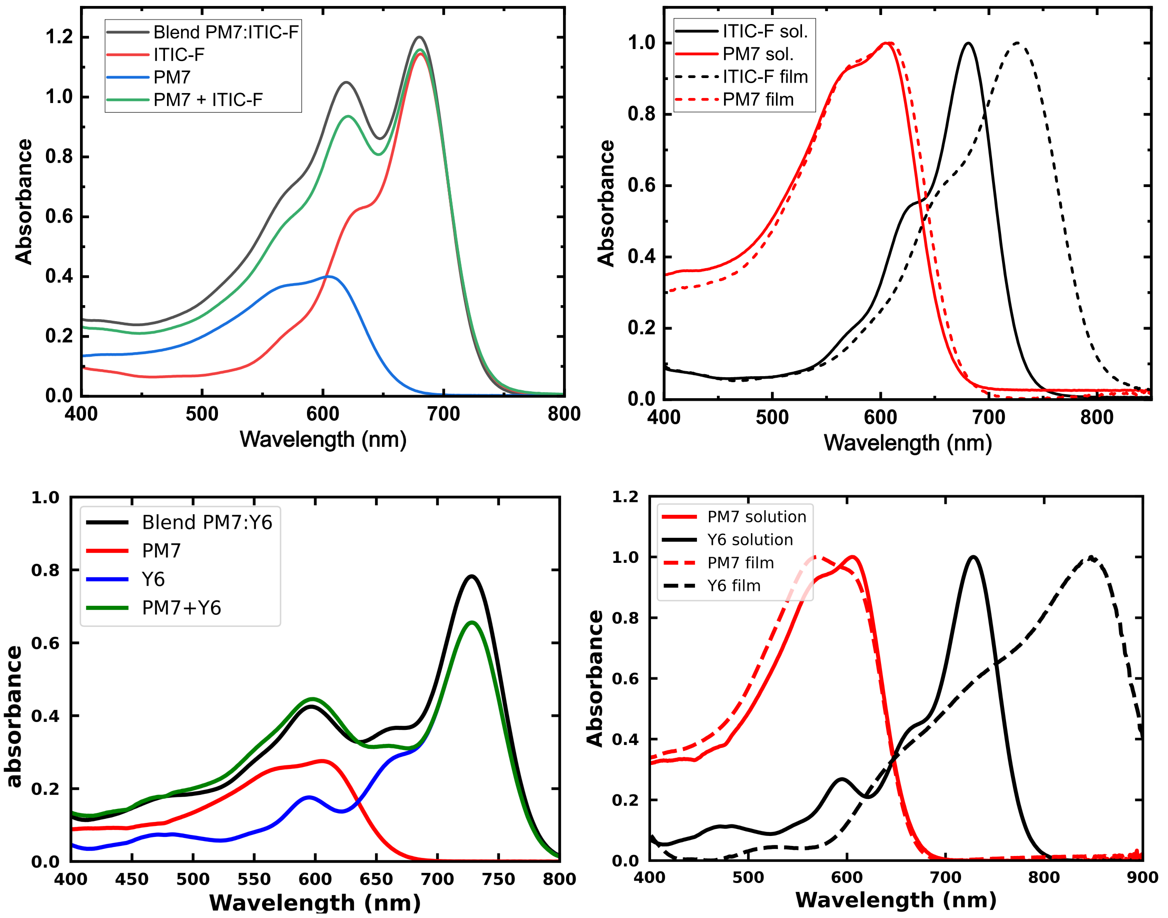

FIGURE 3.6: Absorption spectra of PM7, ITIC-F and D:A blend. On the left, non-normalised signals plus the numerical addition of the spectra of both isolated compounds in chlorobenzene at 10^{-6} mol L^{-1}. On the right, normalised signal of both solid state and solution absorption for PM7 and ITIC-F.

wavelength range is also located in a high photon density area of the solar emission spectrum. This is an important factor for OPV devices and indicates that PM7 is more suitable for blending with BTP molecules to get more efficient devices.

3.3 Push-pull effects

In this section, a purely theoretical analysis of other donor and acceptor will be presented to show more precisely how push-pull effect, CT states, absorption spectrum,...can be affected by the chemical nature of the chosen D and A blocks.

These molecular and polymeric structures have been synthesized for further development in OPV and the willingness to improve current results largely dominated by PBDB-T donor polymers and BTP acceptor molecules. The group of Prof. Sébastien

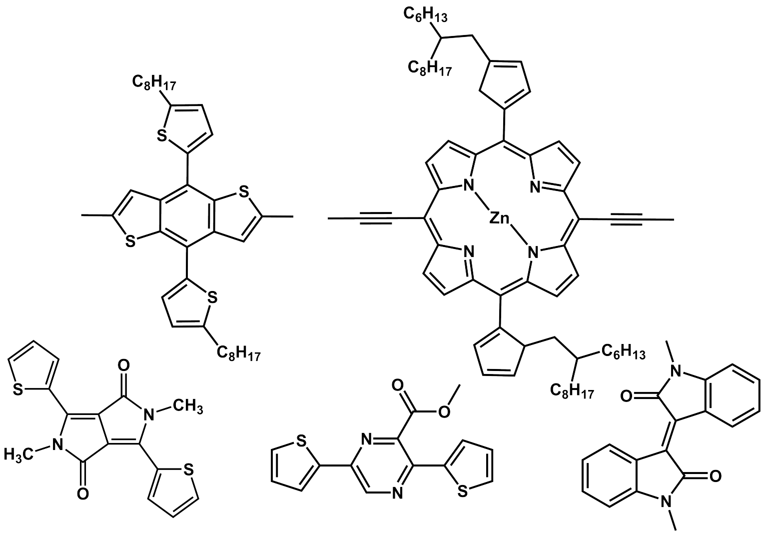

FIGURE 3.7: Lewis structure of all building blocks used for M1, M2 and P1 to P6 systems. First two molecules, from left to right, correspond to BDT and Zn-porphyrin donor groups. Last three are respectively DPP, PiP and Ind from left to right.

Clément has synthesised and combined BDT and Zn-porphyrin as D units with several A structures, such as 2-pyrazinecarbox-ylic acid, 3,6-di-2-thienyl-, methyl ester (PiP), 2,5-dimethyl-3,6-di(thiophen-2-yl)-2,5-dihydropyrrolo-[3,4-c]-pyrrole-1,4-dione (DPP) and N,N′-dimethyl isoindigo (Ind), shown in fig.3.7. Explicit structures are shown in fig.A.2

These assembled D-A systems are also linked to several perylene diimide (PDI) based molecules by long alkyl chains, resulting in a very large molecule or monomer block for further polymerisation. Clément S. et al. contacted us to obtain deeper details about the electronic properties of their molecules and polymers and to know if some of their compounds would exhibit a pronounced CT state upon light irradiation.

The studied compounds are reported in table3.3 to illustrate their chemical structure assembly. The M1 and M2 molecules are made of the porphyrin donor surrounded on each side by a DPP molecule, each carrying two PDI groups. To build the monomer in P1 to P3 polymers, the BDT donor has been linked to one DPP, PiP and Ind respectively, with each acceptor carrying respectively two, one and two PDI moieties. P4, P5 and P6 are completely similar to the previous monomers except that the donor BDT has been replaced by the Zn-porphyrin unit.

Since all π electrons from PDI groups are not interacting with those of the D-A core, they will not be represented in the next figures. All molecular structure names will refer to the D-A core moieties. Besides, all alkyl side chains are removed from simulations because of their negligible impact on the electronic and optical properties.

	M1	M2	P1	P2	P3	P4	P5	P6
Donor moeity	BDT	Porh.	BDT	BDT	BDT	Porph.	Porph.	Porph.
Acceptor moeity	2 DPP	2 DPP	1 DPP	1 Pip	1 Ind	1 DPP	1 Pip	1 Ind
PDI units	4	4	2	1	2	2	1	2

TABLE 3.3: Table reporting chemical composition of all studied compounds.

3.3.1 Molecular geometry

Globally, each BDT based compound induces a dihedral angle between D and A unit of about 20°, which is not the case for porphyrin based systems, as seen in fig.3.8. This torsion is associated to the sulphur atoms from the thiophene cycles whose radius size is large enough to create a torsion to avoid steric hindrance. In porphyrin based systems, the triple bonds located between the porphyrin and the A unit gives enough space to enable full planarity and maximise the π orbital overlap along the molecular backbone. The observations are identical with the other monomer systems.

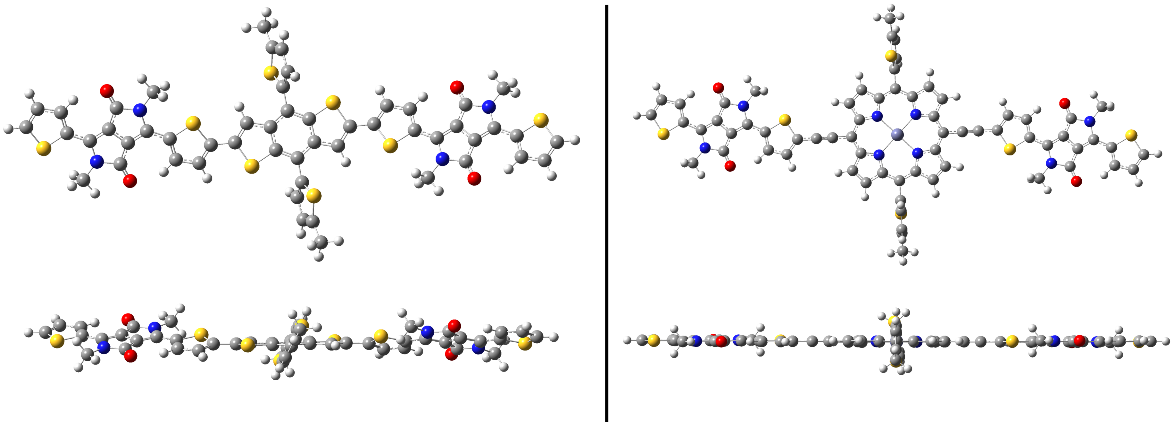

FIGURE 3.8: Top and side view of molecules M1, on the left, and M2, on the right.

3.3.2 Electronic structure

Electronic levels of energy, shown in fig.3.9 point to larger electronic gaps for all BDT substituted compounds compared to porphyrin systems. Respective values for M1, P1, P2, P3 are 2.33 eV, 2.47 eV, 3.15 eV and 2.62 eV while M2, P4, P5 and P6 reach 2.00 eV, 2.18 eV, 2.47 eV and 2.32 eV respectively. The highest values are obtained for the P2 and P5 compounds, i.e., with the PiP acceptor unit, while the DPP unit yields the narrowest electronic gap in P1 and P4. In parallel, the Ind unit provides the deepest LUMO energies but has also a deep HOMO, which results in an intermediate electronic gap size. M1 and M2 show lower HOMO and LUMO,

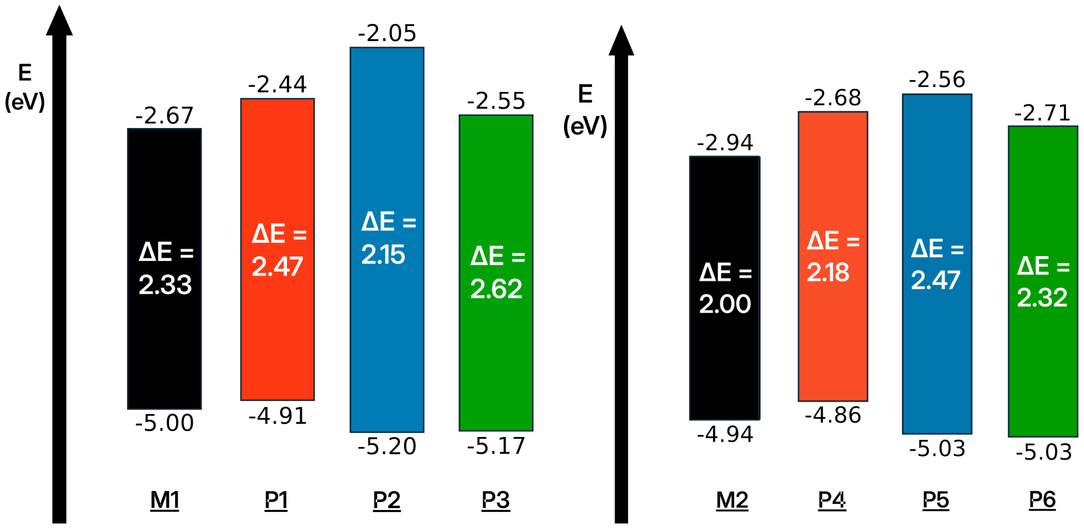

FIGURE 3.9: Orbital energy diagram of BDT based D-A compounds on the left and porphyrin based D-A compounds on the right.

	BDT	Zn-porph.	DPP	Pip	Ind
LUMO	-1.25	-2.35	-2.46	-2.03	-2.61
HOMO	-5.27	-5.05	-5.13	-5.65	-5.72

TABLE 3.4: Table summarizing energy values for frontier orbitals of each D-A system molecular brick.

as well as a reduced gap because of the extended conjugation resulting from the second acceptor unit .

BDT based systems have a broader distribution of LUMO values than porphyrin derivatives, ranging from -2.05 ev to -2.67 eV (0.62 eV range) against -2.56 to -2.94 eV (0.34 eV range). Nevertheless, porphyrin LUMOs are deeper than those of BDT by an average value of of 0.3 eV. It is interesting to note that P2 LUMO stabilisation is much higher than in other systems because compared to BDT, PiP has a deepest LUMO which is not the case compared to the porphyrin.

In terms of frontier orbital localisation, shown in fig.3.10, BDT based systems show significant changes in the LCAO pattern going from P1 to P3. In other words, in P1 the A unit governs the electronic properties and thus appears to be a better donor than the BDT unit while, in P3, BDT acts a good donor as the HOMO is mainly centred on its core and Ind acts as a good acceptor because the LUMO is mainly localised on its core. P2 acts as an intermediate case having electron density respectively centred on each unit but with more delocalisation along the whole backbone. The situation found in M1 results from the "communication" between both DPP groups and the extension of the conjugation while M2 has a fully delocalised HOMO and LUMO centred on the porphyrin meaning that the porphyrin is more acceptor than the DPP unit.

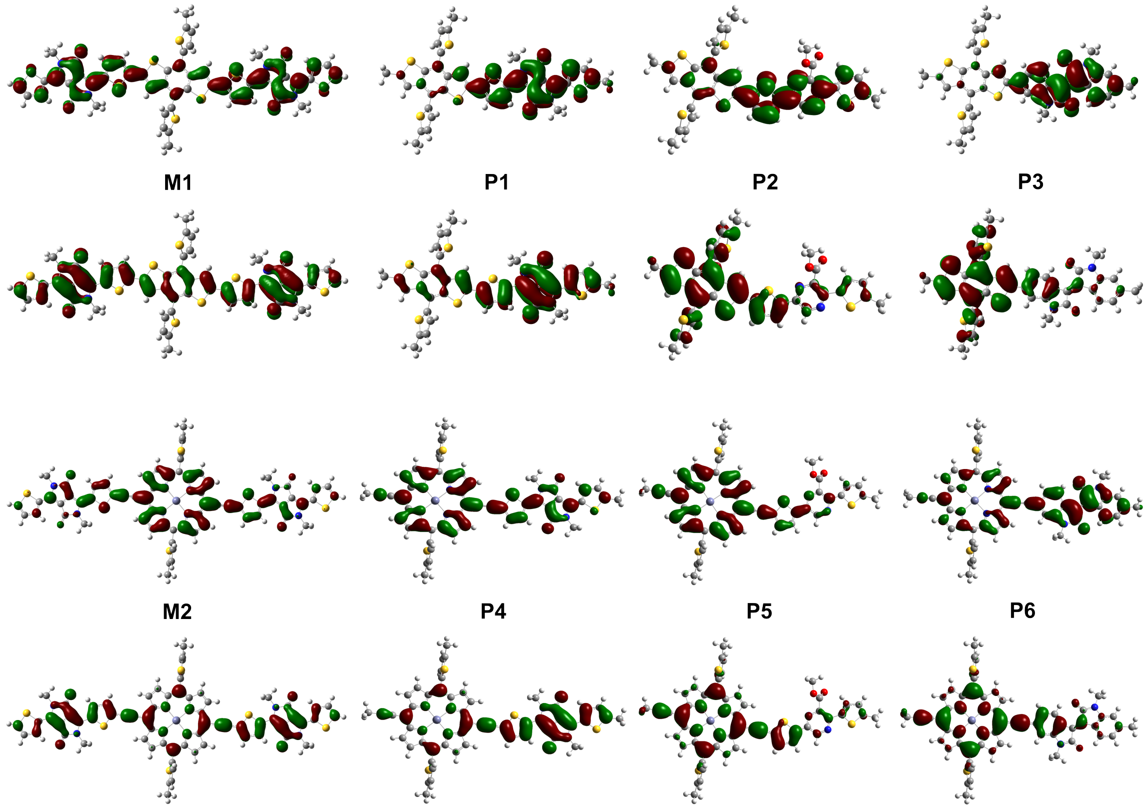

FIGURE 3.10: Representation of orbital localisation on all D-A compounds.

Calculations have also been carried out on the molecular bricks involved in all D-A systems to better rationalize the previous observations. All data are stored in table 3.4. When comparing the two donors, it is clear that BDT has the larger electronic gap and the deeper HOMO while the porphyrin has a more stabilised LUMO by 1.1 eV. Porphyrin would thus require stronger acceptor units to create D-A compounds if the porphyrin is chosen as a donor. Moreover, choosing BDT unit as a donor, as well spread in the literature, is not a so straightforward choice because of its really high electronic gap which might lead to a poor light absorption in the visible region.

P1 has both frontier orbitals mainly located on its A unit because the HOMO and LUMO of DPP are higher and lower in energy respectively than the frontier orbitals of BDT. In P2 and P3, the HOMO position is governed by BDT because PiP and Ind have a deep HOMO level and and LUMO localized on the A unit as expected. In the case of P4, frontier orbitals are well delocalised over the whole molecule since the molecular orbitals of the two bricks show that their HOMO and LUMO are very close, thus facilitating a full delocalisation and leading to a narrowing of the electronic gap. P5 has both orbitals mainly located on the porphyrin units for the same reason as P1 when looking at the molecular brick orbital energies; porphyrin has indeed a higher HOMO and a lower LUMO. As it is the case for P3, P6 has also a clear D-A structure when looking at their component orbital energies even if the charge separation is less pronounced that in the P3 case.

3.3.3 TD-DFT spectra

M1 and M2 results will be discussed as the structure is non polymerised whereas results for P1 to P6 systems will only focus on trimers of their respective monomer structure, as simulations fit better with experiments for long chains. All simulations take into account a spectral contribution for the PDI units present in the structure which is calculated separately. Experimental spectra were recorded in chloroform.

Both M1 and M2 present the same line shape as their experimental signature though the intensities of the S1 state are both overestimated compared to other peaks. The S1 state absorption occurs respectively at 590 nm (2.1 eV) and 700 nm (1,77 eV) while experimentally, the 0-0 transition occurs around 625 nm (1.98 eV) and 750 nm (1.7 eV) for M1 and M2 respectively. Peaks appearing around 500 nm correspond to the PDI group signals. The significative difference between experiment and simulation about peak intensities might originate from interactions between PDI units and the D-A core of the molecule.

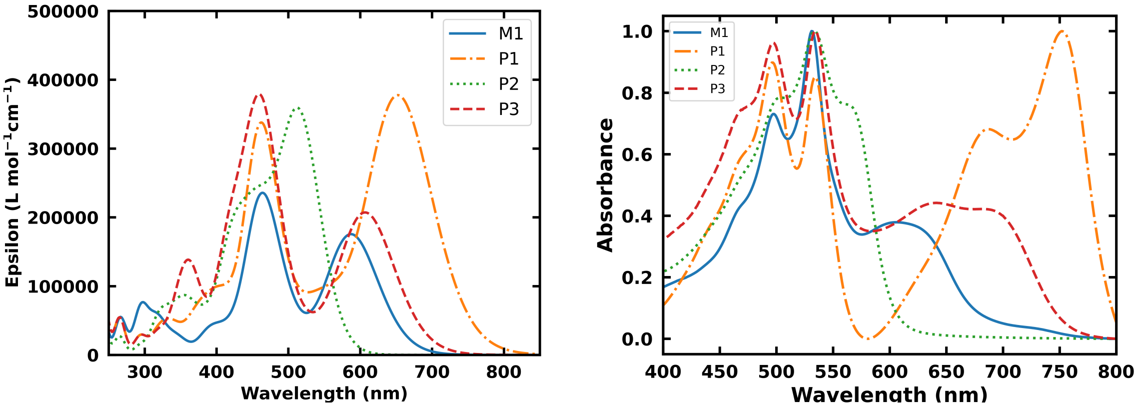

(A) BDT based system. TD-DFT simulated spectra and on the right experiment absorbance

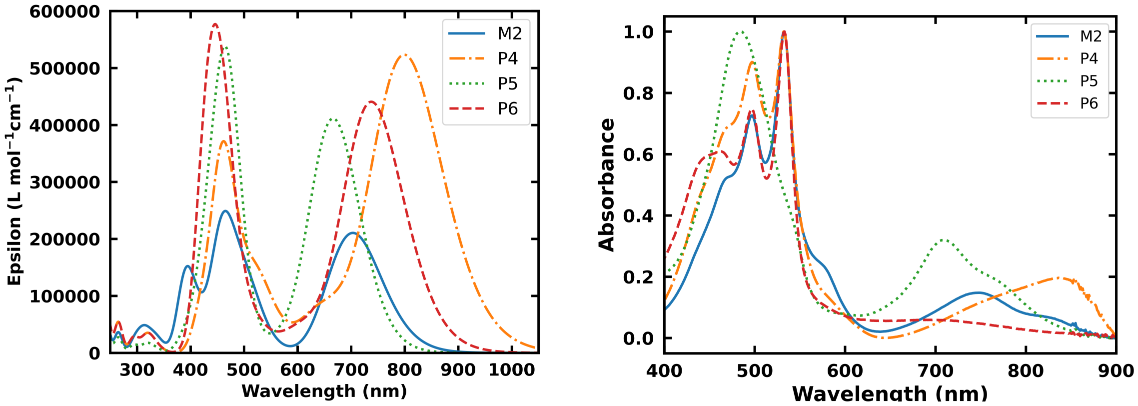

(B) Porphyrin based system. TD-DFT simulated spectra and on the right experiment absorbance

FIGURE 3.11: Absorption simulation and measurements carried out in chloroform at 10^{-6}M.

We can see some similarities between M1, M2 and ITIC or Y5 molecule in the structure and also in the S1 energy range since both systems absorb at similar energies,

Compounds	Excited state	Energy	Oscillator strength	Major orbital contributions	Overlap
M1	S_1	2.11 eV	1.95	H → L: 98%	83%
P1	S_1	1.90 eV	4.16	H → L: 90% H-1 → L+1: 6%	84%
P2	S_1	2.40 eV	3.76	H → L: 85% H-1 → L+1: 9%	75%
P3	S_1	2.04 eV	2.26	H → L: 79% H-1 → L+1: 10%	66%
M2	S_1	1.76 eV	2.34	H → L: 95%	78%
P4	S_1	1.55 eV	5.80	H → L: 88% H-1 → L+1: 9%	77%
P5	S_1	1.86 eV	4.5	H → L: 77% H-1 → L+1: 12%	79%
P6	S_1	1.68 eV	4.88	H → L: 98% H-1 → L+1: 9%	72%

TABLE 3.5: Description of the lowest excited state for each compound. Each excited state is associated with its energy, oscillator strength, major orbital contributions and overlap between departure and arrival orbitals.

670 nm (1.85 eV) for ITIC and 730 nm for Y6 (1.69 eV) experimentally. The main difference lies in the LUMO and HOMO energy systematically higher for M1 and M2 which could be an advantage to reduce energy offset between the donor and the acceptor in the blend. Indeed, although an energy difference is required for exciton dissociation, it is always a loss of energy because it will reduce the V_{OC}. This apparent advantage might also call for another polymer donor if its LUMO is not high enough for exciton dissociation. Nevertheless, M1 and M2 do not appear as more efficient at first sight since their 0-0 transitions are not as intense as ITIC nor Y5.

For all polymers, we end up with same findings as for M1 and M2, namely the line shape is well reproduced but relative intensities do not always match. The TD-DFT calculations provide S1 transitions respectively around 650 nm (1.91 eV), 510 nm (2.43 eV), 610 nm (2.03 eV), 800 nm (1.55 eV), 670 nm (1.85 eV) and 740 nm (1.68 eV) from P1 to P6. Experiments give the 0-0 transition around 750 nm (1.65 eV), 550 nm (2.25 eV), 700 nm (1.77 eV), 840 nm (1.45 eV), 710 nm (1.75 eV) and 700 nm (1.77 eV).

As predicted, BDT based systems show a larger optical gap than porphyrin based structures. The DPP unit always gives the largest red shift while PiP shows the smallest one while Ind gives an intermediate result, as predicted with orbital energies in section 3.3.2.

Let us now give a look at all S1 transitions that are described in table3.5. M1 and M2 show pure HOMO LUMO transition compared to polymers with higher overlap coefficient than ITIC or Y5 compounds, whose HOMO and LUMO orbitals are less delocalized. This makes M1 and M2 poorer acceptor as previous NFA systems since the exciton dissociation would be less effective, thus reducing the J_{SC} values.

Polymer trends confirm the previous observations made on the monomer orbital localisation. P3 does exhibit a smaller overlap value than P2 and P1 but the weaker oscillator strength of P3 implies that the probability of the transition to occur; and by extension the J_{SC} values should be significantly reduced.

Interestingly, the extension of the chain length has also an impact on the overlapping parameter. For BDT systems, it the overlap factor tends to increase by extending the chain length while the opposite behaviour prevails for porphyrin systems. Trends among the monomers are recovered in the polymers; moreover, the extension of conjugation stabilises the orbital energies and yields a better quantitative agreement with experiment.

Throughout all these data, the most promising compounds are those absorbing at relatively high wavelength and with the S1 state with a pronounced CT character. M1 and M2 could be blended with another donor polymer since they absorb at high wavelength and their S1 state arises essentially from a HOMO-LUMO transition. The weak CT character of P1 would obviously reduce its photovoltaic performances while P3 and P6 shows a good compromise between absorption intensity and CT character due to their intermediate overlap values and high oscillator strength combined with a relatively low S_1 energy.

3.4 Compound stability

3.4.1 Light irradiation impact

Absorption measurement is a useful tool to select compounds before blending them in a device but it is also a powerful tool to analyse external factors that might have an impact on the absorption response, such as chemical reactions. In fact, chemical modification will typically lead to a modification of the conjugation and to a change in the HOMO and LUMO distribution, and hence in the intensity and the energy of absorbed light.

NFAs are well known to suffer from degradation over time upon sunlight irradiation and exposure to O_2 and H_2O. What is less understood is the chemical mechanism of the reaction behind this degradation process. This section will tend to give a better understanding of this sometimes dramatic phenomenon for OPV applications.

Tracking the absorption signal evolution of several NFAs such as ITIC and ITIC-F under illumination has been done by Ackermann J. et al.[132] The analysis has been carried out in chloroform and in solid-state under N_2 atmosphere. In solution, the

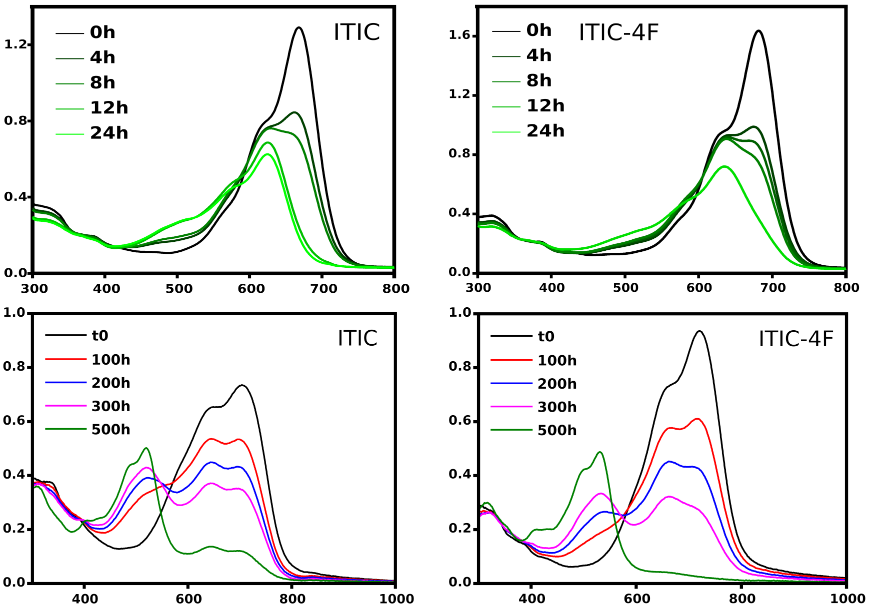

FIGURE 3.12: Absorption signals of ITIC and ITIC-F in N_2 atmosphere and under illumination over 24 hours in solution and 500 hours in the solid state taken from the article of Ackermann J. et al[132].

0-0 transition intensity drops drastically while peaks appear at lower wavelength, between 450 and 550 nm. During the 8 first hours of irradiation. The initial 0-1 transition appears unchanged but seems to be the 0-0 transition of the new formed product because after 12 hours, the initial 0-0 transition has completely disappeared and absorption signal seems blue-shifted. During the next 12 hours the peaks between 450 and 550 nm increase in intensity while the initial 0-1 peaks intensity continue to fall down. In solid state, this behaviour appears more clearly and confirms the presence of another compound formed upon light irradiation, as seen in fig.3.12.

Since the irradiation was carried out under inert atmosphere, the changes in the absorption spectra suggest the formation of a photoproduct resulting from a molecular structural modification. Fourier Transform Infra-Red (FTIR) analysis was then conducted to track the intensity variations of several chemical functions during the irradiation process for thin-film samples. The C=O bond signature appears at 1702 cm^{-1} and was displaced at 1716 cm^{-1} due to chemical environment perturbation during the light soaking. A previous study, performed by Park et al.[133] on ITIC photodegradation on ZnO surface has demonstrated the role of the vinyl bond connected to the 2-(3-oxo-2,3-dihydroinden-1-ylidene)malononitrile (INCN) moiety. The C≡N bond signature is located at 2220 cm^{-1} and decreases in intensity during the degradation process, confirming its implication in the degradation.

The chemical degradation was finally attributed to an electrocyclic reaction involving a *cis-trans* isomerisation followed by a Diels-Alder cycloaddition in solution and thin-films but at different rate since it only requires 24 hours in solution and 500 hours in the solid state to observe a full degradation of ITIC acceptors.

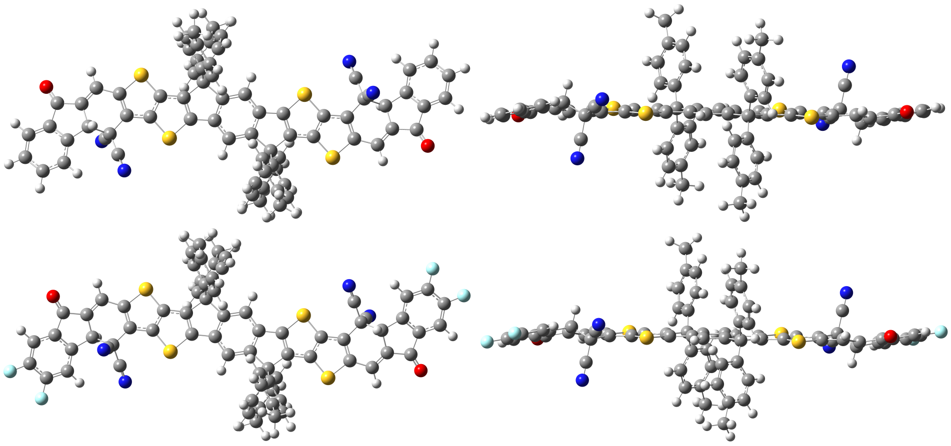

FIGURE 3.13: ITIC and ITIC-F degraded molecular structure under inert atmosphere and light illumination.

3.4.2 DFT analysis

The degradation mechanism has been further addressed by computing the geometry and properties of the suggest by-product using DFT calculations to confirm and understand The changes in the molecular structure. The geometry of the photoproduct is drastically different, with a reduced planarity and conjugation length by ring fusion. The C≡N groups are now out of the plane and no longer involved in the conjugation compared to the ITIC molecular structure. The same observations can be done on the ITIC-F molecule in fig.3.13.

Looking at their orbital energy levels, the HOMO energy is increased by nearly 0.1 eV while the LUMO energy is raised by 0.35 eV for ITIC, The evolution is identical In the case of ITIC-F. The orbital delocalisation is also affected, as seen on the fig.3.14. The weight of LUMO is now more important around the cyclopentenone groups and there is no electronic density on the malononitrile moiety. Considering the HOMO, the delocalisation remains quite similar except for its weak electronic density on the malononitrile bond. Very similar trends are observed for the ITIC-F system, which is not represented on the figure.

When computing the absorption spectra of degraded molecules, the S1 transition appears at 520 nm (2.38 eV) against 610 nm (2.03 eV) previously found in section 3.2.3 for the pristine compound, which results in a blue shift of about 90 nm (0.65 eV). The peak wavelength does not match precisely between experiment and simulation but the trend is verified as the 0-0 transition is blue shifted from 670 nm to 570 nm (0.33 eV), which has been attributed to the degradation of the product by Ackermann et al.

This further proved that malononitrile has a large impact on the π-electron conjugation and the push-pull effect that tend to red shit absorption signature. Because of the Diels Alder reaction, this chemical group is rotated and leaves the molecular plane, which reduces the conjugation length an impacts the absorption properties by a blue shift of the signal. This obviously will reduce performances in a device since

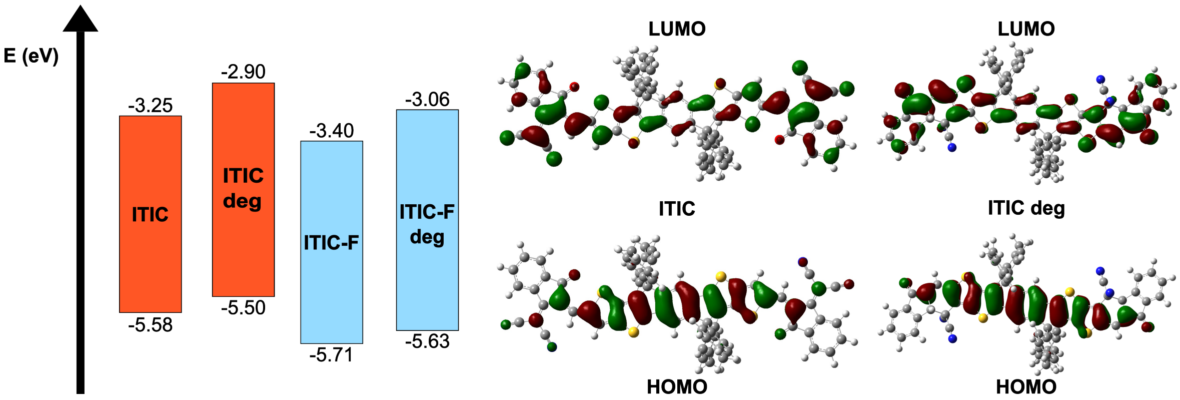

FIGURE 3.14: Energetic scheme of ITIC and ITIC-F frontier orbital energies and HOMO/LUMO delocalisation pattern on ITIC and ITIC degraded molecules.

less photons are available in this spectrum window and also because of the reduced intensity of absorption. This mechanism does not occur in BTP molecules because the thiophene carbon involved in the *cis-trans* isomerisation has an alkyl chain substituent which blocks the electrocyclic reaction. This structural change makes BTP molecule more stable against light irradiation.

3.4.3 Ambient air exposure

ITIC was then placed in contact of oxygen and moisture by removing the inert atmosphere conditions. Even in solution, oxygen appears to dissolve in sufficient quantities to interact with the molecule. It appears that the previous peaks rising between 450 and 550 nm do not show up in this context and only a reduction of 0-0 and 0-1 signal is recorded over the time of irradiation.

In parallel of the absorption signal tracking, mass spectrometry analyses were performed to track any change in the chemical composition. The working principle consists in ionising the compound to make it detectable by mass spectrometry by exciting a substrate containing the analyte and a matrix by a LASER. The matrix is initially prepared by dropping some µl of trans-2-[3-(4-tert-Butylphenyl)-2-methyl-2-propenylidene]malononitrile solution in chloroform and let it dry on a steel plate. Afterwards, some µl of the sample solution is deposited on the matrix to create co-crystals which will help to ionise and evaporate the compounds of interest but also to prevent chemical degradation during the ionisation process.

The results presented in fig.3.15 have shown successive increments of roughly +16 *m/z* of the protonated molecule which is originally located at 1427 *m/z*. Therefore, weak intensity peaks successively appear during the experiment at 1442, 1459 and 1475 *m/z* besides the appearance of molecular moieties resulting from molecular breaking, as described also by Guo J. et al.[134]. The most obvious compound with mass of 16 is the oxygen atom. This means that the molecule is reacting with compounds able to give an oxygen atom to ITIC under light illumination. Nevertheless, we have no clue of the active site where oxygen would specifically interact.

Some DFT calculations have been carried out on several hypothetical structure implying alcohol, ketone, or ether chemical function on several sites easily accessible for an oxygen atom, see fig.A.3. Their spectral signature follows globally the observed trend experimentally by showing a decrease in absorption signal. Nevertheless, none of these compounds can be designated to be more impacting than another. Moreover, analysis of the electronic properties did not help us excluding some of the mentioned above compounds. The literature suggests that all of these compounds should exist at the same time and that several oxidation steps are reducing the conjugation length, therefore impacting absorption signal via a blueshift and intensity reduction.

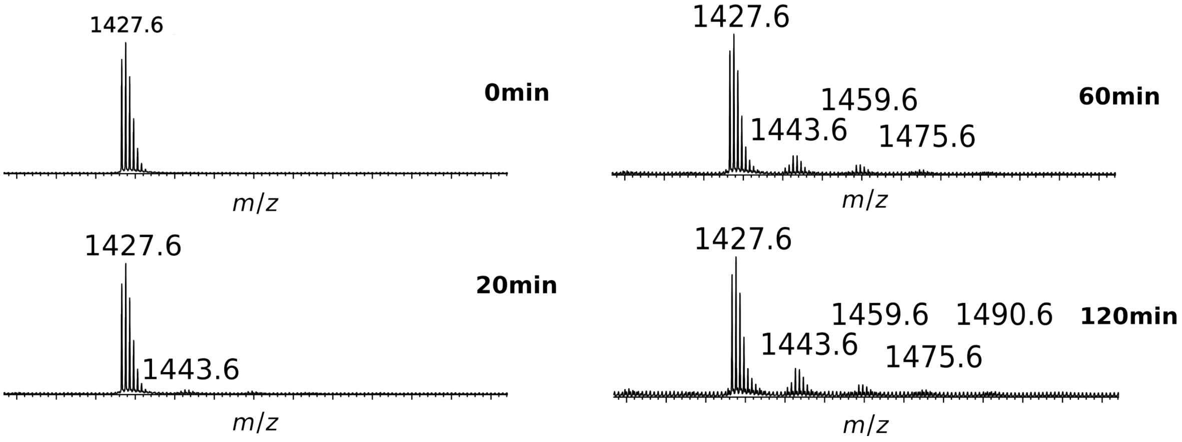

FIGURE 3.15: MALDI+ mass spectrum of ITIC and degraded derivatives. Molecular ion peak appears at 1427 due to the protonation and oxidised derivatives appears at every +16*m/z*. Each peak is affected by the isotopic probability distribution of their atomic components

3.5 Conclusion

In this chapter, we have presented all data acquired on ITIC, BTP and derivatives about their optical and electronical properties. Push-pull effects have been also highlighted in other D-A compounds in collaboration with the group of S. Clement. Moreover, NFA stability to light and oxidant atmosphere has also been discussed with preliminary results.

A complete theoretical approach associating DFT and TD-DFT calculations has enabled to describe precisely assets and drawbacks of famous NFAs: ITIC and BTP based systems. In parallel, experiments have confirmed our simulations results and justified the reliability of our theoretical approach. Geometry and shape of orbital energies give the foundations of their outstanding performances in OPV.

Halogenation does not have a real impact on the electronic characteristics except for the stabilisation of all electronic levels; in contrast, the electronic gap as well as the optical gap remain unchanged. NTO have nicely evidenced push-pull effects by showing departure and arrival areas of the electron during electronic transitions. The overlap between these two effective orbitals shows a CT character for all presented NFAs which helps to weaken the Coulombic interaction between the hole and the electron, and therefore enhance the charge splitting process.

Experiments have also raised other important features in the active layer. First, the red shift associated to the transition from solution to solid-state phase is most probably due to electrostatic interactions activated only in condensed phase. From crystallographic data, halogenated NFA appears to have a more compact structure, which is corralated to a larger red shift for chlorinated and fluorinated derivatives. This will considerably improve electrical conductivity of the active layer towards better performances. Y6 has shown a particularly large red shift probably associated to intermolecular interactions related to their intrinsic dipole moment.

Blending ITIC and BTP with the PM7 polymer donor has also been studied and has shown that the Y6 acceptor is more suited than ITIC due to a larger spectral coverage of the sun compared to the blend signature of PM7:ITIC blend. If the push-pull effect was not largely described in the previous section, the collaboration with the group of S. Clement on other D-A systems has led to a deeper understanding of the related important factors.

Many compounds have been described in this section and many data have been acquired. Several A moieties have been associated to two main D units and their intrinsic orbital energy and shape played an important role in the final compound orbital distribution, S1 transition energy and its CT character. Besides, the system size can also modulate the importance of the CT character by enabling larger delocalisation based on the ability of the D and A units to communicate.

Finally, light has been shed on the stability of these compounds which is also a crucial parameter for resilient OPV devices. Light has the ability to trigger isomerisation and chemical reaction that alter the molecular geometry and in fine affect the electronic structure irreversibly. After a long time of exposure, the spectral signature of ITIC is blue shifted and its intensity is drastically reduced, which is at the origin of the efficiency drop. On the contrary, Y6 does not show the same behaviour due to the presence of an alkyl side-chain disabling the cycloaddition mechanism.

Nevertheless, degradation process under ambient conditions still lacks some insight. Attempts have been made to find some intermediates or final degraded compounds to enhance our comprehension of the degradation mechanism by association of theory and experiments, tracking several aspects of the chemical reaction. It seems that a lot of compounds are created during the oxidation process, inevitably leading to a fragmentation process. Many sites are available for oxidation such as the bridge between the A and D units, the malononitrile groups or carbons forming thiophene cycles. More analysis needsto be done to understand each reactive site chemical activity and describe more precisely the competition process occurring during the oxidation.

Chapter 4

Morphology properties and device efficiencies

4.1 Introduction

In this section, deposition techniques and conditions of depot will be discussed, as well as their impact on the morphology of deposited films. In a second stage, we will use optimised deposition parameters to build testing devices and extract electrical characteristics.

Spin-coating is often used to build in a first stage OPV devices with new compounds. In fact, this deposition technique relies on few parameters to control the thickness and drying speed of the film but always guarantees to obtain a homogeneous film in a few minutes.

In parallel, thermal deposition is often used to avoid a crucial limitation of spin-coating: solvent orthogonality. Indeed, most of the OSC compounds can be dissolved in organic solvents. This prevents to deposit two OSCs on top of each other at the risk to dissolve the previous deposited layer. Thermal deposition enables the deposition of oxide compounds and other materials with low miscibility parameters by a heating process at very low pressure to sublime the material. The vaporous material will deposit homogeneously on the substrate at a fixed rate, controlling the thickness at the ångström scale.

First, the comparison of acceptors with different side-chains length revealed that this degree of freedom is a key parameter for OPV performances. We will consider Y6 and Y6-12 with the same chemical structure except for the inner side chains connected to the nitrogen atoms. On the one hand, side-chains are always attached to molecules to enhance solubility because of the large fused-ring backbone. On the other hand, once the solvent is fully evaporated, side chain will typically deteriorate the packing arrangement between molecules and reduce the OPV device efficiency. This chapter part has led to the publication of a paper in collaboration with Regnier F.[64].

Secondly, a comparison will be made between ITIC and BTP systems. As we have seen from their geometry in the DFT calculations in section 3.2 ITIC molecules

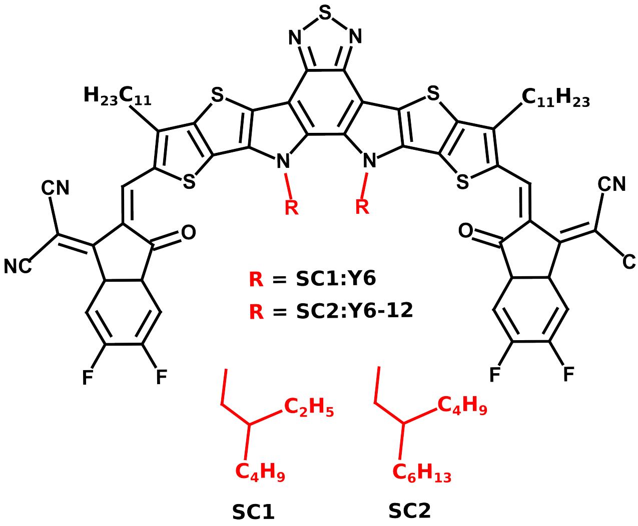

FIGURE 4.1: Y6 and Y6-12 Lewis chemical structure.

should exhibit more steric hindrance than BTP molecules. The morphological properties should be tailored accordingly to a balance between acceptor aggregation for good charge mobility and phase segregation for efficient exciton splitting.

Finally, we have focused on other layers and their deposition technique to highlight their impact on OPV device performances. Most of the papers push the development of new donor polymer or acceptor molecule while the interlayer compounds encountered are often the same. Nevertheless, oxide nanoparticles and conducting polymers have well known drawbacks such as acidity or a photo-catalyst character, such as with PEDOT:PSS polymers or SnO_2 nanoparticles. Some π-conjugated molecules have been introduced but are most of the time hard to deposit and do not allow easy reproducibility in terms of device efficiency. In this section, the presented results will display the complexity of using a full spin-coating method to build working device and the challenges behind the conception of new device architectures.

4.2 Side-chain influence on device efficiency

4.2.1 AFM morphology images

The molecular structures are presented in fig.4.1 with structural differences lying in the addition of two ethyl groups on each inner alkyl chain, in red on the figure, for Y6-12. DFT calculations have been carried out in the previous chapter only on the conjugated backbone because side-chains do not affect the optical and electronic properties. Their usefulness lays rather in the solubility of the compounds, an important parameter to obtain homogeneous thin films for OPV devices. Films have been deposited by spin-coating from solution in chlorobenzene (CB) and chloroform (CF) for pristine Y6, Y6-12 and PM7 before making PM7:Y6 and PM7 Y6-12 blends in an even concentration to achieve an average of 100 nm thickness.

Neat AFM measurements are presented in fig.4.2. The PM7 polymer shows for both solvent an identical behaviour, exhibiting a smooth surface morphology with a roughness (R_q) estimated at 1.0 nm in CB and 0.06 nm in CF. A fibrillar aggregation structure of about 30 to 70 nm length, observed through AFM measurements, highlights a significant organisation degree, as reported by Ma et al.[135,136]. In contrast, Y6 tends to aggregate more strongly by forming domain size of about 40 to 110 nm. R_q are accordingly affected by showing values of 5.1 nm in CB and 2.8 nm in CF. Y6-12 appears to aggregate less and the surface to be smoother, with R_q values reaching 0.4 nm and 0.3 nm in CB and CF respectively.

Y6 appears to have a higher propensity to make agglomerates than Y6-12 which could be explained by the size of the side chains that are longer than those of Y6 but also because of the branches that enlarge the area of side-chain action. Besides, pre-aggregation should be less pronounced due to the higher steric hindrance[137].

Blends of AFM images, seen in fig.4.3 of the PM7:Y6 obtained from CB solution exhibits a granular morphology similar to Y6 neat films with R_q value of 4.7 nm. Surprisingly, the same blend processed in CF reached a R_q of 0.9 nm and shows a smoother surface without a grain like structure, looking like the PM7 neat film. This implies that organisation is dominated in the first case by Y6 and in the second case by the polymer. Blends made of PM7 and Y6-12 behave similarly in both solvents and show an apparent higher degree of organisation. Film roughnesses are also very close, with 1.5 nm in CB and 1.2 nm in CF. The blend exhibits a structure in filament, indicating that the polymer plays a major role in the film organisation. Two main types of morphology have been observed: granular and filamentary aggregations. Filament formation, driven by the polymer, should favour charge transport along the polymer chain axis and improve the photocurrent intensity. In contrast, grains of large size are expected to reduce exciton dissociation rate by reducing the donor-acceptor interface size[136].

Post treatments are often necessary during the device conception process. Annealing is quasi always employed to improve the active layer morphology but also for inter-layers in some cases[138]. It allows for small rearrangements in the film morphology by giving to polymers and molecules sufficient energy to move in the condensed phase. Temperature and timing need to be carefully controlled to avoid the film burning. Annealing on PM7, Y6-12 and PM7:Y6-12 cast from CF solution have not shown significant result on the molecular organisation. Nevertheless, Y6 and PM7:Y6 from CB solution exhibit a radically different behaviour by increasing the roughness values, going from 5.1 nm to 9.9 nm in neat Y6 films and 4.7 nm to 7.8 nm for the blend. This proves that annealing can enhance the aggregation, leading to larger grains.

4.2.2 Electrical characterisation

The impact on morphology has been established when varying the solvent chosen and the applied annealing post treatment in certain cases. To illustrate further these effects, testing devices have been built with active layer of PM7:Y6 and PM7:Y6-12

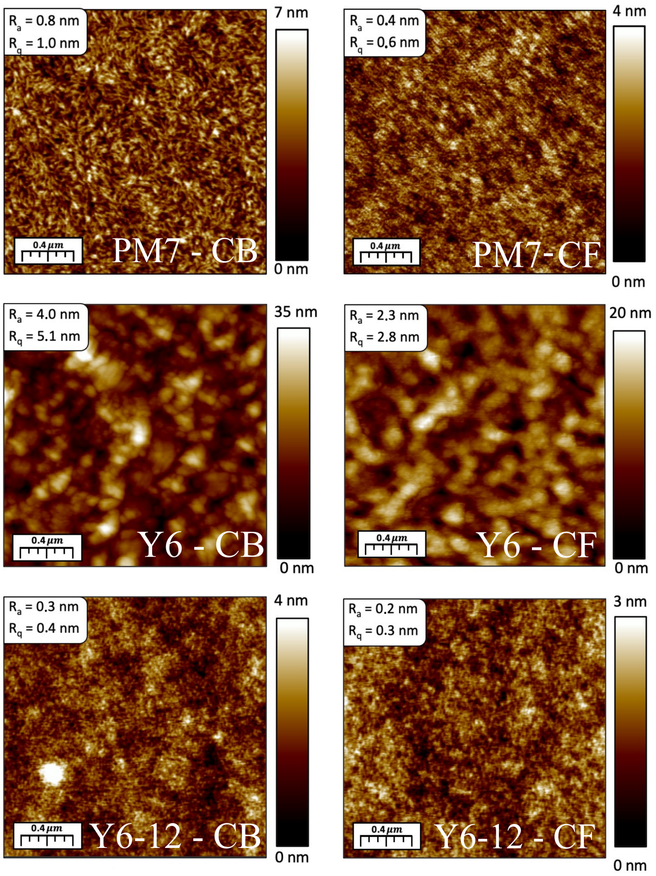

FIGURE 4.2: AFM images (2 x 2 μm²) of PM7, Y6 and Y6-12 thin-film morphologies cast from CB and CF solutions.

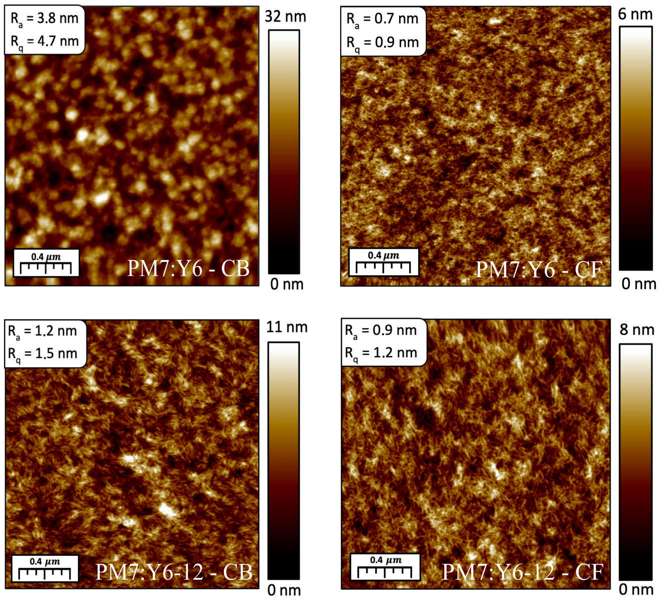

FIGURE 4.3: AFM images (2 x 2 μm²) of blend of PM7:Y6 and PM7:Y6-12 thin-film morphologies cast from CB and CF solutions

both spin-coated from CB and CF solution to reach an average of 100 nm (blends are always respecting the 1:1 proportion between the donor and the acceptor).

The testing device was built as follows: glass/ITO/SnO_2/Active layer/MoO_3/Al. ITO glasses are obtained commercially and are cleaned by being plunged in successive bath of soap and water, acetone and isopropanol (IPA). Between each bath, the substrate is cleaned by pouring distilled water on it. To improve wettability, a post treatment is applied by putting the substrates in an oxygen plasma cleaner. The ETL SnO_2 layer is then deposited by spin coating a mixture of butanol and nanoparticles of tin oxide to achieve less than 10 nm thickness and is then annealed at 150°C for 30 minutes by placing substrates on a hot plate. After, blends are deposited and annealed at 100°C for 10 minutes. An HTL layer made of MoO_3 is thermally evaporated on top of the active layer with a thickness target of less than 10 nm. Finally, the device is finished with the deposition of an Al layers of 100 nm roughly by thermal evaporation. Each device contains 8 analysis spots of 2.56 mm^2. The testing procedure consists in current measurement for an applied voltage ranging from -1.5V to 1.5V in the dark and under illumination from the solar light simulator. Results are stored in fig.A.4 and tab.4.1.

Active layers obtained from CF solution give similar results with a V_{OC} of 0.8 V for both acceptors, a J_{SC} of -14.6 mA cm^{-2} and 14.8 mA cm^{-2} for PM7:Y6 and PM7:Y6-12 , and a FF of 57% and 59% respectively leading to a maximum obtained PCE of 7.28% and 7.44% respectively. This is consistent with the AFM analysis, showing a rather good miscibility of both acceptors in CF. The moderate yields obtained might come from the difficulty to make active layer out of CF solution because of its low boiling point temperature; it already evaporates before starting the spin-coater. Active layers prepared from CB solutions show more distinct differences in performance. While V_{OC} and FF remain constant, J_{SC} values reach -11.02 mA cm^{-2} for PM7:Y6 against -20.54 mA cm^{-2} for PM7:Y6-12, leading to PCE values of 5.54% and 11.12% respectively. Side chain length clearly demonstrates their importance for these results, as confirmed by AFM images.

I-V curves obtained in the dark give information about the electrical circuit. All blends exhibit low series and high parallel resistances, pointing to good charge extraction and good electrical contacts but also to the absence of leakage that may come from inhomogeneity in the layers. Comparing devices, Y6 blends show systematically lower series resistance in the dark and under illumination which originate from lower interface and bulk resistances. Drastic drops in parallel resistance under illumination, compared to values in the dark, reflect the energetic disorder and charge carrier traps that create charge percolation pathways that prevent homogeneous charge extraction and are thus detrimental for OPV devices[139].

The different morphologies obtained from PM7:Y6 and PM7:Y6-12 from CB solutions impact the J_{SC} values because the granular morphology associated to a lower miscibility of the Y6 blend increase the domain sizes and reduce the exciton dissociation rate; indeed, many exciton cannot there reach a donor acceptor interface. Other electrical characteristics may not be impacted or are slightly better than the

PM7:Y6-12 blend because lower phase segregation generally improves charge transport.

Active layer	Solvent	J_{SC} (mA cm^{-2})	V_{OC} (V)	FF (%)	PCE (%)
PM7:Y6	$CHCl_3$	14.04 ± 0.50	0.87 ± 0.01	56.46 ± 0.76	6.91% ± 0.27
PM7:Y6-12	$CHCl_3$	14.86 ± 0.76	0.84 ± 0.01	55.50 ± 2.41	6.96 % ± 0.37
PM7:Y6	C_6H_5Cl	10.53 ± 0.41	0.82 ± 0.01	61.44 ± 0.92	5.25% ± 0.19
PM7:Y6-12	C_6H_5Cl	20.43 ± 0.18	0.83 ± 0.01	63.62 ± 1.20	10.84% ± 0.26

Active layer	Solvent	R_{serie}light	R_{serie}Dark	R_{shunt}light	R_{shunt}dark
PM7:Y6	$CHCl_3$	1.54 ± 0.19	1.60 ± 0.19	405.4 ± 10.36	46342 ± 20219
PM7:Y6-12	$CHCl_3$	27.58 ± 6.07	47.78 ± 12.88	445.20 ± 54.88	38181 ± 32358
PM7:Y6	C_6H_5Cl	0.70 ± 0.07	0.70 ± 0.97	532.20 ± 29.85	14708 ± 9820
PM7:Y6-12	C_6H_5Cl	10.34 ± 2.94	16.00 ± 5.71	488.80 ± 16.63	5382 ± 1845

TABLE 4.1: Device electrical parameters obtained for PM7:Y6 and PM7:Y6-12 blends in CF and CB, as averaged on 5 spots of a single substrate respectively. All resistances are expressed in (Ω cm^{-2}).

Actually, this section highlights the importance of the solvent drying kinetic and the acceptor aggregation capability more than only compound solubility. In the case of PM7:Y6 active layer, best performances can be achieved by spin-coating the solution from CF solvent because it evaporates quickly and does not allow Y6 to agglomerate too much during the film growth, enabling higher exciton dissociation rate. In the case of PM7:Y6-12, CB solution enables higher efficiency because Y6-12 agglomerates much slowly because of the longer side-chains. CB evaporates slower than CF because of the higher boiling point temperature and higher correlated viscosity, and let Y6-12 make sufficient large aggregates to increase charge extraction. Indeed, series resistances are more than twice lower comparing CF and CB cast active layers.

4.3 NFA end-cap halogenation

4.3.1 AFM images

Comparison of morphology and device efficiency has been performed on halogenated NFAs using ITIC-F and ITIC-Cl as acceptors and PM7 as donor. Both acceptors have been dissolved in CB solvent since our study on Y6 has shown that steric hindrance is better accommodated with more viscous solvent to obtain more efficient devices. ITIC acceptors do have more steric constrains with their phenylhexyl side-chains than BTP acceptors.

Neat film shows two radically different morphologies, as presented in fig.4.4. ITIC-F exhibits a homogeneous granular morphology with a 0.4 nm rugosity while ITIC-Cl shows a granular morphology with larger agglomerates and rugosity of 8.9 nm,

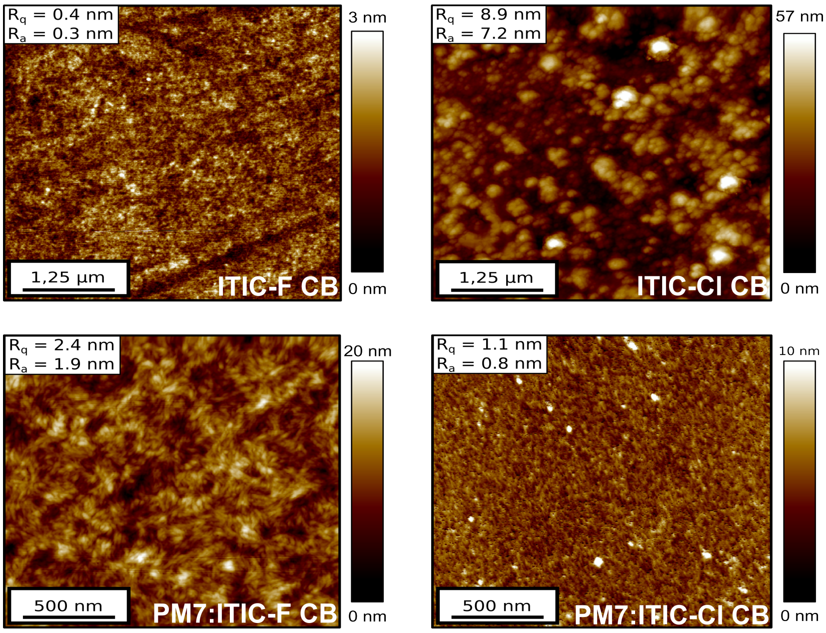

FIGURE 4.4: AFM images of ITIC-F, ITIC-Cl and blend of both NFA with the PM7 polymer. All films are cast from CB solution.

implying a lower solubility of the chlorine derivative and stronger intermolecular interactions which correlate with observations from absorption spectra in section 3.2.4.

Blending both acceptors with the donor polymer gives a filamentary morphology in the ITIC-F sample while a granular arrangement is maintained for the ITIC-Cl blend. PM7:ITIC-F AFM images exhibit the polymer driven morphology, indicating that the fluorine derivative has a good miscibility with the donor, as confirmed by the 2.4 nm rugosity. In fact, the polymer always has the lowest solubility compared to small molecules. PM7:ITIC-Cl does not show a good miscibility between the donor and the acceptor despite the improved rugosity reaching 1.1 nm. Indeed, white and black spots on the image point to a persistent low solubility of ITIC-Cl in CB and solvent evaporation difficulties, which promotes a lower phase segregation and a low photo-generated current besides a low FF parameter.

4.3.2 Device IV curves

Devices incorporating both blends have the same architecture as those used in the study of the side-chain length impact, i.e. glass/ITO/SnO_2/Active layer/MoO_3/Al, and are represented in fig.A.5 and tab.4.2. PM7:ITIC-F exhibits higher PCE values of 9.93% against 0.45% for PM7:ITIC-Cl, denoting bad conditions for the active layer preparation. J_{SC}, V_{OC} and FF values reach -18.52 mA cm^{-2}, 0.86 V and 62.4% for PM7:ITIC-F and -2.18 mA cm^{-2}, 0.65 V and 31.4 % for PM7:ITIC-Cl.

These results correlate with AFM observations about miscibility and aggregation.

Active layer	J_{SC} (mA cm^{-2})	V_{OC} (V)	FF (%)	PCE (%)
PM7:ITIC-F	18.52	0.86	62.4	9.93%
PM7:ITIC-Cl	2.18	0.65	31.4	0.45%

Active layer	R$_{serie}$light	R$_{serie}$Dark	R$_{shunt}$light	R$_{shunt}$dark
PM7:ITIC-F	10	20.9	1241	97200
PM7:ITIC-Cl	0.7	0.7	428	3885

TABLE 4.2: I/V parameters obtained for PM7:ITIC-F and PM7:ITIC-Cl blends in CB. All resistances are expressed in (Ω cm^{-2}).

The ITIC-F blend has a more important phase segregation which improves the charge generation while keeping large enough domain sizes to keep high charge mobility, This is confirmed by low series resistivity either in dark and under illumination with respective values of 20.9 and 10 Ω cm^{-2}. ITIC-Cl blends do not show sufficient phase segregation between the polymer and the NFA, which turns into a dramatic impact on J_{SC} values. Nevertheless, the device keeps a relatively high V_{OC} and low series resistances (0.7 Ω cm^{-2} in the dark and under illumination) because a large domain size is favourable for charge transport.

On the other hand, shunt resistance values are relativity lower in the case of the ITIC-Cl blend than in the case of ITIC-F. Respective shunt values in the dark and upon irradiation are 97200 Ω cm^{-2}, 1241 Ω cm^{-2}, 3885 Ω cm^{-2} and 428 Ω cm^{-2} for PM7:ITIC-F and PM7:ITIC-Cl. ITIC-Cl blend low shunt resistance in the dark points to a non homogeneous charge percolation through the whole illuminated surface, correlated with low FF values. The interface contact is thus poor and opens the way to a leakage current, as supported by the AFM images.

There is still an important remark to be made about absolute PCE values. They are systematically lower than those reported in the literature for many reasons. First of all, finding a good match between a donor polymer and an NFA is far from easy due to the need for complex tailored structure behind the intrinsic parameter optimisation such as light absorption, solubility in commonly used solvent, compromised between aggregation and phase separation,. . . and the compound price. Secondly, many fine tunings can be applied on the annealing temperatures, active layer thicknesses, solvent compositions,. . . . Finally, the inter-layer compounds play a non negligible role on the FF factor and charge extraction properties.

4.4 Device construction recipes

An internship in Brilliant Matters (BM) company was the occasion to deepen my knowledge on device fabrication and device electrical response. During three months, the main project was to build a device only using a spin-coater as deposition method. It can be useful to test a lot of devices to reduce fabrication time in comparison to the use of a thermal evaporator. In parallel, other active layers and inter-layer compounds have been tested to analyse their impact on performances.

Since their facilities do not possess state-of-the-art testing materials, every testing device is built in ambient air in contrast to the previous results shown. Their device structure, glass/ITO/PEIE-Zn/Active layer/BM-HTL/Ag, implied an active layer made of PM6 donor polymer and Y7-12 NFA, an ETL made of a blend of polyethylenimine ethoxylated (PEIE) and ZnO nanoparti-cles[140] and an HTL made of BM-HTL compound, a conductive and transparent polymer commercialised by BM.

The first encountered challenge was to select a soluble electrode. In fact, the materials involved require a high electrical conductivity for a good extraction of charge carriers and metals best suit this role. Nevertheless, metallic structures are not soluble and are usually deposited via thermal evaporation in the OPV field. on the contrary, conducting polymers are more easily dissolved and can be deposited homogeneously but their conducting properties are usually inferior to metals. Another possibility consists in reducing the material size which enables to conciliate metal conductivity and solution based processing, such as by using silver nanowires or carbon nanotubes.

4.4.1 Electrode selection and spin-coated device

Among several compounds, silver nanowires provide the ability to be deposited on top of organic compounds thanks to an isopropanol dispersion formula, with a sufficiently low resistivity. Nevertheless, a solvent test has been performed, seen on fig.4.5, on the BM-HTL layer to list all orthogonal solvents and increase the probability of compatible electrode formulation. Tested solvents are listed as follows, H_2O, IPA, DMSO, CH_3CH_2OH, H_2O + triton 5% as they are very common in OPV device formula. Testing device is similar to the previous description except for the electrode that is made of metallic silver thermally evaporated.

Only water and IPA do not affect IV characteristics compared to the reference meaning that no alteration on the HTL layer occurred. Nevertheless, water does not wet on any organic layer, so that only IPA solvent for the top electrode is retained. DMSO and ethanol have both altered the IV device signal but at different scale. DMSO has reduced the V_{OC} and the FF values while ethanol impacts drastically the FF parameter but also altered V_{OC} and J_{SC} parameter. Finally, water and triton (surfactant) mixture has definitely dissolved the whole organic layer because of the absence of any photocurrent.

Ethanol has probably dissolved the HTL layer without affecting the active layer which could explain the nearly preserved V_{OC} and J_{SC} values, reducing the active layer and HTL interface homogeneity and creating current leakage. DMSO, for its part, penetrates more deeply in the device and also affects the active layer. It does

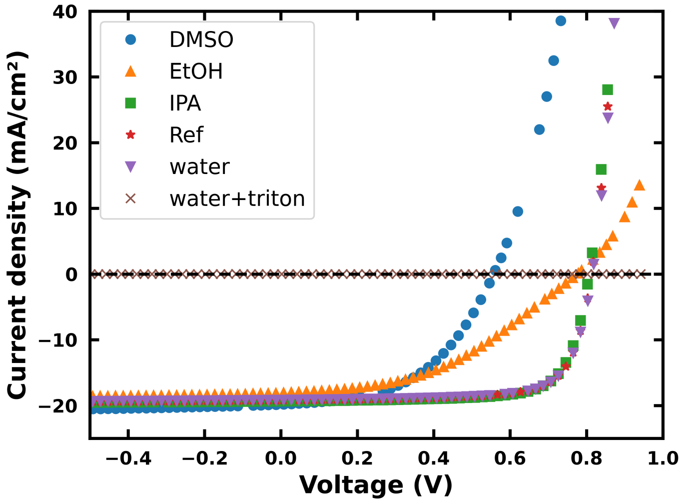

FIGURE 4.5: IV curves of devices glass/ITO/PEIE-Zn/PM6:Y7-12/BM-HTL/Ag showing effect on electrical characteristics of several solvent on the HTL layer.

not modify the phase segregation because of a maintained J_{SC} but creates more energetic disorder and therefore more traps for charge carriers, which is correlated to a drastic reduction of V_{OC} and FF values.

Afterwards, many attempts were carried out to achieve the best performances with the device structure implying silver nanowires. One of the main problem was the too weak dispersion concentration so that successive deposits were required to thicken the electrode layer but also the electrode patterning. Indeed, testing devices are made of eight independent measuring spots while the electrode deposition spreads over all of them. Manual delimitation is then required to keep the same illumination area to compare with other results. Finally, a PCE of 9.4 % is achieved with J_{SC}, V_{OC} and FF values of 13.97 mA cm^{-2}, 0.79 and 68% respectively which is reasonable regarding the prototypical device construction.

Interestingly, the nanowire-based nature of the electrode makes it semi-trans-parent which could be interesting for certain applications though it also reduces performance. In fact, for plain silver devices, non absorbed entering photon can be reflected by the electrode and be absorbed while exiting the device which is not feasible in semi-transparent devices. It is commonly admitted that an average of 30% PCE loss is due to transmitted photon across the device.[141].

4.4.2 Impact of the device architecture on OPV properties

In parallel, the studied active layer PM7:Y6 was built with different inter-layers and also compared to the PM6:Y7-12 blend which involves quasi similar compounds but with F atoms on the polymer donor and Cl atoms on the NFA molecule. ETL tested compounds are SnO_2 and ZnO nanoparticles, and PEIE-Zn mixture while HTL tested compounds are polymer BM-HTL and MoO_3. Finally, another solvent is introduced in the active layer formulation, the O-xylene solvent. All I-V curves used in this comparison are presented in fig.4.6

The first comparison takes into account CB and xylene solvent for the active layer processing in the following device architecture: glass/ITO/PEIE-Zn/PM7:Y6-12/BM-HTL/Ag. O-xylene seems to slightly improve performances as its boiling point temperature is roughly 10°C higher than CB and will lead to a better active layer morphology as demonstrated in section 4.2. Best values obtained for CB formulation are 0.83 V, 17.78 mA cm^{-2}, 68% and 12.66% for V_{OC}, J_{SC}, FF and PCE respective values while for O-xylene, these values are recorded at 0.81 V, 18.19 mA cm^{-2}, 71% and 13.16%.

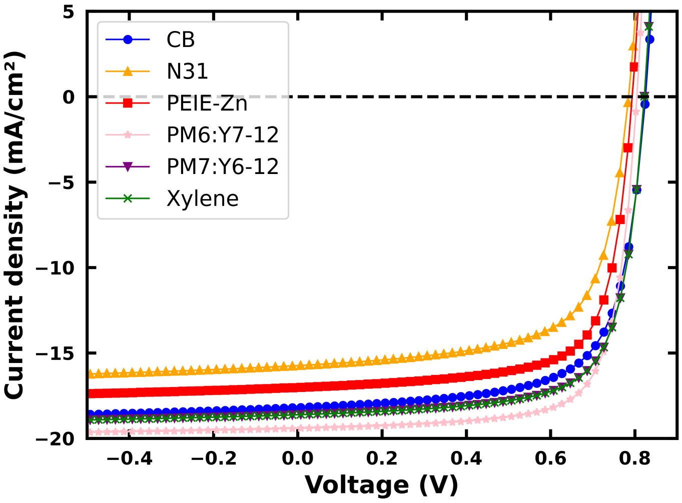

FIGURE 4.6: IV curves of devices used for efficiency comparison while changing ETL compounds, active layer composition and solvent for the active layer formulation. the purple PM7:Y6-12 and the green xylene curves are plotted using the same recorded data.

Regarding the active layer composition, comparing devices having both PEIE-Zn as ETL and BM-HTL as HTL plus having a cast active layer from O-xylene solvent, the reached PCE for PM6:Y7-12 is 14.08% with 0.80 V, 18.92 mA cm^{-2} and 74% as V_{OC}, J_{SC} and FF values while PM7:Y6 yields a PCE of 13.16% with 0.81 V, 18.19 mA cm^{-2} and 71% as V_{OC}, J_{SC} and FF values. The difference lays in the current density and the fill factor which is explained by a potential increased phase segregation while keeping a low energetic disorder. As seen with ITIC-Cl in section3.2.4, putting chlorines on the acceptor may be responsible for better intermolecular interactions between NFAs while fluorines improve polymer miscibility and thus phase segregation.

Finally, changing ETL composition to compare SnO_2 with PEIE-Zn in device structure glass/ITO/ETL/PM7:Y6-12/MoO_3/Ag can also largely affect the performances. Indeed, SnO_2 devices achieve a PCE of 9.96% with 0.79 V, -15.18 mA cm^{-2} and 67% of V_{OC}, J_{SC} and FF parameters while PEIE-Zn allows to reach PCE of 11.81% with 0.79 V, 16.54 mA cm^{-2} and 72% for the V_{OC}, J_{SC} and FF parameters. Indeed SnO_2

nanoparticles create a rougher interface with the active layer which is always reducing FF and will also affect a bit J_{SC} concomitantly because of the less homogeneous charge transfer to the inter-layer. This is confirmed by reduced shunt resistance meaning that there are preferred pathways for charge carrier in contrast to the smoother PEIE-Zn ETL showing higher shunt resistance values.

4.5 Conclusion

Several structural parameters and their impact on device performances have been highlighted. First, the length of the side chains has a drastic influence on the compound solubility but also on the domain size and aggregation process during the spin-coating. Moreover, depending on the side-chain length, performance can be modified by choosing the best solvent based on its viscosity. Indeed, for shorter side chains, aggregation will be improved therefore a low viscosity solvent is required to maintain a sufficient phase segregation while with longer side chain, the dynamic is radically opposed with the choice of a more viscous solvent to enable a better packing and reach sufficient domain size for an effective charge conductivity.

Secondly, end-cap modification has also shown strong effects on device efficiency. Comparison between chlorine and fluorine end-cap moiety gives information about intermolecular packing and active layer morphology. In fact, the previous chapter has already pointed to more interactions between chlorinated NFA and less solubility than fluorinated ones, which is confirmed by an AFM analysis of neat ITIC-F and ITIC-Cl thin films. Moreover, electrical characterisation has also demonstrated the poor current density of chlorinated NFA based active layer correlated to a poor phase segregation. This means that a less viscous should be used instead of the chlorobenzene.

Finally, data from the internship made in the BM company have highlighted the critical choice of other layers in the device performances. A semi-transparent device has been built and shows decent performances with a brand new construction recipe. Orthogonality of solvents has been discussed, showing the difficulty behind the spin-coating deposition technique to successively stack organic layers. Finally, this has also been the occasion to create multiple device structures by changing the nature of ETL, HTL and active layer. Surprising changes in device PCEs and electrical characteristics have been recorded for different reasons such as layer morphology or compound miscibility. These are basic reasons behind the performance gap between home-made devices and device mentioned in the literature. Many parameters are not tailored in this work and explain the non optimal results of OPV devices.

Chapter 5

Charge carrier mobility

5.1 Introduction

Charge transport is obviously an important parameter for efficient devices and is related to the morphology and optoelectronics properties to a certain extent. Charge mobility in thin film OSC can be probed in several manners such as using Organic Field Effect Transistor (OFET), Space Charge Limited Current (SCLC) or Impedance Spectroscopy (IS). Each method outputs a different value and requires specific experimental conditions to guarantee a certain degree of consistency.

Experimentally, the IS technique was established to stick closer to charge transport dynamics in OPV devices. In fact, OFETs are well designed for longitudinal transport analysis, along the channel between the source and the drain; however, this is not suited for OPV devices that are built vertically. Another alternative would then be to consider SCLC measurements but with non negligible drawbacks such as high required voltage or thick layers. Indeed, the truly SCLC regime, $I \propto V^2$, is usually achieved at high applied potential difference. Such conditions usually fill traps and give higher mobility values than effective mobility in OPV working conditions at low voltage.[142,143].

IS measurement techniques can be easily set up for various cases of study but have a main limitation: it requires a fictive electrical circuit to fit the electrical device response and extract all charge behaviour informations. It requires then a deep comprehension and description of the analysis to obtain consistent results. In our case, the device structure and the analysis method is explained in section 2.2.4.

Preliminary results will be shown on polymer neat and blend thin films to probe hole transport. Unfortunately, major technical limitations have been encountered and impeded the experiment set-up to probe electron transport mechanism in the neat and blend films. Originally, to support these results, DFT simulations have been carried out on crystallographic structures to predict charge transport directionality in NFA-based condensed structure. These calculations consist in estimating, in first approach, the orbital overlap between frontier orbitals of nearest neighbours to estimate preferential charge migration pathways.

Finally, n-doped π-conjugated molecules have recently boosted a certain interest for thermoelectric generator applications. Indeed, organic molecular crystals have demonstrated low thermal conductivity while introducing dopant has enabled large improvement in their electrical conductivity characteristics. An experimental study has been performed by Wang S. et al. on two small π-conjugated molecules, TIFDKT and TIFDMT, with a chemical structure close to the ITIC donor core and a collaboration has been established with our group to further study these compounds at the DFT level.

AFM and GIWAXS experiments leaded by Wang S. et al. indicates strong opposite behaviour for both molecules upon doping with NDMI molecule. Morphology parameters shows a lower miscibility in the case of TIFDMT but an more dense and an improved crystallinity compared to the TIFDKT thin-films

Accordingly, molecular dynamic simulations should have been carried out following the collaboration with Wang S. but due to to high constraints and technical issues, no exploitable results have been collected to completely support the work of our collaborators on π-conjugated molecules.

5.2 Charge mobility experiments

Performing IS measurements on such a complex device requires a step by step electrical response probing to validate hypotheses of probing mechanism (cfr: 2.2.4). The following tests have then been performed successively:

- Al_2O_3
- Al_2O_3 + MoO_3
- Al_2O_3 + OSC +MoO_3

The capacitive responses of both devices without the OSC are presented in the fig.5.1. One can see a constant capacity value of 5 nF at low frequency, dropping to 0 after 10^6 Hz, meaning that the impedance response of the AC current is governed by the resistance component beyond this frequency, as also confirmed by the conductance values rising at the same frequency. Adding the hole blocking layer increases the capacity value to 7 nF because oxides are poor conductive materials but its thickness is relatively thin here. Small decreasing trend upon AC frequency increasing shows the inter-layer capacity response but is sufficiently low to be neglected in further analysis. The significative perturbation occurring around 50-60 Hz originates from the electric interferences from surrounding electrical operating devices and installations.

After this system layer calibration, the capacity response of OSC layers have been recorded and shown in fig.5.1First tested OSC includes the PM7 polymer. The capacitive drop at very low frequency probably comes from non significative perturbations while the significative transition regime between 10^5 and 10^6 Hz is correlated to the charge mobility behaviour transition occurring when charge carriers cannot

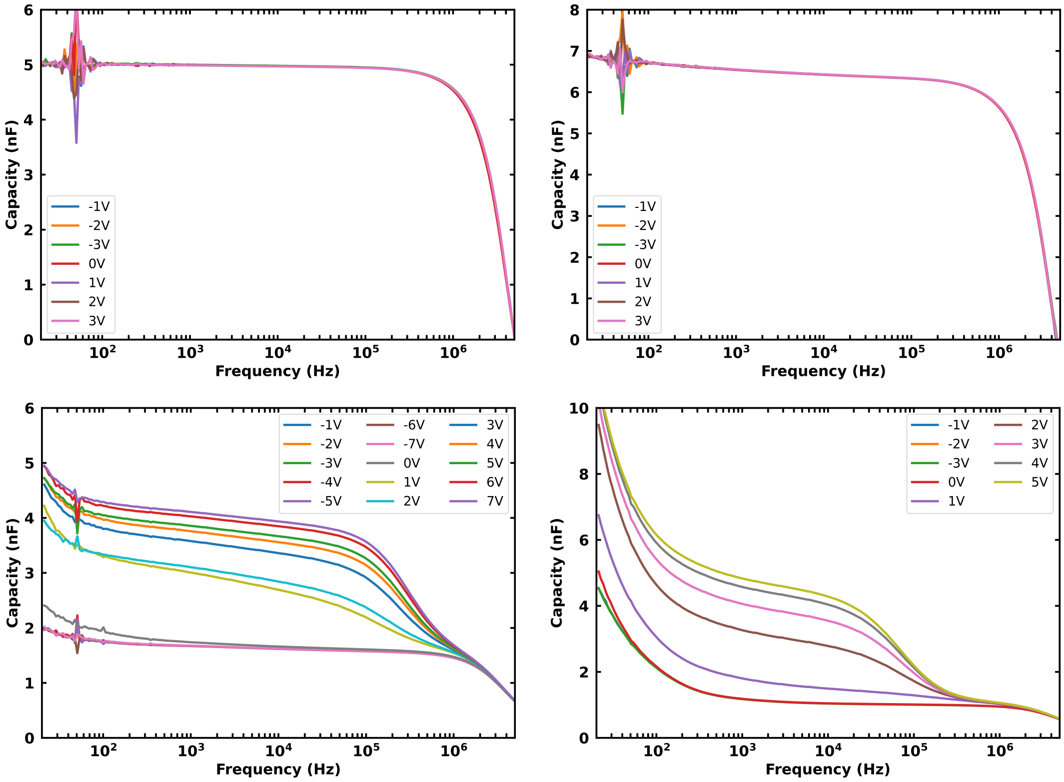

FIGURE 5.1: Evolution of the capacity as a function of the AC frequency for the dielectric layer device and dielectric + electron blocking layer device in the first two charts, right and left respectively. Pristine polymer and blend devices are respectively represented on the bottom left and bottom right charts. Capacity trends is plot for DC applied bias to create a charge carrier depleted and accumulated situation.

follow the AC perturbation anymore. Using the mathematical relation presented in the methodology section, the transition frequency estimated at 2.8*10^5 Hz corresponds to charge carrier mobility values of 3.06*10^{-4} $cm^2V^{-1}s^{-1}$ for a thickness of 53 nm. This value is strongly consistent with reported SCLC results[135]

Y6-12 NFA hole mobility has been tested in similar conditions. The appearing capacitance variation is the tail of a large window transition regime occurring at less than 10 Hz. This could come from several parasitic effects or due to a very low mobility value but the absence of a clear transition at high frequency shows a non significant hole mobility in the NFA neat film.

Finally, blend thin-film hole mobility has also been probed in a 100 nm thickness of PM7:Y6-12 blend. The results seem to combine NFA and polymer isolated capacity response with a first capacity drop at low frequency and a second close to the same value as the pristine polymer thin film but reduced due to the segregation phase. This results in a hole transport dominated by the polymer. This concludes the IS results of this section and can confirm the analysis method pertinence, even if results are missing for the other charge carrier type.

5.3 Charge transport: DFT approach

Even if IS experiments were not conducted on NFA for electron transport, this has been theoretically studied using a DFT method on crystalline structures. This simulation context is obviously far from experimental conditions but still gives useful information on performance trends and comparison between studied active layers used in devices.

Crystallographic data files have been taken from[144,145], shown in fig 5.2. The calculations have been carried with the ADF software using the PBE functional, not including the long range correction because not available at the time of the analysis. The ITIC crystal demonstrates the importance of side-chain steric hindrance because the distance between vertically aligned molecules is too large for electronic interaction, the interaction distance is equal to 8.42 Å. Therefore, the shortest distance between nearest neighbours occurs between end-cap moieties, with roughly 3.75 Å of separation, revealing the charge pathway through the crystal structure.

The fluorinated ITIC crystal structure shows an intercalated molecule between two vertically aligned molecules resulting in a denser structure. This unlocks another directionality in the charge transport, between end-caps and the central core in an ordered structure.

Y6 on the other hand exhibits a more ordered structure, monoclinic against a triclinic for ITIC. Several couples are distinguished by their mutual interactions, combining the benzothiazole core (BT) group and terminal groups (TG). Between dimer molecules, the distance is 3.47 Å while inter dimer distances are equal to 3.53 Å.

- BT-BT
- BT-TG
- Two different TG-TG

The interaction distances and the DFT transfer integrals, represented for ITIC and ITIC-F in fig.A.6 and A.7 in the crystal structure let us predict a one dimension transport for ITIC, 2 dimensions for ITIC-F and a 3D charge transport in the Y6 molecular crystal. DFT calculations have demonstrated strong orbital overlap for such previously reported short distance interactions, confirming the hypothesis of the transport directionality in the NFAs. These information can help us to describe the film morphology to achieve for each NFA. Indeed, NFA with a poor isotropic charge transport in the crystal character should have an amorphous morphology while NFA with more crystalline aggregates should be achieved for NFA showing isotropic charge tran-sport to improve in the charge mobility in OPV devices.

5.4 A-D-A compounds for thermoelectric applications

During the collaboration with Suhao Wang et al.[146], DFT calculations were performed to understand why TIFDMT shows a power factor radically stronger than

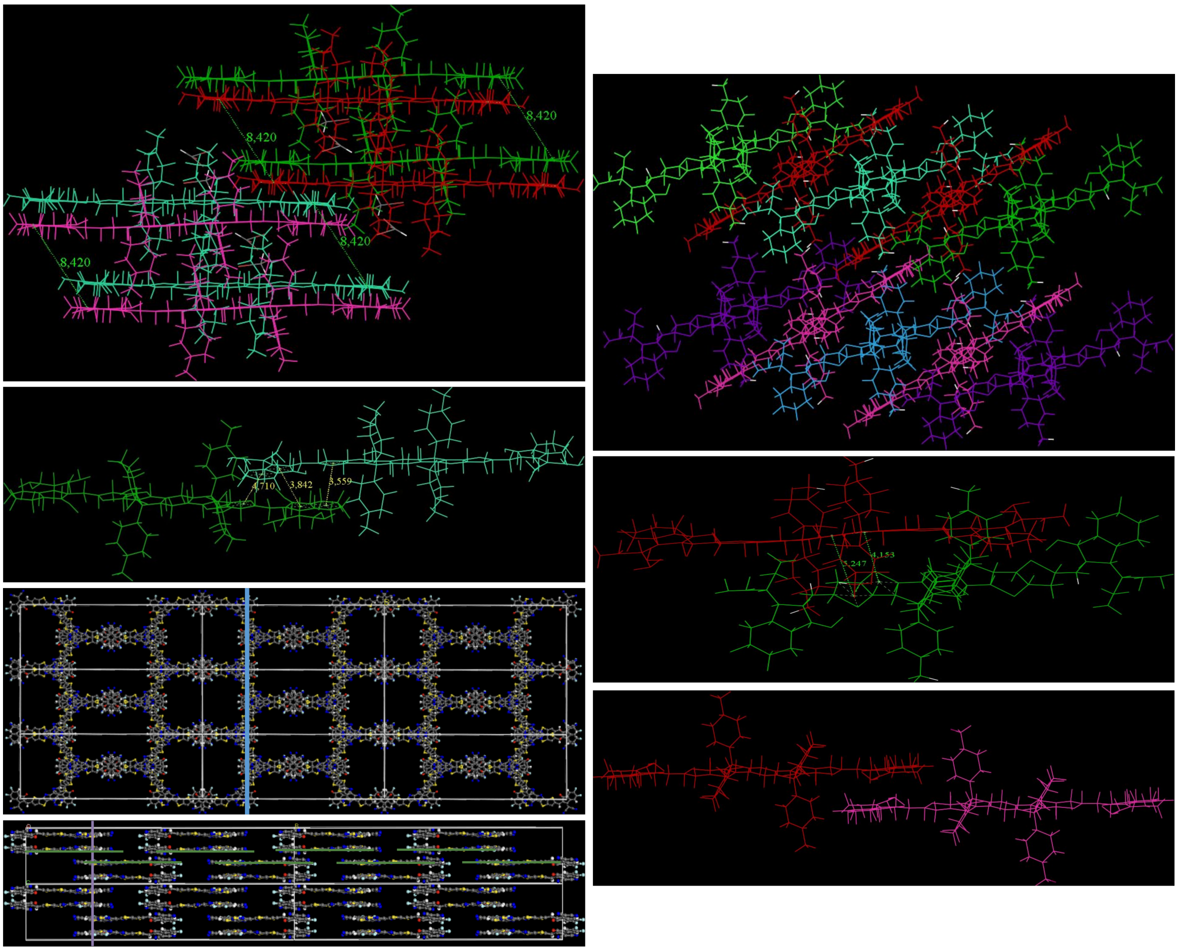

FIGURE 5.2: Crystallographic arrangement of ITIC, ITIC-F and Y6. Left pictures correspond to ITIC and Y6 data, top two pictures for ITIC and bottom two pictures for Y6 while right pictures correspond to ITIC-F.

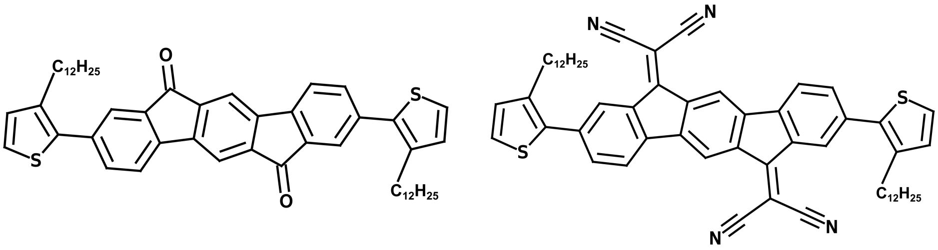

FIGURE 5.3: Molecular structures of TIFDMT, on the left, and TIFDKT, on the right.

the TIFDKT after doping with NDMBI. Both molecules consist in a fused ring backbone with two thiophenes on each side substituted by alkyl chains for good solubility while strong electron withdrawing units are attached to the core (two carbonyls for TIFDKT and two dicyanovynilene units for TIFDMT). These structures, represented in fig. 5.3 can be depicted as donor-acceptor-donor systems, i.e., inverted structures compared to ITIC or BTP systems.

5.4.1 Electronic and optical properties

Their frontier orbital energies have been extracted from CV measurements in dichloromethane; the respective HOMO and LUMO values for TIFDKT are -5.62 eV and -3.60 eV while those of TIFDMT reach -5.65 eV and -4.12 eV. The strong LUMO stabilisation of 0.52 eV is due in part to the dicyanovynilene group that allows for a more extended LUMO than the carbonyl of TIFDKT beside being a stronger acceptor.

Since doping is most of the time required to achieve significant charge conductivity, these two compounds have been doped with the N-DMBI dopant molecule. Pristine film conductivity for both molecules is reported to be on the order of 10^{-6} S cm^{-1}. The TIFDMT conductivity increases by 3 orders of magnitude with 3 mol% of N-DMBI to reach $2.1{*}10^{-3}$ S cm^{-1} and 0.16 S cm^{-1} for a dopant concentration of 20 mol% while the conductivity of TIFDKT remains quasi identical whatever the amount of dopant, as seen in fig.5.4.

DFT calculations firstly shed light on their geometric and electronic properties. Both molecules have a rigid and coplanar π-conjugated core and the thiophene on both sides can easily rotate around the interring bond, giving dihedral angle of about 45°. Alkyl side chains have once again been represented by methyl groups to save computational time. The HOMO is fully delocalised for both molecules, except on the withdrawing moieties. The HOMO of TIFDMT is stabilised by 0.12 eV with respect to TIFDKT, in consistency with CV data. In opposition, the LUMO delocalisation is limited to the indenofluorene core plus substituents. The LUMO energy of TIFDMT is lower by 1.17 eV compared to TIFDKT, in accordance with CV measurements; this explains why TIFDMT is more easily doped than TIFDKT because of its more accessible LUMO. Optical absorption spectra, shown in fig.5.5 were recorded for both systems to compare their properties before and after doping. The presence of a wide peak at high wavelength is characteristic of the formation of polaron in the molecule, meaning that the doping is successful. This polaron signature slightly appears for TIFDMT but not for TIFDKT. The simulated TD-DFT spectra well replicate the experimental features with the main absorption peak appearing in the same energy window, as well as the two sub-gap absorption peaks of doped TIFDMT. TIFDKT does not show any polaronic feature in experiments because N-DMBI is probably not a good dopant for this molecule, as suggested by the calculations.

In neutral systems, each electron is paired with another of opposite spin resulting into a spin sum of zero wherever in space. This is not the case for open-shell anionic systems. Spin density, shown in fig.5.5 has then been computed for both n-doped

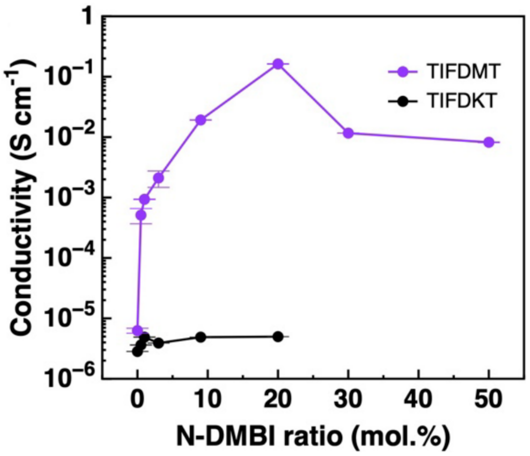

FIGURE 5.4: Evolution of the electrical conductivity in thin films of TIFDKT in black and TIFDMT in purple as a function of doping ratio.

molecules. Coloured atoms support the higher spin density whereas dark zones have all their electrons paired together. The spin density distribution is more delocalised in TIFDMT than TIFDKT. The TIFDKT spin delocalisation is centred on the benzene ring between both carbonyl groups while the TIFDMT spin delocalisation involves more atoms because of the π-electron delocalisation over the dicyanovynilene bridges.

Beside the spin density, Mulliken charges have been computed for on each atom and their values have been subtracted between the anionic and the neutral form to get the partial charges. The Mulliken population analysis allows us to visualise the total electronic density by attributing charges on each atoms and is useful to assess where electron depletion or accumulation occurs. In this section, we report the difference of atomic charges between the neutral and the singly doped molecules to visualise the delocalised position of the charge added upon doping. TIFDKT shows a relatively higher centralisation at the view of the four atoms with high negative values compared to the others and to TIFDMT, resulting in a probably lower charge transfer between molecules in the case of TIFDKT than TIFDMT thin films.

The in-plane π-stacking and the d-spacing from morphology analysis for the doped system suggest an adopted edge-on layer packing for TIFDMT with alkyl chains interdigitated but there is no proof of non intercalation of the dopant in the π-π stacking and rather aggregates on top of the layer. Moreover the polaron delocalisation between neighbouring backbones, suggested through previous DFT calculations, is responsible of attractive forces that decreases the π-π distance, as reported by Yoon S. et al.[147], explaining the better charge transport and enhanced conductivity. At the same time, the non obvious change in the microstructure of TIFDKT before and after doping is primary due to lack of polaron formation despite of the host-dopant miscibility.

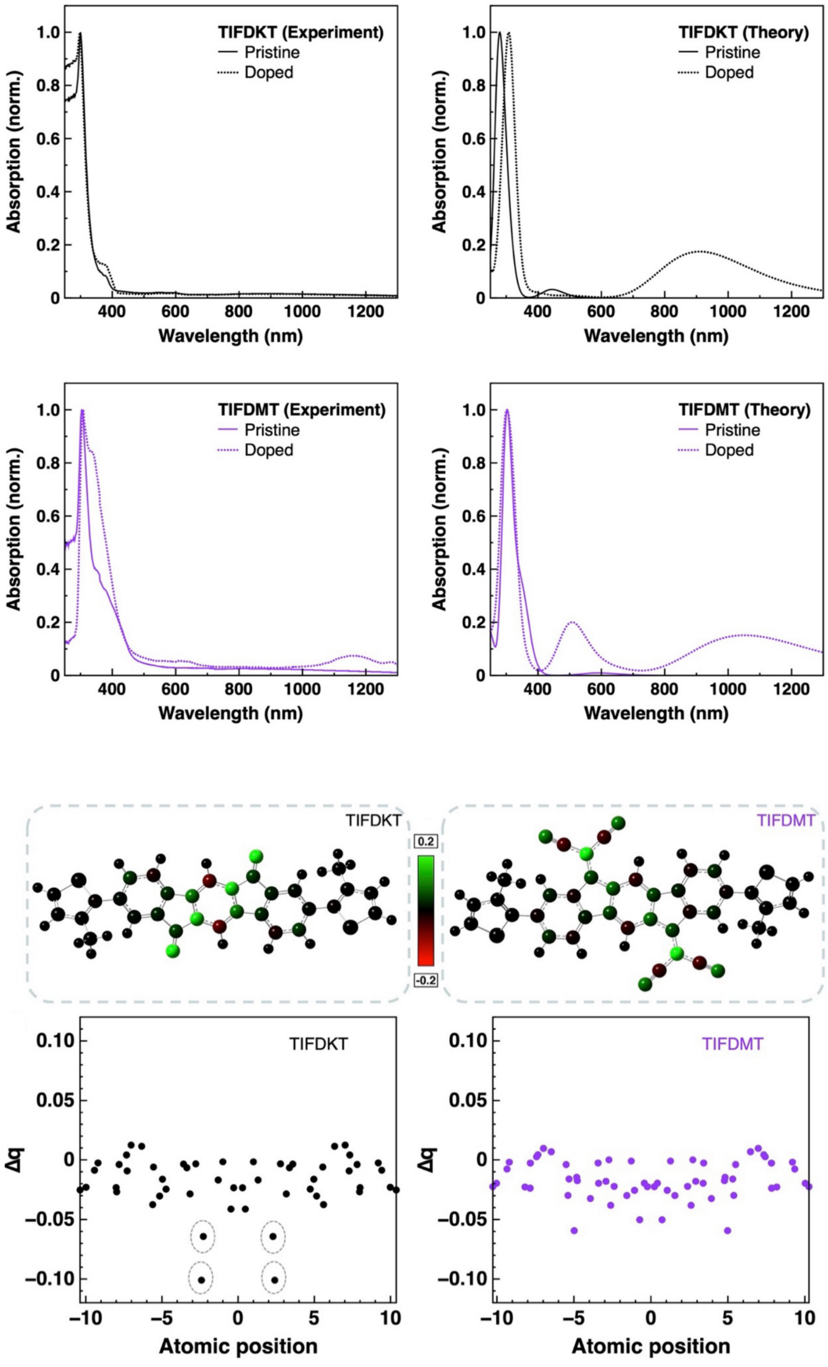

FIGURE 5.5: On the top part, absorption spectra of both TIFDMT and TIFDKT molecules. Experiments are located on the left and TD-DFT simulations on the right. TIFDKT data are represented on the top and TIFDMT on the bottom. Signatures of pristine compounds in solid lines are opposed to those of doped compounds with dashed lines. On the other part, the spin density on the anionic TIFDKT and TIFDMT is represented on top and Mulliken charge distribution at the bottom. Coloured regions represent a high spin or charge density. Graphs represent the charge/spin difference on each atom between the anion and the neutral form as a function of the atomic positions along the molecular backbone.

5.4.2 Thermoelectric characterisation

Thermoelectric performances of the N-DMBI doped TIFDMT compounds, shown in fig.5.6 have been assessed. The Seebeck coefficient (S) is obtained by applying a gradient of temperature while measuring the generated voltage due to the temperature gradient. Measured S values were performed with different doping concentrations. As S is influenced by Fermi level energy differences (E_F) and the charge transport energy (E_T), doping increases the charge carrier density and shift E_F towards E_T and affect S parameter. In fact, S values vary from -355 µV K^{-1} to -123 µV K^{-1} when increasing the dopant concentration from 3 to 20%.

The power factor (PF) rationalises the compromise of electric conductivity and Seebeck coefficient values and can be calculated by $PF = S^2\sigma$ for each dopant concentration. TIFDMT doped by N-DMBI shows then an optimised PF of 0.25 ± 0.006 µ$Wm^{-1}K^{-2}$ at the doping concentration of 20mol%.

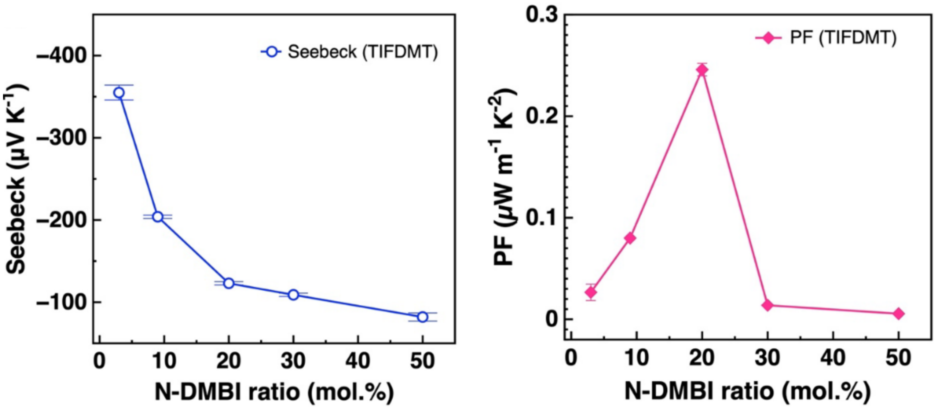

FIGURE 5.6: Charts displaying the evolution of the Seebeck coefficient, on the left, and the power factor, on the right, in function of the dopant molar ratio for TIFDMT thin film.

5.5 Conclusion

This chapter exposed first preliminary results on charge transport study in NFA thin films. A simple method to probe charge carrier mobility by employing the IS technique has been set up and is fully adapted to the OPV field since the charge mobility is probed vertically. The obtained values are not differing far from what have been recorded until now with other methods. Consistent values have been determined for hole transport in polymer thin film but also for a donor acceptor blend, highlighting the modifications occurring while blending both materials compared to the properties of the individual components. Unfortunately, electron mobility for both pristine NFA and blend films have not been recorded due to some technical limitations but are mandatory to complete the analysis method validation.

Moreover, charge transport in the crystal structures of both ITIC and BTP based molecules have been analysed by DFT calculations to give some hints on the potential of these compounds to conduct electricity. We actually focused on the capacity to form charge carrier channels in the 3D structure. Charge migration show a more isotropic character in BTP crystals than ITIC because of the lower steric hindrance that helps to create ordered structures. The more efficient devices obtained with the BTP NFA structure thus partly originates from the larger capability to transfer photo-generated charges between neighbours than ITIC based systems.

Finally, a short section on thermogenerators based on n-doped organic semiconductors having a similar structure as A-D-A ITIC or Y6 NFA concludes this section. This parts reflects the possibility to promote a wider range of applications of ADA or DAD . Comparison between two molecules differentiated by the nature of their electron withdrawing groups, carbonyl versus dicyanovynilene, showed a large difference in doping efficiency. In fact, CV data and DFT results pointed to a much lower LUMO for TIFDMT which is a key parameter to dope molecules, as confirmed through UV-vis experimental and theoretical absorption spectra. Besides, TIFDMT yield a better delocalisation of the added charge, implying that their condensed phase should exhibit a higher electrical conductivity.

Chapter 6

Conclusion and perspectives

This work has shed light on several key properties inherent to A-D-A π-conjugated compounds, namely light absorption, electronic donor acceptor structure, and charge conductivity. Besides their use in solar cells, new possible application in the field of thermoelectricity has been illustrated.

The first chapter discussed in details the electronic structure via DFT calculations plus the light absorption capability in theory but also through experiments in liquid and solid phases. Advantages and drawbacks of widely used NFA molecules, i.e. ITIC and BTP, have been described. Parallelly, the DFT simulation reliability has been confirmed through experimental results and their correlation have explained the outstanding OPV performances due to their geometry and orbital shapes.

Halogenation of these NFA have been studied to assess its impact on the electronic and optical properties. No significant changes have been observed in their electronic structure, except for the stabilisation of all electronic energy levels. Nevertheless, the electronic and optical gap remained unchanged for the molecules in solution. An NTO analysis showed a strong CT character in all NFAs, i.e., a strong feature for an efficient device by weakening the Coulomb interaction between hole and electron and enhancing charge splitting efficiency.

Experimental spectra highlighted their ability to aggregate from the amplitude of the red shift observed between solution and solid-state spectra. This red shift is most probably coming from electrostatic interactions occurring only in condensed phases. Based on their crystal structure, halogenated derivatives tend to compact the ordered structure by activating new interactions involving halogen atoms. In spin-coated thin films, such a structure does not appear and the film is rather amorphous. Nevertheless, these interactions should still occur and should enhance charge mobility across the organic film. Y6 has shown a particularly strong red shift associated to intermolecular interactions that probably arises from the dipole moment related to the molecular half-moon shape.

The blend of donor polymer PM7 with both NFA molecules showed a better association with the Y acceptor family because of the larger spectral coverage compared to the sun emission spectrum. Finally the collaboration with the group of Sébastien

Clément on other D-A systems permitted to study more deeply the push-pull effect occurring in these systems.

They have synthesized other compounds by associating several A moieties to two different D chemical groups. This affects the orbital energies and shapes giving birth to several degrees of CT character in their optical transitions. Moreover, the polymerisation of these systems also affect the frontier orbital delocalisation, thus impacting the CT character of a given compound as a function of its length.

Another interesting part of this work lays in the photo-stability study of NFA, a crucial parameter in the reliability of OPV technology. Light irradiation may trigger isomerisation reactions on ITIC compounds that do not occur with BTP molecules. Indeed, the cycloaddition induced by the isomerisation is prevented for BTP molecules due to the presence of a side-chain on the involved carbon from the thiophene cycle. Another compound is then formed with a blue-shifted absorption signature undoubtedly reducing OPV performances.

Ambient air exposure triggered another degradation pathway under light absorption, which remains not understood at this stage. Attempts have been carried out in this work by combining light absorption, mass spectrometry and DFT techniques to bring more answers to this question. This has evidenced a reaction with oxygen by a successive addition of oxygen atoms on the NFA structure but the attacking location and the kinetic is still in the working progress stage.

The second chapter focused on the morphology analysis of the spin-coated OSCs and the device performances. Several parameters, such as the side-chain length and the nature of halogen on end-cap moieties can trigger strong morphology changes and therefore affect devices performances. In fact, longer side chains will obviously affect the solubility in solvent but also the miscibility with the donor polymers. The importance of the solvent choice has been demonstrated based on its viscosity beside compound solubility. Indeed, more viscous solvents, correlated with its boiling point temperature, will dry more slowly enabling a higher degree of order in the film than a less viscous solvent. Therefore, shorter side-chain NFA should be dissolved in less viscous solvents to prevent too high phase segregation while longer side-chain NFA should be dissolved in viscous solvent to enables more order while keeping a good phase segregation.

End-cap moiety halogenation has also demonstrated a huge impact on the morphology and performances. Based on the conclusions settled about the intermolecular interaction strength between fluorine and chlorine atoms, ITIC-Cl should exhibit less solubility than ITIC-F in the same conditions which is proven through AFM images and by a drastically low current density in OPV devices embedding chlorinated ITIC due to a poor phase segregation and high roughness.

At the end of this chapter, several observations have been made on the device construction approach performed during an internship at the Brilliant Matters company. Besides the molecular parameters and the tailoring of the active layer, the nature of the inter-layer was found to strongly impact the OPV performances, justifying the comparably low performances exhibited in this work with those from the literature. The conception of a fully spin-coatable device has been enabled by the electrode material selection and the solvent orthogonality analysis which has permitted to create a semi-transparent performant device despite the prototypal stage.

In parallel, multiple device structures have been created by mixing the nature of the active layer and inter-layer,demonstrating the importance of inter-layer electrical conductivity or morphology in the performances. Device tailoring can enhance significantly the active layer performances by several precents by modifying solvents, inter-layer compounds, device building technique, and many other parameters which explain the non-optimal results in this manuscript but still relevant for a comparison study.

In the final chapter, preliminary results have been exposed about charge mobility extracted from impedance spectroscopy in NTA thin films, further supplemented by DFT simulations. Impedance spectroscopy for charge mobility probing has the advantage to combine a relatively simple technique with a consistent probing approach exploiting the vertical character of the charge displacement across the OPV device under relatively low applied voltages. Results have been obtained for hole transport for the PM7 polymer, the Y6-12 acceptor and the blend of both. Consistent values have been recorded and a hole transport dominated by the polymer in the blend film has been evidenced; this study needs to be extended to demonstrate its reliability in particular for electron transport.

Crystal structure analysis of NFA compounds has been done theoretically by assessing the potential interaction sites through their intermolecular distance and the orbital overlap between nearest neighbours. From one dimension to three dimensions for the charge transport was theoretically demonstrated successively for ITIC, ITIC-F and Y6 and could partly explain the relative difference in terms of their device performances despite the amorphous character of the active layer if we consider a significant domain phase order in the thin film.

The potential for thermoelectric applications of NFA-like structures was finally illustrated by comparing the performances of two D-A-D like molecules. Doping efficiency of both TIFDMT and TIFDKT molecules have been assessed through a joint theoretical and experimental study. The lower LUMO energy of TIFDMT is a strong advantage for chemical doping while absorption spectra have proved the presence of polarons on the TIFDMT molecules in contrast of TIFDKT. Moreover, DFT calculations have shown that TIFDMT delocalises the supplementary charge more easily than TIFDKT.

To push this work even further, proposals will be described in the following paragraphs. For theoretical simulations, similar works as done with the group of Clément S. could be realised for polymeric systems of ITIC and BTP. Moreover, a molecular dynamic aspect could be introduced to simulate BHJ systems to enhance our knowledge about their molecular arrangement and the impact of any post-treatment usually used in the device fabrication.

Further experimentation could be conducted using absorption spectra to dwell more on the stability in ambient air conditions by still associating mass spectrometry techniques and theoretical experiments. Potential attack sites and the kinetic behind this process could be more precisely described which would definitely help to design more stable compounds.

About the morphology of NFA thin films and blends, other solvent could be tested for the end-cap halogenation study and definitely assess the solubility parameter of halogenated compounds but also to determine a better solvent for chlorinated acceptors. In parallel, the chlorine-fluorine interactions should be analysed in relation to the strong OPV performances. Finally, adding GIWAXS data to already obtained AFM results could be very useful to understand molecular arrangement in the thin films and also describe the power of several post treatment techniques that are often used to enhance the molecular ordering.

Finally, charge carrier mobility deserves more attention to fulfil the study with electron mobility. This could be pushed to the measurements of photo-generated charges under illumination which would bring us even closer to the real charge transport in OPV devices. Moreover, crystal study is very far from the reality. Combination of molecular dynamics and DFT would allow the generation of multiple amorphous structures that could be used to compute transfer integrals by DFT. This will provide us a refine picture of the charge transport directionality in NFAs and also confirm or not the previous observations made from crystallographic structures.

Appendix A

Appendices

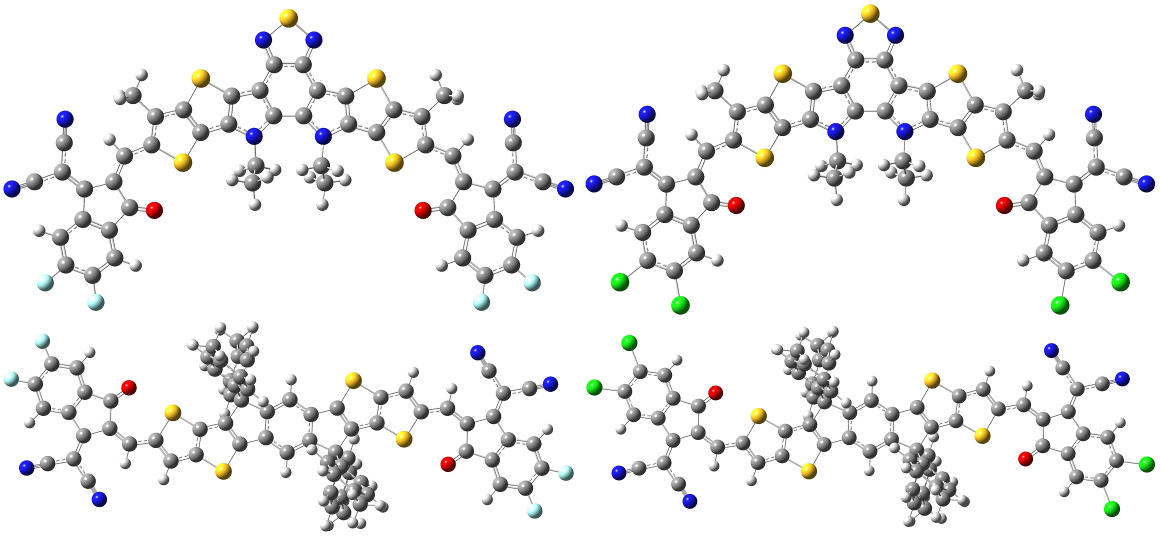

FIGURE A.1: Molecular structure of halogenated ITIC and BTP derivatives. Colour legend is similar to the scheme of ITIC and Y5, adding fluorine in light blue and chlorine in green.

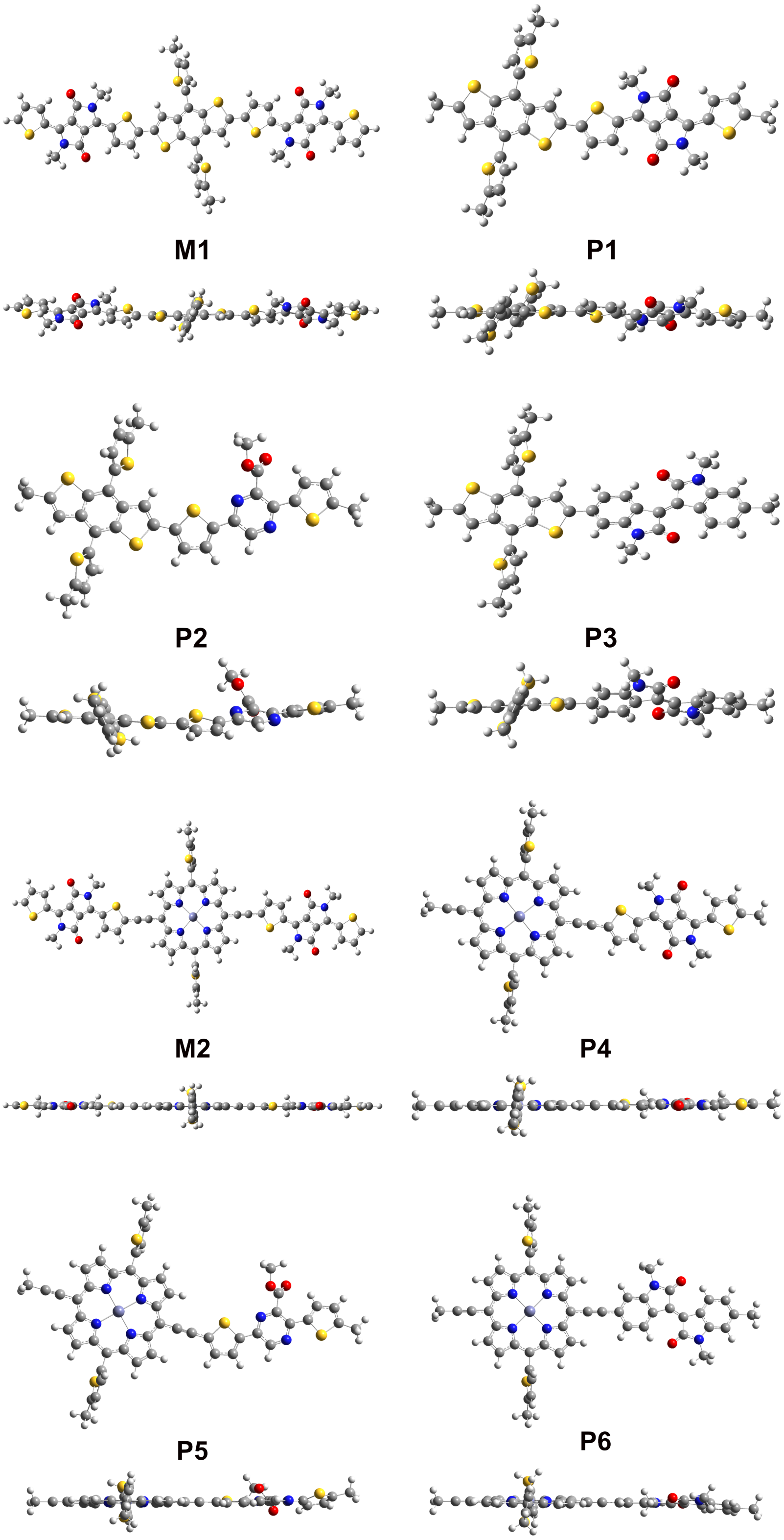

M1 P1 P2 P3 M2 P4 P5 P6

FIGURE A.2: All D-A compounds structures build synthesised by the group of Clément S. from top and side view

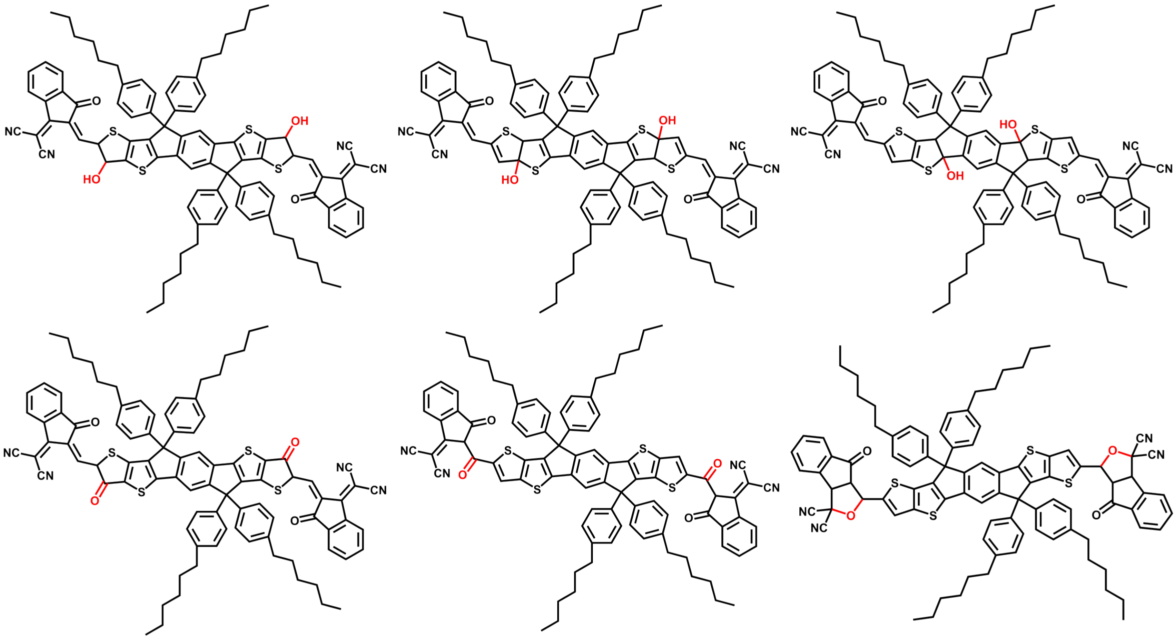

FIGURE A.3: Chemical structures for oxidised ITIC molecules proposed from expirments observation and literature suggestions.

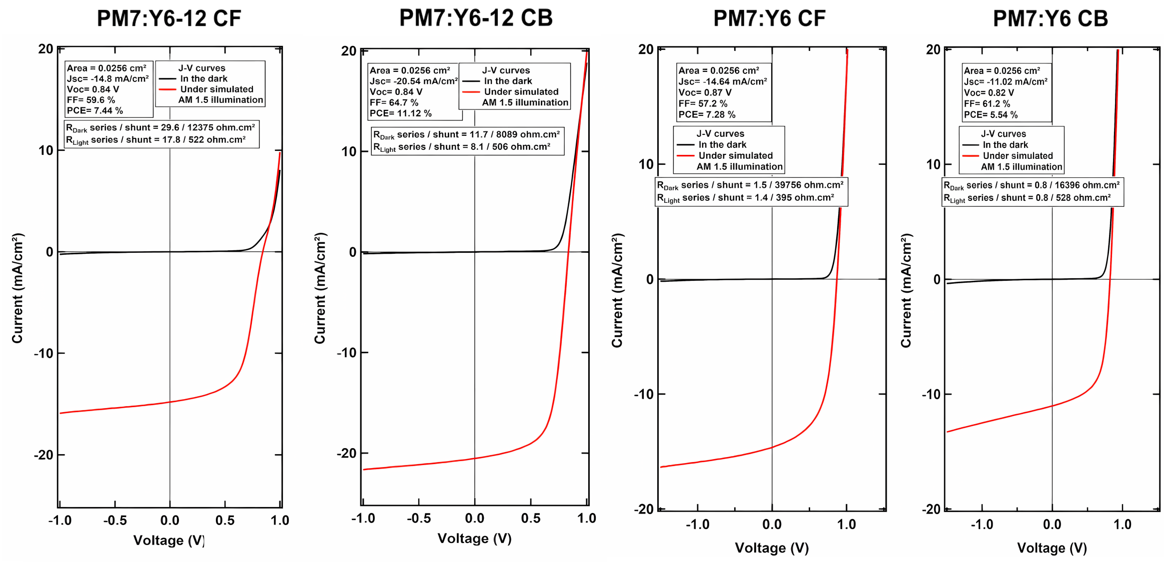

FIGURE A.4: I/V curves of testing devices including PM7:Y6 and PM7:Y6-12 blends as active layer cast from CB and CF solutions

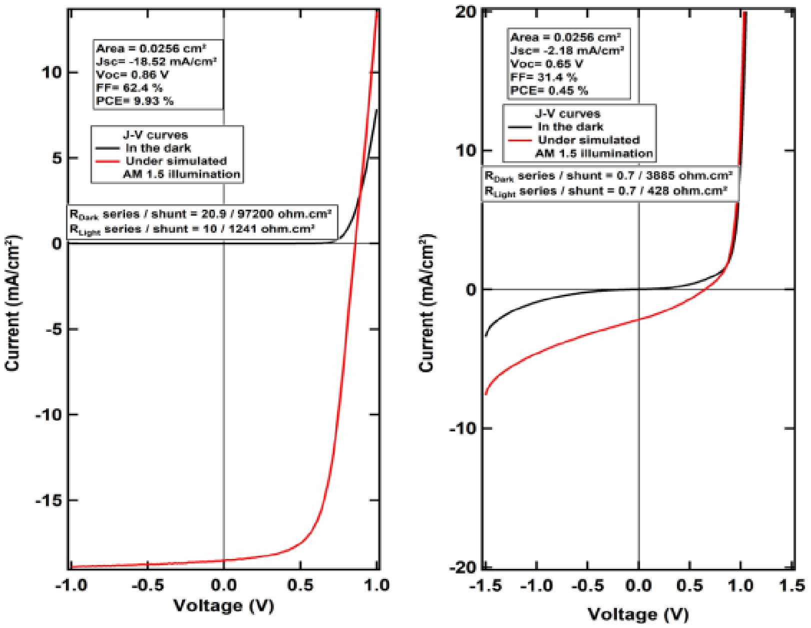

FIGURE A.5: I/V curves of testing devices including PM7:ITIC-F and PM7:ITIC-Cl as active layer cast from CB solution.

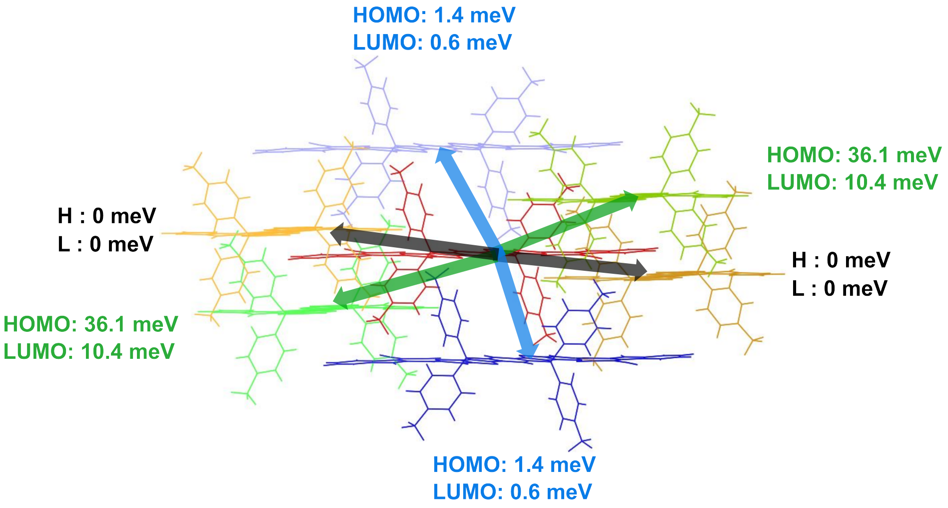

FIGURE A.6: Scheme of charge transport pathway in a ITIC crystalline structure.

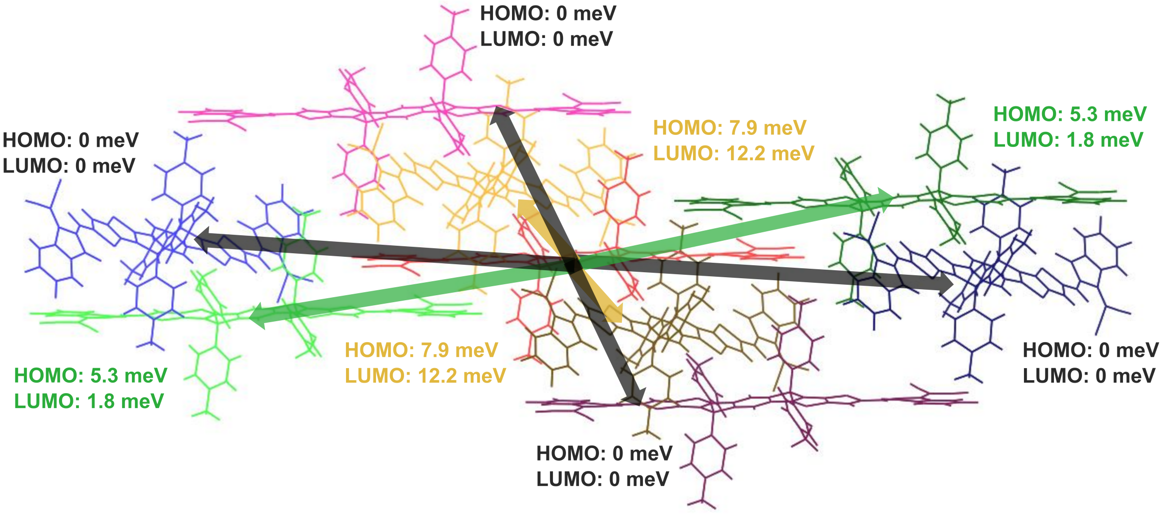

FIGURE A.7: Scheme of charge transport pathway in a ITIC-F crystalline structure.

Bibliography

[1] *Special Eurobarometer 538 Climate Change*. Accessed on April 2024. 2023. URL: `https://europa.eu/eurobarometer/surveys/detail/2954`.

[2] H. Ritchie, P. Rosado, and M. Roser. "CO_2 and Greenhouse Gas Emissions". In: *Our World in Data* (2023).

[3] S. Singh. *The relationship between growth in GDP and CO2 has loosened; it needs to be cut completely*. 2024. URL: `https://www.iea.org/commentaries/the-relationship-between-growth-in-gdp-and-co2-has-loosened-it-needs-to-be-cut-completely`.

[4] H. Ritchie, P. Rosado, and M. Roser. "Per capita, national, historical: how do countries compare on CO2 metrics?" In: *Our World in Data* (2023).

[5] *Données climatique fédérale de belgique*. 2022. URL: `https://climat.be/en-belgique/climat-et-emissions/emissions-des-gaz-a-effet-de-serre`.

[6] H. Belin. "How 200 years of industry shaped Belgium's identity". In: *The Brussels Times* (2018).

[7] H. Lee et al. *Climate Change 2023: Synthesis Report, Summary for Policymakers. Contribution of Working Groups I, II and III to the Sixth Assessment Report of the Intergovernmental Panel on Climate Change*. Tech. rep. Intergovernmental Panel on Climate Change (IPCC), 2023.

[8] D. H. Meadows et al. *The limit to growth*. Potomac Associates – Universe Books, 1972.

[9] M. Ferrer. "La décroissance : d'où vient ce concept politique et philoso-phique?" In: *Le Monde* (2021).

[10] *Les énergies renouvelables : qu'est-ce que c'est ?* URL: `https://www.un.org/fr/climatechange/what-is-renewable-energy`.

[11] S. Schlomer et al. *Climate Change 2014: Mitigation of Climate Change. Contribution of Working Group III to the Fifth Assessment Report of the Intergovernmental Panel on Climate Change: Annex III: Technology-specific cost and performance parameters*. Tech. rep. Cambridge University Press, Cambridge, United Kingdom and Ne York, NY, USA, 2014.

[12] T. D. de Wit et al. "Methodology to create a new Total Solar Irradiance record: Making a composite out of multiple data records". In: *Geophys. Res. Lett.* 44 (2017), pp. 1196–1203.

[13] P. Gadonneix et al. *World Energy Resources*. World Energy Council, 2013.

[14] *Global Energy Review 2019*. Tech. rep. IEA, 2020. URL: `https://www.iea.org/reports/global-energy-review-2019`.

[15] URL: `https://www.nrel.gov/pv/research.html`.

[16] G. Bilicic and S. Scroggins. *Lazard's Levelized Cost of Energy*. Tech. rep. Lazard, 2023.

[17] M. Taylor, P. Ralon, and S. Al-Zoghoul. *Renewable power generation: costs in 2021*. Tech. rep. International Renewable Energy Agency, 2022.

[18] E. Walker and . Brown. *Best solar panels in 2024: Which one should you choose?* 2024. URL: `https://www.energysage.com/solar/best-solar-panels-complete-ranking/`.

[19] M.J. (Mariska) de Wild-Scholten. “Energy payback time and carbon footprint of commercial photovoltaic systems”. In: *Solar Energy Materials and Solar Cells* 119 (2013), pp. 296–305.

[20] P. Tsang Michael, W. Sonnemann Guido, and M. Bassani Dario. “A comparative human health, ecotoxicity, and product environmental assessment on the production of organic and silicon solar cells”. In: *Progress in Photovoltaics: Research and Applications* 24.5 (2016), pp. 645–655.

[21] *Energy and Carbon Payback Times for Modern U.S. Utility Photovoltaic Systems*. Tech. rep. NREL, 2024.

[22] H. Hertz. “Ueber einen Einfluss des ultravioletten Lichtes auf die electrische Entladung”. In: *Annalen der Physik* 267.8 (1887), pp. 983–1000.

[23] D. Lincot. “Lumière du ciel, énergie de la Terre. La conversion photovoltaïque au service des hommes”. In: *Raison présente* 4.196 (2015), pp. 27–37.

[24] P. W. Atkins and R. S. Friedman. *Molecular Quantum Mechanics*. Oxford University Press, 2005.

[25] A.V. Shah, R. Platz, and H. Keppner. “Thin-film silicon solar cells: A review and selected trends”. In: *Solar Energy Materials and Solar Cells* 38.1 (1995), pp. 501–520.

[26] C. Kittel. *introduction to solid state physics*. 8th ed. Wiley, 2005.

[27] T. A. Skotheim and J. Reynolds. *Conjugated Polymers: Theory, Synthesis, Properties, and Characterization*. 3rd ed. Handbook of Conducting Polymers, Third Edition. CRC Press, 2006.

[28] F. A. Carey and R. J. Sundberg. *Advanced Organic Chemistry*. Springer, 2000.

[29] T. Kazuo, O. Itaru, and N. Masahiro. “Pi-Building Blocks for Organic Electronics: Revaluation of “Inductive” and “Resonance” Effects of pi-Electron Deficient Units”. In: *Chemistry of Materials* 26.1 (2014), pp. 587–593.

[30] W. D. Callister Jr. and D. G. Rethwisch. *Materials Science and Engineering: An Introduction, Eighth Edition*. 8th ed. Wiley and Sons, 2010.

[31] Carol J. Riordan and R. Hulstron. “What is an air mass 1.5 spectrum? (solar cell performance calculations)”. In: *IEEE Conference on Photovoltaic Specialists* (1990), 1085–1088 vol.2.

[32] L. B.R. Puri, L.R. Sharma, and M. S. Pathania. *Principles of Physical Chemistry*. Vishal Publishing Co., 1962.

[33] G.E. Jellison and F. A. Modine. “Optical absorption of silicon between 1.6 and 4.7 eV at elevated temperatures”. In: *Applied Physics Letters* 41.2 (July 1982), pp. 180–182.

[34] M.A. Green and M.J. Keevers. "Optical properties of intrinsic silicon at 300 K". In: *Progress in Photovoltaics Research and Applications* 3.3 (1995), pp. 189–192.

[35] Wei Wang et al. "Enhancing Transition Dipole Moments of Heterocyclic Semiconductors via Rational Nitrogen-Substitution for Sensitive Near Infrared Detection". In: *Advanced Materials* 34.28 (2022).

[36] M. Knupfer. "Exciton binding energies in organic semiconductors". In: *Applied physics A* 77.5 (2003), pp. 623–626.

[37] B. M. Savoie et al. "Mesoscopic Features of Charge Generation in Organic Semiconductors". In: *Accounts of chemical research* 47.11 (2014), pp. 3385–3394.

[38] J. Maier. "Doping Strategies in Inorganic and Organic Materials". In: *Zeitschrift für anorganische und allgemeine Chemie* 643.23 (2017), pp. 2083–2087.

[39] S.C. Jain, E.L. Heasell, and D.J. Roulston. "Recent advances in the physics of silicon P-N junction solar cells including their transient response". In: *Progress in Quantum Electronics* 11.2 (1987), pp. 105–204.

[40] Yun-Ju Lee et al. "Comparison of conventional and inverted organic photovoltaic devices with controlled illumination area and extraction layers". In: *Solar Energy Materials and Solar Cells* 144 (2016), pp. 592–599.

[41] D.W. Zhao et al. "Optimization of an inverted organic solar cell". In: *Solar Energy Materials and Solar Cells* 94.6 (2010), pp. 985–991.

[42] G. Yu et al. "Polymer Photovoltaic Cells: Enhanced Efficiencies via a Network of Internal Donor-Acceptor Heterojunctions". In: *Science* 270.5243 (1995), 1789–1791.

[43] J.H. Park et al. "Roles of Interlayers in Efficient Organic Photovoltaic Devices". In: *Macromolecular Rapid Communications* 31.24 (2010), pp. 2-095–2108.

[44] S. Huang et al. "Solution-processed SnO2 nanoparticle interfacial layers for efficient electron transport in ZnO-based polymer solar cells". In: *Organic Electronics* 62 (2018), pp. 373–381.

[45] S.A. Abubaker and M.Z. Pakhuruddin. "An Overview of Electron Transport Layer Materials and Structures for Efficient Organic Photovoltaic Cells". In: *Energy Technology* (June 2024).

[46] C.G. Granqvist and A. Hultåker. "Transparent and conducting ITO films: new developments and applications". In: *Thin Solid Films* 411.1 (2002), pp. 1–5.

[47] Hyesung Park et al. "Graphene As Transparent Conducting Electrodes in Organic Photovoltaics: Studies in Graphene Morphology, Hole Transporting Layers, and Counter Electrodes". In: *Nano Letters* 12.1 (2011), pp. 133–140.

[48] A.J. Heeger. "25th Anniversary Article: Bulk Heterojunction Solar Cells: Understanding the Mechanism of Operation". In: *Advanced Materials* 26.1 (2013), pp. 10–28.

[49] Letian Dou et al. "25th Anniversary Article: A Decade of Organic/ Polymeric Photovoltaic Research". In: *Advanced Materials* 25.46 (2013), pp. 6642–6671.

[50] B. Ehrler et al. "Photovoltaics Reaching for the Shockley–Queisser Limit". In: *ACS Energy Letters* 5.9 (2020), pp. 3029–3033.

[51] William Shockley and Hans J. Queisser. "Detailed Balance Limit of Efficiency of p-n Junction Solar Cells". In: *Journal of Applied Physics* 32.3 (1961), pp. 510–519.

[52] Marisol Reyes-Reyes, Kyungkon Kim, and David L. Carroll. "High-efficiency photovoltaic devices based on annealed poly(3-hexylthiop-hene) and 1-(3-methoxycarbonyl)-propyl-1- phenyl-(6,6)C61 blends". In: *Applied Physics Letters* 87.8 (2005).

[53] Ying Wang et al. "Photo-dimerization kinetics in solid C60 films". In: *Chemical Physics Letters* 211.4-5 (1993), pp. 341–345.

[54] Ping Zhou et al. "Reaction mechanism for the photopolymerization of solid fullerene C60". In: *Chemical Physics Letters* 211.4-5 (Aug. 1993), pp. 337–340.

[55] Christoph J. Brabec et al. "Origin of the Open Circuit Voltage of Plastic Solar Cells". In: *Advanced Functional Materials* (2001).

[56] Sih-Hao Liao et al. "Fullerene Derivative-Doped Zinc Oxide Nanofilm as the Cathode of Inverted Polymer Solar Cells with Low-Bandgap Polymer (PTB7-Th) for High Performance". In: *Advanced Materials* 25 (2013), pp. 4766–4771.

[57] Zhicai He et al. "Enhanced power-conversion efficiency in polymer solar cells using an inverted device structure". In: *Nature Photonics* 6.9 (2012), 591–595.

[58] Long Ye et al. "Highly Efficient 2D-Conjugated Benzodithiophene-Based Photovoltaic Polymer with Linear Alkylthio Side Chain". In: *Chemistry of Materials* 26.12 (2014), pp. 3603–3605.

[59] Guangchao Han et al. "Terminal pi–pi stacking determines three dimensional molecular packing and isotropic charge transport in an A–pi–A electron acceptor for non-fullerene organic solar cells". In: *Journal of Materials Chemistry C* 5.20 (2017), pp. 4852–4857.

[60] Yuze Lin et al. "An Electron Acceptor Challenging Fullerenes for Efficient Polymer Solar Cells". In: *Advanced Materials* 27.7 (2015), pp. 1170–1174.

[61] Y. Yankang et al. "Side-Chain Isomerization on an n-type Organic Semiconductor ITIC Acceptor Makes 11.77% High Efficiency Polymer Solar Cells". In: *Journal of the American Chemical Society* 138.45 (2016), pp. 15011–15018.

[62] M. Muzammil et al. "Boosting the performance of PBDB-T:ITIC based organic solar cell: A theoretical analysis utilizing SCAPS-1D". In: *Chemical Physics Impact* 8 (2024), p. 100407.

[63] B. Zheng, L. Huo, and Y. Li. "Benzodithiophenedione-based polymers: recent advances in organic photovoltaics". In: *NPG Asia Materials* 12.1 (2020).

[64] F. Regnier et al. "The impact of side chain elongation from the Y6 to Y6-12 acceptor in organic solar cells: a fundamental study from molecules to devices". In: *Journal of Materials Chemistry C* 11.22 (2023), pp. 7451–7461.

[65] Ping Li et al. "Rigid fused pi-spacers in D–pi–A type molecules for dye-sensitized solar cells: a computational investigation". In: *Journal of Materials Chemistry C* 5.44 (2017), pp. 11454–11465.

[66] Yong Zhang et al. "Conjugated polymers based on C, Si and N-bridged dithiophene and thienopyrroledione units: synthesis, field-effect transistors and

bulk heterojunction polymer solar cells". In: *Journal of Materials Chemistry* 21.11 (2011), p. 3895.

[67] *Best Research-Cell Efficiency Chart*. Tech. rep. National Renewable Energy Laboratory, 2024.

[68] T. J. Seebeck. "Ueber die magnetische Polarisation der Metalle und Erze durch Temperaturdifferenz". In: *Annalen der Physik* 82.3 (Jan. 1826), pp. 253–286.

[69] LI Anatychuk. "On the discovery of thermoelectricity by Volta". In: *Journal of thermoelectricity* 2 (2004), pp. 5–10.

[70] Alessandro Volta. *Le opere di Alessandro Volta: Edizione nazionale sotto gli auspici della Reale Accademia dei Lincei i del Reale Istituto lombardo di scienze e lettere*. Vol. 5. Hoepli, 1928.

[71] G Pastorino. "Alessandro Volta and his role in thermoelectricity". In: *Journal of Thermoelectricity* 1 (2009), pp. 7–10.

[72] J Fourier and H Oersted. "Sur quelques nouvelles experiences thermoelectriques". In: *Ann. Chim. Phys* 24 (1823), pp. 375–380.

[73] Peter Mark Roget. *Treatises on electricity, galvanism, magnetism, and electromagnetism*. Baldwin and Cradock, 1832.

[74] Lord Rayleigh. "XLIII. On the thermodynamic efficiency of the thermopile". In: *The London Edinburgh and Dublin Philosophical Magazine and Journal of Science* 20.125 (Oct. 1885), pp. 361–363.

[75] Alexandre Polozine, Susanna Sirotinskaya, and Lírio Schaeffer. "History of development of thermoelectric materials for electric power generation and criteria of their quality". In: *Materials Research* 17 (2014), pp. 1260–1267.

[76] Maria Telkes. "The Efficiency of Thermoelectric Generators. I." In: *Journal of Applied Physics* 18.12 (1947), pp. 1116–1127.

[77] David Michael Rowe. *CRC handbook of thermoelectrics*. CRC press, 2018.

[78] George R Schmidt, Thomas J Sutliff, and LA Dudzinksi. "Radioisotope power: A key technology for deep space exploration". In: *Radioisotopes Applications in Physical Sciences* (2008), pp. 419–456.

[79] Victor Parsonnet, Alan D. Berstein, and Gershon Y. Perry. "The nuclear pacemaker: Is renewed interest warranted?" In: *The American Journal of Cardiology* 66.10 (Oct. 1990), pp. 837–842.

[80] L. D. Hicks and M. S. Dresselhaus. "Use of Quantum-Well Superlattices to Obtain a High Figure of Merit from Nonconventional Thermoelectric Materials". In: *MRS Proceedings* 326 (Jan. 1993).

[81] L. D. Hicks and M. S. Dresselhaus. "Effect of quantum-well structures on the thermoelectric figure of merit". In: *Physical review. B, Condensed matter* 47.19 (May 1993), pp. 12727–12731.

[82] C. Forman et al. "Estimating the global waste heat potential". In: *Renewable and Sustainable Energy Reviews* 57 (Jan. 2016), pp. 1568–1579.

[83] Edmund Altenkirch. "über den nutzeffekt der thermosäule Phys". In: *Zeitschrift* 16 (1909), p. 560.

[84] Edmund Altenkirch. "Elektrothermische Kälteerzeugung und reversible elektrische Heizung". In: *Physikalische Zeitschrift* 12 (1911), pp. 920–924.

[85] Julian W Gardner and Florin Udrea. *Microsensors: principles and applications*. John Wiley & Sons, Inc., 2009.

[86] G Jeffrey Snyder and Eric S Toberer. "Complex thermoelectric materials". In: *Nature materials* 7.2 (2008), pp. 105–114.

[87] Dinesh K Aswal, Ranita Basu, and Ajay Singh. "Key issues in development of thermoelectric power generators: High figure-of-merit materials and their highly conducting interfaces with metallic interconnects". In: *Energy conversion and management* 114 (2016), pp. 50–67.

[88] H. Julian Goldsmid. *Chapter 1 Introduction*. Jan. 2001, pp. 1–24.

[89] M. A. Zoui et al. "A Review on Thermoelectric Generators: Progress and Applications". In: *Energies* 13.14 (2020), p. 3606.

[90] Jiabing Yu, Qiang Sun, and Puru Jena. "Recent advances in 2D thermoelectric materials". In: *Proceedings of SPIE, the International Society for Optical Engineering/Proceedings of SPIE* (Dec. 2016).

[91] Boris Russ et al. "Organic thermoelectric materials for energy harvesting and temperature control". In: *Nature Reviews Materials* 1.10 (Aug. 2016).

[92] David Michael Rowe and G. Slack. *CRC handbook of thermoelectrics*. CRC press, 2018.

[93] Suhao Wang et al. "Progress of conjugated polymers as emerging thermoelectric materials". In: *Progress in Polymer Science* 129 (2022), p. 101548.

[94] Zhi-Ping Fan et al. "Enhancing the Thermal Stability of Organic Field-Effect Transistors by Electrostatically Interlocked 2D Molecular Packing". In: *Chemistry of Materials* 30.11 (2018), pp. 3638–3642.

[95] Akash Nigam et al. "Insight into the charge transport and degradation mechanisms in organic transistors operating at elevated temperatures in air". In: *Organic Electronics* 22 (2015), pp. 202–209.

[96] Wenrui Zhao et al. "Chemical doping of organic semiconductors for thermoelectric applications". In: *Chemical Society Reviews* 49.20 (2020), pp. 7210–7228.

[97] Dongyang Wang et al. "Multi-heterojunctioned plastics with high thermoelectric figure of merit". In: *Nature* 632.8025 (2024), pp. 528–535.

[98] F. Rissner et al. "Understanding the Electronic Structure of Metal/SAM/Organic-Semiconductor Heterojunctions". In: *ACS Nano* 3.11 (2009), pp. 3513–3520.

[99] Kai Liu et al. "n-Type thermoelectric elastomers". In: *Nature* (2025), pp. 1–7.

[100] Yong Du et al. "Flexible thermoelectric materials and devices". In: *Applied Materials Today* 12 (2018), pp. 366–388.

[101] Naoki Toshima. "Recent progress of organic and hybrid thermoelectric materials". In: *Synthetic Metals* 225 (2017), pp. 3–21.

[102] Guillaume Schweicher et al. "Molecular Semiconductors for Logic Operations: Dead-End or Bright Future?" In: *Advanced Materials* 32.10 (2020).

[103] Deepak Venkateshvaran et al. "Approaching disorder-free transport in high-mobility conjugated polymers". In: *Nature* 515.7527 (2014), pp. 384–388.

[104] Xinyu Wang et al. "Thermal transport in organic semiconductors". In: *Journal of Applied Physics* 130.17 (2021).

[105] Pablo Díaz-Chao et al. “Precise measurement of the performance of thermoelectric modules”. In: *Measurement Science and Technology* 27.8 (2016), p. 085002.

[106] Ekaterina Selezneva et al. “Review of the Methods for Thermal Conductivity Measurements Most Appropriate for Thermoelectric Materials”. In: *Thermoelectric Materials and Devices*. The Royal Society of Chemistry, 2016. ISBN: 978-1-78262-323-6.

[107] Hsin Wang et al. “Transport Properties of Bulk Thermoelectrics—An International Round-Robin Study, Part I: Seebeck Coefficient and Electrical Resistivity”. In: *Journal of Electronic Materials* 42.4 (2013), pp. 654–664.

[108] Alexandre Vercouter. “Using Computational Methods to Describe Heat Transport Properties in Organic Materials: A Promising Route Towards Thermoelectric Applications”. PhD thesis. University of Mons, 2023.

[109] Xinyu Wang et al. “Molecular dynamics study of thermal transport in a dinaphtho[2,3-b:2′,3′-f]thieno[3,2-b]thiophene (DNTT) organic semiconductor”. In: *Nanoscale* 9.6 (2017), pp. 2262–2271.

[110] Joan Ràfols-Ribé et al. “Evidence of thermal transport anisotropy in stable glasses of vapor deposited organic molecules”. In: *Physical Review Materials* 2.3 (2018).

[111] Dong Wang et al. “Anisotropic Thermal Transport in Organic Molecular Crystals from Nonequilibrium Molecular Dynamics Simulations”. In: *The Journal of Physical Chemistry C* 115.13 (2011), pp. 5940–5946.

[112] Jeong Yun Kim and Jeffrey C. Grossman. “Optimization of the Thermoelectric Figure of Merit in Crystalline C60 with Intercalation Chemistry”. In: *Nano Letters* 16.7 (2016), pp. 4203–4209.

[113] Xiaojia Wang et al. “Ultralow thermal conductivity of fullerene derivatives”. In: *Physical Review B* 88.7 (2013).

[114] M. J. Frisch et al. *Gaussian~16 Revision C.01*. Gaussian Inc. Wallingford CT. 2016.

[115] Roy Dennington, Todd A. Keith, and John M. Millam. *GaussView Version 6*. Semichem Inc. Shawnee Mission KS. 2019.

[116] Evert Jan Baerends et al. “The Amsterdam Modeling Suite”. In: *The Journal of Chemical Physics* 162.16 (2025), p. 162501.

[117] Aidan P. Thompson et al. “LAMMPS - a flexible simulation tool for particle-based materials modeling at the atomic, meso, and continuum scales”. In: *Computer Physics Communications* 271 (Sept. 2021), p. 108171.

[118] Miguel A.L. Marques et al. *Fundamentals of Time-Dependent Density Functional Theory*. Springer Berlin, Heidelberg, Jan. 2012.

[119] Carsten A Ullrich. *Time-dependent density-functional theory: concepts and applications*. OUP Oxford, 2011.

[120] Carsten A. Ullrich and Zeng-Hui Yang. “A Brief Compendium of Time-Dependent Density Functional Theory”. In: *Brazilian Journal of Physics* 44.1 (2013), pp. 154–188.

[121] Jia Hu et al. “Effects of ZnO fabricating process on the performance of inverted organic solar cells”. In: *Organic Electronics* 13.7 (2012), pp. 11-71–1177.

[122] F.J. Zhang et al. “Inverted small molecule organic solar cells with Ca modified ITO as cathode and MoO3 modified Ag as anode”. In: *Solar Energy Materials and Solar Cells* 94.12 (2010), pp. 2416–2421.

[123] Wanxin Sun. “Principles of Atomic Force Microscopy”. In: *Atomic Force Microscopy in Molecular and Cell Biology*. Ed. by Jiye Cai. Singapore: Springer Singapore, 2018, pp. 1–28.

[124] Evgenij Barsoukov and J. Ross Macdonald. *Impedance spectroscopy*. John Wiley & Sons, Mar. 2018.

[125] Jun Yuan et al. “Fused benzothiadiazole: a building block for n-type organic acceptor to achieve high-performance organic solar cells”. In: *Advanced materials* 31.17 (2019), p. 1807577.

[126] Jiarong Luo et al. “Highly sensitive photoelectrochemical sensing platform based on PM6: Y6 pn heterojunction for detection of MCF-7 cells”. In: *Sensors and Actuators B: Chemical* 363 (2022), p. 131814.

[127] Yuqing Li et al. “Structural cutting of non-fullerene acceptors by chlorination: effects of substituent number on device performance”. In: *ACS Applied Materials & Interfaces* 12.45 (2020), pp. 50541–50549.

[128] Hao Zhang et al. “Over 14% Efficiency in Organic Solar Cells Enabled by Chlorinated Nonfullerene Small-Molecule Acceptors”. In: *Advanced Materials* 30.28 (2018).

[129] Dan Deng et al. “Fluorination-enabled optimal morphology leads to over 11% efficiency for inverted small-molecule organic solar cells”. In: *Nature Communications* 7.1 (2016).

[130] Hanjian Lai and Feng He. “Crystal engineering in organic photovoltaic acceptors: a 3D network approach”. In: *Advanced Energy Materials* 10.47 (2020), p. 2002678.

[131] Paul F. Barbara et al. “Single-Molecule Spectroscopy of Conjugated Polymers”. In: *Accounts of Chemical Research* 38.7 (2005), pp. 602–610.

[132] Y. A. Quiroz Avalos et al. “Insights into the relationship between molecular and order-dependent photostability of ITIC derivatives for the production of photochemically stable blends”. In: *Journal of Materials Chemistry C* 12.11 (2024), pp. 4130–4141.

[133] Sungmin Park and Hae Jung Son. “Intrinsic photo-degradation and mechanism of polymer solar cells: the crucial role of non-fullerene acceptors”. In: *Journal of Materials Chemistry A* 7.45 (2019), pp. 25830–25837.

[134] Jing Guo et al. “Suppressing photo-oxidation of non-fullerene acceptors and their blends in organic solar cells by exploring material design and employing friendly stabilizers”. In: *Journal of Materials Chemistry A* 7.43 (2019), 25088–25101.

[135] Shaoqing Zhang et al. “Over 14% efficiency in polymer solar cells enabled by a chlorinated polymer donor”. In: *Advanced Materials* 30.20 (2018), p. 1800868.

[136] Lijiao Ma et al. “A ternary organic solar cell with 300 nm thick active layer shows over 14% efficiency”. In: *Science China Chemistry* 63 (2020), pp. 21–27.

[137] Ling Hong et al. “Eco-compatible solvent-processed organic photovoltaic cells with over 16% efficiency”. In: *Advanced materials* 31.39 (2019), p. 1903441.

[138] Yong Cui et al. “Over 16% efficiency organic photovoltaic cells enabled by a chlorinated acceptor with increased open-circuit voltages”. In: *Nature communications* 10.1 (2019), p. 2515.

[139] Boyuan Qi and Jizheng Wang. “Fill factor in organic solar cells”. In: *Physical Chemistry Chemical Physics* 15.23 (2013), pp. 8972–8982.

[140] Huangzhong Yu, Xinxin Huang, and Chengwen Huang. “PEIE doped ZnO as a tunable cathode interlayer for efficient polymer solar cells”. In: *Applied Surface Science* 470 (2018), pp. 318–330.

[141] Yuxin Xia, Xiaofeng Xu, and Olle Inganäs. “Photovoltage loss in semi-transparent organic photovoltaic devices”. In: *Organic Electronics* 74 (2019), pp. 37–40.

[142] Thanh Luan Nguyen et al. “Semi-crystalline photovoltaic polymers with efficiency exceeding 9% in a 300 nm thick conventional single-cell device”. In: *Energy & Environmental Science* 7.9 (2014), pp. 3040–3051.

[143] Sungmin Park et al. “Progress in materials, solution processes, and long-term stability for large-area organic photovoltaics”. In: *Advanced Materials* 32.51 (2020), p. 2002217.

[144] Thomas J Aldrich et al. “Fluorination effects on indacenodithienothiophene acceptor packing and electronic structure, end-group redistribution, and solar cell photovoltaic response”. In: *Journal of the American Chemical Society* 141.7 (2019), pp. 3274–3287.

[145] Francis Lin et al. “A non-fullerene acceptor with enhanced intermolecular π-core interaction for high-performance organic solar cells”. In: *Journal of the American Chemical Society* 142.36 (2020), pp. 15246–15251.

[146] Suhao Wang et al. “N-Type Molecular Thermoelectrics Based on Solut-ion-Doped Indenofluorene-Dimalononitrile: Simultaneous Enhancement of Doping Level and Molecular Order”. In: *Advanced Materials Technologies* 10.1 (2025), p. 2401131.

[147] Sang Eun Yoon et al. “Enhancing dopant diffusion for ultrahigh electrical conductivity and efficient thermoelectric conversion in conjugated polymers”. In: *Joule* 7.10 (2023), pp. 2291–2317.